Synchronisation of coupled chaotic systems

Giovanni Santoboni

Thesis submitted for the degree of

Doctor of Philosophy

Centre for Nonlinear Dynamics and its Applications

University College London

December 1999

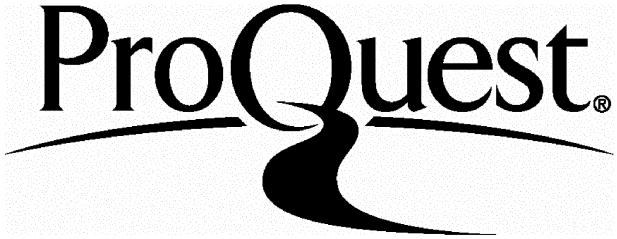

Acknowledgements

Many people in the years 1996/99 have contributed, at different times and in different ways to this work. First of all, I want to express my gratitude to my supervisor, Steve Bishop, for the help he constantly gave me during these years. I will never forget his openness for discussion, and his willingness to face many problems of very different nature during this time. Last, but certainly not least, his exquisite manners that narrowed the gap between a supervision and a friendship.

I owe a large debt of gratitude to Franco Meloni. Although officially not part of my Ph.D. programme, Franco, almost paternally, looked after me during this time, always having a free moment for me for any technical discussion, and for anything that generally I might have needed.

There are other people I feel honoured to have worked closely with, namely Rua Murray, currently at the University of Waikato, Guido Pegna and Rita Marrocu at the University of Cagliari, and Alberto Varone at the CRS4 in Cagliari.

The above are the people with whom I have worked with the closest contact, but I cannot forget here the helpful presence of all those who provided technical support, logistical help, and, of no less importance, offered a good company. They contributed invaluable help to finish this work. All these people deserve to be mentioned, but I deeply apologize in case somebody has been accidentally forgotten. Therefore, my deepest gratitude to Steve Baigent, Mario di Bernardo, Gian-Italo Bischi, Andrea Bosin, Kevin M. Campbell, Vittorio Cannas, Ricardo Carretero-Gonzáles, Thomas L. Carroll, Alexandra Chavez-Ross, Alessandro Chessa, Ben Cotton, Jack Daniel, Mike E. Davies, Celso Grebogi, Julie M. Haggerty, James P.M. Heald, Gert van der Heijden, Lutz Junge, Yorgos Karpodinis, Ying-Cheng Lai, Pietrino Manca, Valeria Meloni, Ana Guedes de Oliveira, Edward Ott, Louis M. Pecora, Alastair M. Rucklidge, Jaroslav Stark, Rob Sturman, Michael Thompson, and David J. Wagg.

Finally, the Regione Autonoma della Sardegna deserves a separate acknowledgment for financial support, especially Mr. Massimo Lallai, whose patience and willingness have always been precious to me.

Abstract

The study of chaotic dynamical systems has highlighted their extreme sensitivity to initial conditions effectively ruling out any long term prediction of response. It is therefore quite surprising that, despite this sensitivity, under certain conditions two chaotic systems coupled together in some way, may synchronise their behaviour producing identical responses.

This thesis mainly considers when synchronisation is accomplished with two identical dynamical systems coupled unidirectionally, *i.e.* with no feedback. In this way we aim to consider under what conditions a system may synchronise with an identical copy. As the coupling is altered the switch to convergence to the synchronised state can be viewed as a form of bifurcation. Initially, a trajectory will evolve within the higher dimensional coupled system phase space before eventually converging onto the invariant subset which is the synchronised state.

In this thesis some of the main features of this property are discussed, and evidence will be given of the peculiarities that makes this bifurcation unique with respect to all other typical changes that occur in a dynamical system. This importance is assured by the evidence that when the dynamics in the invariant subset is chaotic new previously unseen phenomena occur, for instance the presence of very complex basins of attraction and peculiar intermittent behaviour taking place in the neighbourhood of the transition point. Moreover, extensive numerical work has been carried out to explain the underlying processes responsible of the behaviour of coupled systems possessing an invariant subset. Particular attention has been devoted to two apparently uncorrelated problems; first, the numerical occurrence of synchronised behaviour when the chaotic motion in the invariant subset is nevertheless unstable and second, the scaling of the distribution of the transient time before convergence to the invariant subset, when this is stable.

Contents

List of Figures

List of Tables

Chapter 1

Introduction

1.1 Coupled oscillators and synchronisation

Major changes in composite materials and/or extended dynamical systems are generated by the dynamics of ensembles of interacting units. Chemical bonding, the problem of morphogenesis, as well as the oscillation of prices in the stock market and the survival of interacting biological species, can be seen as complex phenomena generated by the interaction of many degrees of freedom, represented as dynamics of coupled oscillator systems. So many and different are the disciplines subjected to such an analysis, that the understanding of the supposedly existing general laws of interaction between several systems are of major importance in scientific investigation. The dynamics of an isolated nonlinear oscillator can, in certain conditions, give rise to a very complicated motion, so it is a straightforward consequence to think of the dynamics of coupled oscillators as displaying a complexity well beyond analysis, due to the increased number of degrees of freedom.

On the contrary, it is a relatively recent idea that the behaviour of coupled oscillators systems can give rise to temporally and spatially organised structures, that we can observe in the organisation of the natural world. Take for example, the problem of *morphogenesis*, *i.e.* what is the origin of the cell differentiation, if the genetic material is the same in all cells? The problem was challenged firstly by A.M. Turing where in his pioneering work [1952] has shown that under cer-

tain conditions two interacting chemicals can generate a stable inhomogeneous pattern if one of the substances diffuses much faster than the other. As noted in [Koch & Meinhardt 94] and by Turing himself, this result goes against common sense, since diffusion is expected to smooth out concentrations rather then to enhance them.

The subject of this thesis is the so-called topic of *synchronisation of chaos*, meant as the ability of two or more coupled systems performing chaotic motion to converge onto a state which displays *exactly* the same values of their coordinates. Having in mind the remarks made above on the importance of the presence of organised behaviour in nature, and the considerations on how various and complex this organised motion can appear, it is easy to realize how the subject of this thesis is a phenomenon as important as it is rare, considering all possible ways we can make dynamical systems interact.

We can mathematically represent the situation, considering the equations

$$\begin{cases} \dfrac{d\boldsymbol{r}_1}{dt} = \boldsymbol{F}_1(\boldsymbol{r}_1) + K_1\boldsymbol{G}_1(\boldsymbol{r}_1, \boldsymbol{r}_2) \\ \dfrac{d\boldsymbol{r}_2}{dt} = \boldsymbol{F}_2(\boldsymbol{r}_2) + K_2\boldsymbol{G}_2(\boldsymbol{r}_2, \boldsymbol{r}_1) \end{cases} \tag{1.1}$$

where we have chosen a continuous time representation of a dynamical system, in the form of differential equations, but the same considerations can be stated for coupled discrete systems, such as iterative maps. The variables $\boldsymbol{r}_1$, $\boldsymbol{r}_2 \in \mathbb{R}^n$ are the coordinates of the two systems, in a $2n$-dimensional phase-space, $\boldsymbol{G}_1$ and $\boldsymbol{G}_2$ are the coupling functions, whose strengths of interaction are regulated by the constants K_1 and K_2, respectively. This is a very general way in which we can write down the equations of motion for two mutually interacting dynamical systems. We stated before that we will describe the situation in which two identical oscillators are coupled together, *i.e.* $\boldsymbol{F}_2 = \boldsymbol{F}_1 = \boldsymbol{F}$, setting the only requirement that if $\boldsymbol{r}_2 = \boldsymbol{r}_1$, then the coupling functions $\boldsymbol{G}_1(\boldsymbol{r}_1, \boldsymbol{r}_1) = \boldsymbol{G}_2(\boldsymbol{r}_1, \boldsymbol{r}_1) = \boldsymbol{0}$. With these constraints we see from Eqs. (1.1) that if at a certain time t_0, $\boldsymbol{r}_2(t_0) = \boldsymbol{r}_1(t_0)$, the equality of the variables will be mantained for all the future evolution. In this condition, the coupling terms will no longer influence the dynamics of the systems regardless of the values of K_1 and K_2, and the systems will continue their evolutions

synchronously, given by the solution of $d\boldsymbol{r}_1/dt = \boldsymbol{F}(\boldsymbol{r}_1)$, for both $\boldsymbol{r}_2$ and $\boldsymbol{r}_1$. This is the phenomenon of *synchronisation*, and unless otherwise explicitly stated, in all the thesis it will mean the exact equality of the coordinates of two or more coupled dynamical systems. The state $\boldsymbol{r}_2 = \boldsymbol{r}_1$ defines an n-dimensional hyperplane (more generally, an n-dimensional manifold) in the $\mathbb{R}^{2n}$ phase space, and we will denote this *invariant subset* as $\mathcal{S}$, alternatively called the *synchronisation manifold.*

It is not difficult to couple two or more dynamical systems in a way to ensure the existence of a synchronisation manifold, but this does not mean that trajectories will necessary converge onto it if their initial starting points are not already within $\mathcal{S}$, for this we must ask if the synchronisation manifold is stable. A more detailed discussion about the stability of the motion in $\mathcal{S}$ will be given later, but the problem can simply be introduced by looking at how trajectories close to $\mathcal{S}$ are attracted towards, or repelled from, $\mathcal{S}$. The usual technique will be to consider the dynamical evolution for the difference $\Delta\boldsymbol{r} = \boldsymbol{r}_2 - \boldsymbol{r}_1$

$$\frac{d\Delta\boldsymbol{r}}{dt} = \boldsymbol{H}(\Delta\boldsymbol{r}, \boldsymbol{r}_1), \tag{1.2}$$

where $\boldsymbol{H}(\Delta\boldsymbol{r}, \boldsymbol{r}_1) = \boldsymbol{F}(\boldsymbol{r}_1+\Delta\boldsymbol{r}) - \boldsymbol{F}(\boldsymbol{r}_1) - K_1\boldsymbol{G}_1(\boldsymbol{r}_1, \boldsymbol{r}_1+\Delta\boldsymbol{r}) + K_2\boldsymbol{G}_2(\boldsymbol{r}_1+\Delta\boldsymbol{r}, \boldsymbol{r}_1)$, and to investigate the evolution of perturbations close to $\mathcal{S}$, using the linearized equation

$$\frac{d\Delta\boldsymbol{r}}{dt} = DH(\boldsymbol{r}_1)\Delta\boldsymbol{r} + \mathcal{O}(\|\Delta\boldsymbol{r}\|^2), \tag{1.3}$$

where the matrix $DH(\boldsymbol{r}_1)$ has entries

$$[DH(\boldsymbol{r}_1)]_{ij} = \left.\frac{\partial H_i(\Delta\boldsymbol{r}, \boldsymbol{r}_1)}{\partial \Delta r_j}\right|_{\Delta\boldsymbol{r}=\boldsymbol{0}}. \tag{1.4}$$

The stability of the motion in $\mathcal{S}$ can be investigated by considering the eigenvalues of the matrix $DH(\boldsymbol{r}_1)$ that might be varying in time explicitly, or implicitly through one of the coordinates, as Eqs. (1.3) and (1.4) suggest. The vector $\Delta\boldsymbol{r}$ is perpendicular to the hyperplane defined by $\boldsymbol{r}_1 - \boldsymbol{r}_2 = \boldsymbol{0}$, so the stability of the motion on $\mathcal{S}$ is termed *transverse stability*, and the eigenvalues of the matrix $DH(\boldsymbol{r}_1)$ called the *transverse Lyapunov Exponents*, or given by the abbreviation TLE. Other terms and abbreviations are present in the scientific literature, such as Sub-Lyapunov Exponents (SLE), when the coupling between the two systems is

as in [Pecora & Carroll 90] (see Section 1.2.5) or Conditional Lyapunov Exponents (CLE), to underline the dependence of the Jacobian matrix $DH(\boldsymbol{r}_1)$ on the variables of one of the two systems. We note that, so far, we have not said anything yet about the dynamical system represented by $\boldsymbol{F}$, as well as for the coupling functions $\boldsymbol{G}_1, \boldsymbol{G}_2$. All the discussion above holds regardless of the properties of the given vectorial functions. As we said before, we will specifically discuss cases for which the chosen $\boldsymbol{F}$ will give rise to chaotic motion, but also drawing useful comments from the study of much simpler periodic evolution. Regarding the coupling terms, we have an infinite choice for the functions $\boldsymbol{G}_1$ and $\boldsymbol{G}_2$, as well as the parameters K_1 and K_2, to satisfy the requirement to have an invariant subset as described above. The coupling functions can be linear or nonlinear, or perhaps even (continuous or discontinuous) functions of time, modelling a different physical situation (as in the case of *adaptive control*, for example [Arecchi & Boccaletti 97]), or the more extreme one of *impulsive control* (as in [Yang & Chua 97]). A type of coupling we will frequently make use of obeys the requirement that

$$\boldsymbol{G}_i(\boldsymbol{r}_1, \boldsymbol{r}_2) = \boldsymbol{G}_i(\boldsymbol{r}_1 - \boldsymbol{r}_2),\ i = 1, 2$$

sometimes called *diffusive coupling*, for example, in [Bagnoli *et al.* 99] because of its resemblance to a discretized form, in time and space, of a reaction-diffusion system. In [Heagy *et al.* 94b], the coupling has a special form of *shift-invariant symmetry*, namely a function satisfying the property

$$\boldsymbol{G}_i(\boldsymbol{r}_j, \boldsymbol{r}_{j+1}, \cdots, \boldsymbol{r}_{j+N-1}) = \boldsymbol{G}_{i+1}(\boldsymbol{r}_{j-1}, \boldsymbol{r}_j, \cdots, \boldsymbol{r}_{j+N-2})$$

for $i, j = 0, 1, \cdots, N-1$, where N is the number of coupled units, $\boldsymbol{G}_i$ are the coupling functions, and all indices are understood to be taken $mod(N)$. In addition, if $K_1 = 0$ and $K_2 \neq 0$ (or vice-versa), the two systems in Eqs. (1.1) are called *unidirectionally coupled*, otherwise for K_1 and K_2 different from zero, we refer to this situation as *mutually coupled.* In addition, we will call *scalar coupling* the case in which $\boldsymbol{G}$ is a $n \times n$ diagonal matrix, with $G_{11} = G_{22} = \cdots = G_{nn}$.

So far we have not assumed that the coupling function possesses any particular symmetry, while in reality this might be the case. According to the action-reaction principle it seems quite natural to think that a part of a dynamical system

providing a coupling between two systems leads them to exert an equal and opposite force among them. However, even in experiments, the exact state of the coupling function does not provide severe difficulties, but rather problems may lie in the definition of "identical" for the systems used, a definition easy to implement in numerical simulations, but only with the bound of the experimental uncertainty in real systems. The simple equality of before $\boldsymbol{F}_2 = \boldsymbol{F}_1 = \boldsymbol{F}$ cannot be fulfilled in practice but nevertheless synchronisation can experimentally be achieved in coupled systems. There are several examples in literature, utilizing lasers [Roy & Thornburg 94, van Wiggeren & Roy 98], but mainly electronic circuits [Chua *et al.* 92, Kocarev *et al.* 92], as we will show in the third chapter of this thesis. Synchronisation has sometimes been found to be robust even for a parameter mismatch well beyond the experimental uncertainty associated with the parameter values, as in [Johnson *et al.* 98]. Nevertheless, synchronisation as discussed here is a situation ideally reached when a connection is made between systems of the same kind, and with nearly equal parameter values. Before dealing with the peculiarities of synchronised systems we will first see which other different phenomena of organised behaviour can occur in coupled systems.

1.1.1 Phase-locking of two coupled oscillators

The first example we can mention ever reported in the literature, is the report of the observations made by the Dutch physicist Christiaan Huygens that in 1665, in writing a letter to his father, described how two clocks mounted on the same yielding panel could synchronised their phase, probably through imperceptible vibrations in their common support. Huygens observations, reported in [Huygens 1673], boosted the study of coupled oscillators systems.

While the problem of linear oscillators with linear coupling is entirely solvable, the presence of nonlinearity makes the dynamic evolution richer. In [Haken 83] there is a good account of the possible phenomena produced by the coupling of linear oscillators via a nonlinear coupling, such as the frequency shift of the natural frequency of two oscillators when a feedback in a multiplicative form is inserted

into each other. We are nevertheless interested in phenomena resembling a sort of organised behaviour arising in these kind of systems, such as the common phenomenon of *phase locking* arising between coupled nonlinear oscillators.

The importance of this phenomenon is reflected in its practical applications. There are many cases in which the synchronisation of the phase variable of oscillators is the physical mechanism at the heart of the functioning of a particular device. In radio engineering, it is necessary to generate highly stabilized microwave oscillations. Since the existing klystron and magnetron generators do not have enough phase stability, they are usually coupled to a highly stabilized standard generator, like quartz-controlled or quantum generators. Moreover, some television receivers contain horizontal and vertical oscillators that position the fluorescent dot on the screen. All these oscillators must be operating at exactly the same frequency and phase as a signal being transmitted, otherwise the picture will move sideways or vertically. There are many other applications of the phase locking or synchronisation, and in the nonlinear dynamics literature the study of *phase locked loops* (PLL) is achieving some popularity; that is a basic mechanism for the synchronisation of phase in an oscillator, commonly used in a synchronisation scheme [Lindsey 72].

Let us consider that we have an input signal, $s(t,\theta) = A(t)\sin(\omega_0 t + \theta)$, where $A(t)$ is the amplitude modulation. Let the recovered signal, after multiplication at a VCO (Voltage controlled oscillator), be $r(t,\theta') = K\cos(\omega_0 t + \theta')$, where in absence of noise the same frequency w_0 is transmitted. Our interest is on the behaviour of the quantity $\phi = \theta - \theta'$, called the *total loop phase error.* A synchronous control system (SCS) will then determine the evolution of the total loop phase error, that we simply denote here as

$$\frac{d\phi}{dt} = \gamma - \sin\phi \tag{1.5}$$

which means that synchronisation, viewed as a phase locking phenomenon, occurs when $\phi = 2n\pi + \arcsin\gamma$, with n integer.

The study of the phase locking boosted a lot of research efforts, and Kuramoto [1984] gave an analytical description of the entrainment of coupled oscillators sys-

tems. Consider, for example, two oscillators with different frequencies coupled symmetrically, described by

$$\begin{cases} \dfrac{d\boldsymbol{x}_1}{dt} = \boldsymbol{F}_1(\boldsymbol{x}_1) + \varepsilon \boldsymbol{V}(\boldsymbol{x}_1, \boldsymbol{x}_2) \\ \dfrac{d\boldsymbol{x}_2}{dt} = \boldsymbol{F}_2(\boldsymbol{x}_2) + \varepsilon \boldsymbol{V}(\boldsymbol{x}_2, \boldsymbol{x}_1). \end{cases} \tag{1.6}$$

If the uncoupled oscillators are slightly different in nature from each other (say, of order ε), we may consider $\boldsymbol{F}_1(\boldsymbol{x}_1) = \boldsymbol{F}(\boldsymbol{x}_1) + \varepsilon \boldsymbol{f}_1(\boldsymbol{x}_1)$, and a similar equation for $\boldsymbol{x}_2$ so that,

$$\frac{d\boldsymbol{x}_i}{dt} = \boldsymbol{F}(\boldsymbol{x}_i) + \varepsilon \boldsymbol{p}_i, \ \boldsymbol{p}_i = \boldsymbol{V}(\boldsymbol{x}_1, \boldsymbol{x}_2) + \boldsymbol{f}_i(\boldsymbol{x}_i), \ i = 1, 2. \tag{1.7}$$

The problem is not so different from considering the dynamics of a time-perturbed oscillator, when the perturbation is induced by the coupling with the second equation. To have a more physical description of the phenomenon we are going to describe, it is better to change representation, from one of amplitude to that of phase. For a more detailed exposition of the procedure, we foward the reader to [Kuramoto 84], describing here only the main result. The phase ϕ corresponding to an arbitrary $\boldsymbol{x}$ of the state space is defined when, according to the time development of $\boldsymbol{x}$, ϕ satisfies the equation $\dot{\phi} = \omega$. In terms of the spatial dependence, this means that $\nabla_{\boldsymbol{x}} \phi \cdot \boldsymbol{F}(\boldsymbol{x}) = \omega$. If the motion of both the uncoupled oscillators was a limit cycle, and the perturbation ε is sufficently weak, we can assume that $\nabla_{\boldsymbol{x}} \phi$ can be evaluated on the limit cycle itself (as a perturbation of first-order), because these points are indeed close. The phase representation of Eqs. (1.7) is then

$$\begin{cases} \dot{\phi}_1 = \omega + \varepsilon [\nabla_{\boldsymbol{x}_C} \phi \cdot \boldsymbol{V}(\phi_1, \phi_2) + g_1(\phi_1)] \\ \dot{\phi}_2 = \omega + \varepsilon [\nabla_{\boldsymbol{x}_C} \phi \cdot \boldsymbol{V}(\phi_2, \phi_1) + g_2(\phi_2)] \end{cases} \tag{1.8}$$

where $g_i(\phi_i) = \nabla_{\boldsymbol{x}_C} \cdot \boldsymbol{f}_i(\boldsymbol{x}_C(\phi_i))$, $(i = 1, 2)$, in order to see the contribution from the isolated and coupled phases. In Eqs. (1.8) we have labelled the points forming the limit cycle considered with $\boldsymbol{x}_C$, and abbreviated $\boldsymbol{V}(\boldsymbol{x}_C(\phi_1), \boldsymbol{x}_C(\phi_2))$ to $\boldsymbol{V}(\phi_1, \phi_2)$. Let us now define $\phi_i = \omega t + \psi_i$, and consider the time average of all quantities in (1.8) after a period T of $\boldsymbol{x}_C$. After a time average of (1.8) over a

period T with constant phases ψ, it is possible to express the evolution of the ϕ_i as

$$\begin{cases} \dot{\psi}_1 = \tilde{\omega}_1 + \Gamma(\psi_1 - \psi_2) \\ \dot{\psi}_2 = \tilde{\omega}_2 + \Gamma(\psi_2 - \psi_1) \end{cases} \tag{1.9}$$

where now $\tilde{\omega}_i$ is the average of g_i over a period, and a similar definition can be derived for the function Γ. Consider now the difference of the phases. If $\psi = \psi_1 - \psi_2$, and $\Delta\tilde{\omega} = \tilde{\omega}_1 - \tilde{\omega}_2$, we have that

$$\frac{d\psi}{dt} = \Delta\tilde{\omega} + B(\psi) \tag{1.10}$$

where $B(\psi) = \Gamma(\psi) - \Gamma(-\psi)$, *i.e.* B is an odd function of ψ, and also T-periodic. Hence, there are values $\psi_0 = \frac{nT}{2}$, with n integer, that are certainly zeros of B. If the oscillators are identical ($\Delta\tilde{\omega} = 0$) these points are the equilibrium points of (1.10), alternatively stable and unstable in increasing n. For the unstable points, we will see a phase difference of half a cycle $T/2$. For more complicated forms of Γ, and for a nonzero but small frequency difference $\Delta\tilde{\omega}$, these equilibrium points will still give rise to a kind of phase-locked behaviour, where the relative phase distance will vary very slowly. This explains the occurrence of phase-locking.

1.1.2 Phase dynamics with more degrees of freedom

What happens if we consider a much larger assembly of coupled oscillators? If synchronisation is meant to be a dynamical state in which different parts show cooperative (or collective) behavour, we might be interested to see if such a phenomenon could result from the dynamics of large assemblies of coupled oscillators, having seen the synchronicity of the two-oscillator systems treated above. To keep some examples in mind from the natural world, in some parts of Southeast Asia, thousands of male fireflies gather in trees and flash in unison (a very nice color picture of this event can be seen in [Strogatz & Stewart 93]). In addition to this, A.T. Winfree reported many similar examples of collective phenomena, such as the chorusing of crickets, the synchronous firing of cardiac pacemaker cells, and the metabolic synchrony in yeast cell suspension [Winfree 80].

Remembering the coupled equations (1.9) in the phase representation, we can easily generalize the problem to the case of N-oscillator system, as

$$\frac{d\psi_i}{dt} = \tilde{\omega}_i + \sum_{j=1}^{N} \Gamma(\psi_i - \psi_j),\ i = 1, 2, \cdots, N. \tag{1.11}$$

In the particular case $\Gamma(\psi_i - \psi_j) = -K_{ij}\sin(\psi_i - \psi_j)$, Eqs. (1.11) are widely known as the *Kuramoto model* [Kuramoto 75].

The mutual entrainment is responsible for the transition between a disordered and an ordered state. In [Sakaguchi & Kuramoto 86] the authors indeed proved that this transition is a phase transition in the real thermodynamic meaning of the term [Yeomans 92], important because the main qualitative features of phase transitions are proved to be universal, *i.e.* independent of the special dynamical system used to model the base dynamics. More specifically, in [Sakaguchi & Kuramoto 86] it has been defined an *order parameter* σ as

$$\sigma e^{i\theta} = \frac{1}{N}\sum_{j=1}^{N} e^{i\psi_j}$$

(where θ is proportional to the time t), that goes to zero after a certain value of K or, in gradually varying the variance of the initial Gaussian distribution of the frequencies $\tilde{\omega}_i$, as in [Sakaguchi & Kuramoto 86].

1.2 Historical and phenomenological overview

We now adopt again the already defined meaning of the word "synchronisation" as the identical motion of two coupled oscillators. In the next subsections we will detect the synchronised motion in simple low-dimensional and non-chaotic systems then turn our attention to review how the problem has been brought about and discussed during the last years, when the identical motion of two coupled oscillators is chaotic.

1.2.1 Two coupled linear oscillators

Probably the first problem of coupled oscillators in any first course of mechanics is given by two coupled linear pendula. We consider two identical linear oscilla-

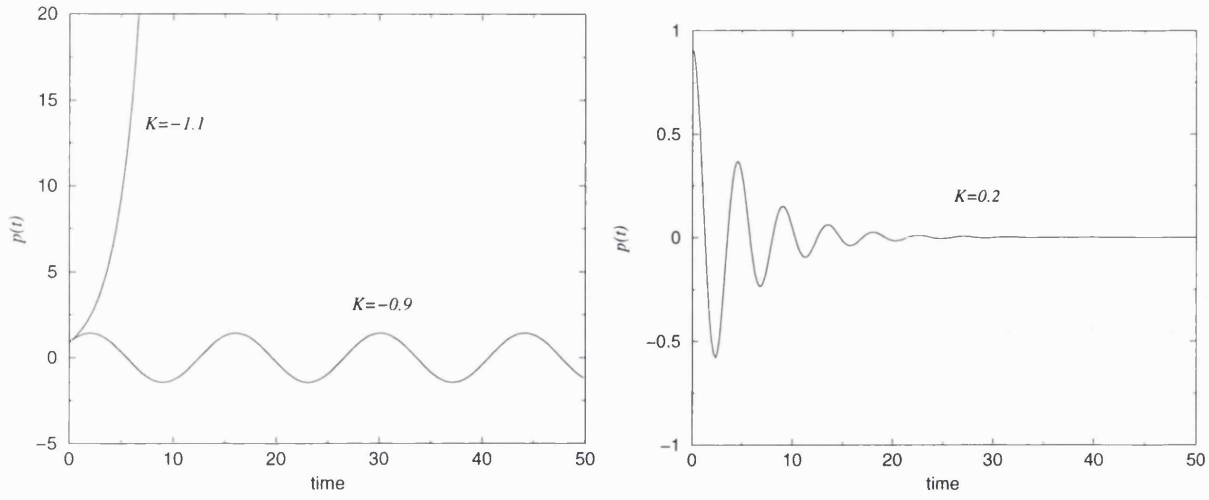

Figure 1.1: Left: Time series of $p(t)$ for a coupling matrix M as in (1.15), $M_{21} = K$, and two different values of K. Right: A second case, in which this time $M_{11} = K$ only.

tors (pendula, mass-spring, electronic circuits, ...) of mass m and parameter k_0, connected by a spring of elastic constant μ. If we call x and x' the respective displacement of the two masses, the equations of motion are:

$$\begin{cases} m\ddot{x} + k_0 x + \mu(x - x') = 0 \\ m\ddot{x}' + k_0 x' - \mu(x - x') = 0. \end{cases} \tag{1.12}$$

With the substitutions $\frac{k_0}{m} = \omega_0^2$, $\frac{\mu}{m} = K$, $y = \dot{x}$, and $y' = \dot{x}'$, we can express the Eqs. (1.12) as

$$\begin{cases} \dot{x} = y \\ \dot{y} = -\omega_0^2 x - K(x - x') \end{cases} \quad \begin{cases} \dot{x}' = y' \\ \dot{y}' = -\omega_0^2 x' + K(x - x'). \end{cases} \tag{1.13}$$

With the substitution $p = x - x'$ and $q = y - y'$, the dynamics transverse to the set $(x, y) = (x', y')$ evolve as

$$\frac{d}{dt}\begin{pmatrix} p \\ q \end{pmatrix} = \begin{pmatrix} 0 & 1 \\ -\omega_0^2 - 2K & 0 \end{pmatrix}\begin{pmatrix} p \\ q \end{pmatrix}, \tag{1.14}$$

There is a more compact way to visualize the structure of such a system, in the vector representation, Eqs. (1.13) are rewritten as

$$\begin{cases} \dfrac{d\boldsymbol{r}}{dt} = A\boldsymbol{r} - M(\boldsymbol{r} - \boldsymbol{r}') \\ \dfrac{d\boldsymbol{r}'}{dt} = A\boldsymbol{r}' + M(\boldsymbol{r} - \boldsymbol{r}') \end{cases} \tag{1.15}$$

where $\boldsymbol{r} = (x, y)$, $\boldsymbol{r}' = (x', y')$, $A \in \mathbb{R}^{2\times 2}$ is the matrix

$$A = \begin{pmatrix} 0 & 1 \\ -\omega_0^2 & 0 \end{pmatrix} \tag{1.16}$$

and $M \in \mathbb{R}^{2\times 2}$ is the coupling matrix, in this case with all zero elements except $M_{21} = K$. Our interest is focused on the behaviour of the difference between $\boldsymbol{r}$ and $\boldsymbol{r}'$ so, from (1.15), in the vector representation the difference equations are written as

$$\frac{d\Delta\boldsymbol{r}}{dt} = (A - 2M)\Delta\boldsymbol{r} \tag{1.17}$$

where $\Delta\boldsymbol{r} = \boldsymbol{r} - \boldsymbol{r}'$. The sign of the real part of the eigenvalues of the matrix $A - 2M$ provides us with the solution of the problem. If the maximum *transverse* eigenvalue (as explained before, the evolution of $\Delta\boldsymbol{r}$ is in the direction transverse to the manifold $\boldsymbol{r} = \boldsymbol{r}'$) has negative sign, then $\Delta\boldsymbol{r}(t) \to 0$ as the time increases, while if this eigenvalue has positive sign, the distance between $\boldsymbol{r}(t)$ and $\boldsymbol{r}'(t)$ must increase.

We can now discuss some cases of coupled linear oscillators of the form (1.12), and different forms of the coupling matrix M. The case shown in (1.12) is modelled by a coupling matrix M with all zeros but the element $M_{21} = K$. The matrix $A-2M$ is the matrix shown in Eqs. (1.14), and its eigenvalues are $\pm\sqrt{-(\omega_0^2 + 2K)}$, which are consequently complex conjugates for $K > -\omega_0^2/2$. We show, in Fig. 1.1, the time series of the linear system (1.12) for two different values of K. For $K < -\omega_0^2/2$ the eigenvalues of the matrix $A - 2M$ are complex conjugates, while for $K > -\omega_0^2/2$ they are real, identical but with opposite signs. With such a situation synchronised behaviour is not stable, as shown in Figure 1.1(left) for $\omega_0^2 = 2$. From the time series of the difference $p(t) = x(t) - x'(t)$ in Figure 1.1 it is possible to see that with complex conjugate eigenvalues ($K = -0.9$) $p(t)$ shows oscillating behaviour, while for real eigenvalues ($K = -1.1$) the trajectory diverges. Now consider all elements of the matrix M equal to zero this time except the $M_{11} = K$ (this case is quite untypical, it represents a coupling between the two pendula realized in such a particular way that the velocity behaves as $\dot{x} = y - K(x - x')$), and solve the eigenvalue problem. The eigenvalues obtained

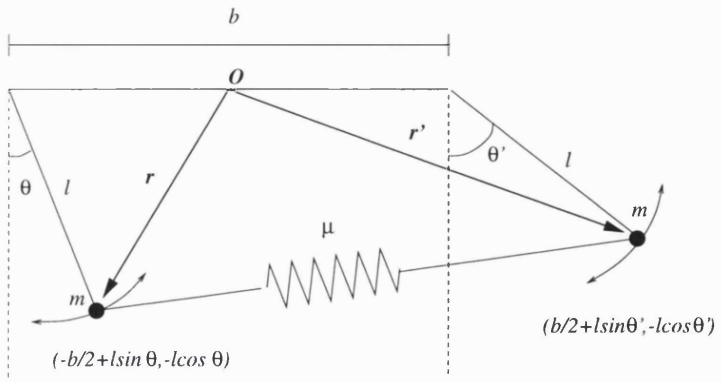

Figure 1.2: Schematic view of two coupled real pendula connected by a spring.

are $\lambda = -K \pm \sqrt{K^2 - \omega_0^2}$, so with negative real part for all $K > 0$. A portrait of the behaviour of the variable $p(t)$ in this second example is shown in the right picture of Figure 1.1. Because of the negative sign of λ, the trajectory quickly oscillates exponentially decaying to zero.

1.2.2 A nonlinear evolution

Two linearly coupled harmonic oscillators form a very simple model of synchronisation, which is analytically solvable. Unfortunately, we saw from the second example that to synchronise identically two oscillators starting from different initial starting conditions we need the presence of some sort of dissipation, so that the whole system can literally *converge* towards a solution. An example of synchronisation in a conservative map has been shown by [Zonghua and Shigang 97], where coupled *standard* maps are forced to synchronise via an impulsive coupling method, that still introduces dissipation in the response system. To introduce dissipation in a system of coupled oscillators, rather than to introduce very liberal sort of couplings, we can deal with nonlinear forms of the response function, that provide stable oscillatory solutions by the interaction of suitable damping and forcing terms. So we describe here a system of two coupled identical pendula, connected by a linear response mechanism (a spring obeying Hooke's law), to see if synchronisation between the two systems is possible. The schematic diagram of the mechanism is given in Figure 1.2. The angular displacement of the two pendula

are given by θ and θ', respectively. The origin of the axis is centered at **O**, and $\boldsymbol{r}, \boldsymbol{r}$' are the vectors defining the positions of the tips of the pendula, whose masses m and lengths l are the same. The pivots of the pendula are kept at a distance b, and their tips are connected by a spring obeying Hooke's law, with string constant μ and natural length is exactly b apart. We make the simplifying assumption that the spring has a neglibile mass compared to m. Under these conditions, whenever $\theta = \theta'$ (modulo 2π) the coupling force is null and synchronised motion is a possible mode of oscillation of the coupled system.

We derive now the equations of motion from the Lagrangian function, $L = T - V$, where the kinetic and potential terms are given by

$$\begin{aligned} T &= \tfrac{1}{2} m l^2 (\dot{\theta}^2 + \dot{\theta}'^2) \\ V &= mgl(\cos\theta + \cos\theta') - \tfrac{1}{2}\mu(\|\boldsymbol{r} - \boldsymbol{r}'\| - b)^2. \end{aligned} \tag{1.18}$$

We can derive the Lagrangian equations of motion, and using the substitutions $\omega^2 = \frac{g}{l}$, and $K = \frac{\mu}{ml^2}$, arrive at

$$\begin{cases} \ddot{\theta} + \omega^2 \sin\theta + K(\|\boldsymbol{r} - \boldsymbol{r}'\| - b)\dfrac{\partial}{\partial\theta}\|\boldsymbol{r} - \boldsymbol{r}'\| = 0 \\ \ddot{\theta}' + \omega^2 \sin\theta' + K(\|\boldsymbol{r} - \boldsymbol{r}'\| - b)\dfrac{\partial}{\partial\theta'}\|\boldsymbol{r} - \boldsymbol{r}'\| = 0 \end{cases} \tag{1.19}$$

where, from Figure 1.2,

$$\|\boldsymbol{r} - \boldsymbol{r}'\|^2 = b^2 - 2bl(\sin\theta - \sin\theta') + 2l^2[1 - \cos(\theta - \theta')],$$

and consequently,

$$\begin{aligned} \frac{\partial}{\partial\theta}\|\boldsymbol{r} - \boldsymbol{r}'\| &= -[bl\cos\theta + l^2\sin(\theta' - \theta)]\|\boldsymbol{r} - \boldsymbol{r}'\|^{-1} \\ \frac{\partial}{\partial\theta'}\|\boldsymbol{r} - \boldsymbol{r}'\| &= [bl\cos\theta' + l^2\sin(\theta' - \theta)]\|\boldsymbol{r} - \boldsymbol{r}'\|^{-1}. \end{aligned}$$

This is the Hamiltonian formulation of the problem, and in these terms the two real pendula shown in Figure 1.2 form a conservative system. We introduce in the uncoupled system ($K = 0$) a dissipative term γ, representing a linear damping coefficient accounting for the energy dissipation due to air resistance, and a sinusoidal forcing term $A\cos\omega_0 t$, of frequency ω_0 and amplitude A. The rescaled equation of motion of a single real pendulum provided with damping and forcing terms is written as

$$\ddot{\theta} + \gamma\dot{\theta} + \omega^2\sin\theta = A\cos\omega_0 t. \tag{1.20}$$

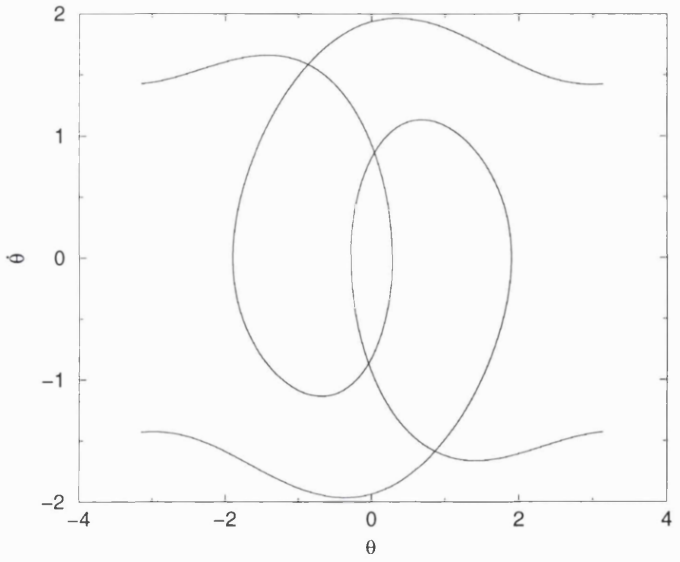

Figure 1.3: Two coexisting periodic solutions for the real pendulum, Eqs. (1.20). The top one has positive average velocity, and the lower one negative.

Much has been written on this system (see, for example, [Baker & Gollub 90]), being the extension of the harmonic pendulum, particularly when the angular displacement θ is small. If we consider all types of motion (not necessary small θ) then rotating solutions can exist. This system is also of great importance in solid-state physics, since the equations of motion also model the resistively-shunted Josephson junction [Gwinn & Westervelt 85]. Using the parameter values $\gamma = \frac{1}{2}$, $\omega_0 = \frac{2}{3}$ and $\omega = 1$, we can find a lot of qualitatively different solutions in varying the amplitude of the forcing A. Choosing $A = 1.35$ the Eqs. (1.20) display the two coexisting periodic solutions shown in Figure 1.3. these solutions differ in the sign of the average angular velocity $\langle\dot{\theta}\rangle$. We can now try to simulate the dynamics of two coupled real pendula (1.20), with the equations of motion

$$\begin{cases} \ddot{\theta} + \gamma\dot{\theta} + \omega^2 \sin\theta + KG_1(\theta, \theta') = A\cos\omega_0 t \\ \ddot{\theta}' + \gamma\dot{\theta}' + \omega^2 \sin\theta' + KG_2(\theta, \theta') = A\cos\omega_0 t \end{cases} \tag{1.21}$$

using the same parameter values as above for the nonlinear pendulum, then imposing that l is of unitary length and $b = 2l$, for the coupling terms. The coupling functions G_1 and G_2 are defined as $G_1 = \frac{1}{2}\frac{\partial}{\partial\theta}(\|\boldsymbol{r} - \boldsymbol{r}'\| - b)^2$, and the same for G_2 but with the differentiation in terms of θ', according to (1.18). We simulated

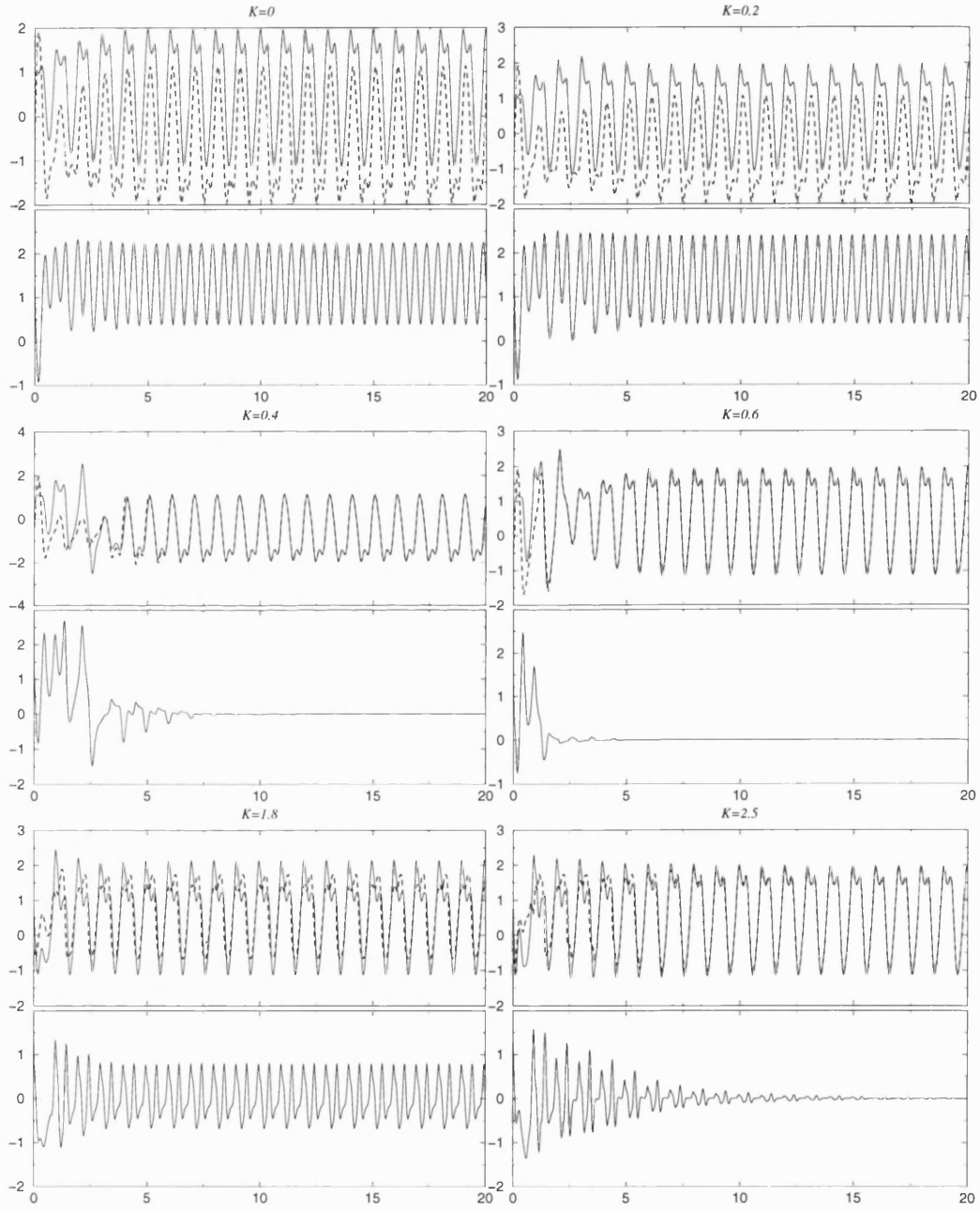

Figure 1.4: Synchronisation of two coupled real pendula connected by a spring in increasing the value of K. The abscissa represents the time expressed in the number of cycles of the forcing $\omega_0 t/2\pi$, while the upper and lower panels for each K value represent the time series of $\dot{\theta}$ (solid line) and $\dot{\theta}'$ (dashed line), and the difference between the two, respectively.

numerically the solution of Eqs. (1.21) with a Runge-Kutta algorithm with adaptive stepsize [Press *et al.* 92], and the results for different values of K are shown in Figure 1.4. All simulations are produced in such a way that the initial conditions of the two systems are specifically chosen to belong to different basins of attraction. More specifically, the solid line in the upper panel of each picture represents the time evolution of the $\dot{\theta}(t)$ variable of the first of the Eqs. (1.21), starting from the initial conditions $(\theta, \dot{\theta}) = (1.6, 1.0)$, giving a time evolution with a positive $\langle\dot{\theta}\rangle$, while the dashed line in the same panel represents the variable $\dot{\theta}'(t)$, with initial conditions $(\theta', \dot{\theta}') = (-2.1, -0.4)$, with $\langle\dot{\theta}'\rangle < 0$. The lower panel shows the evolution of the difference $\dot{\theta} - \dot{\theta}'$ between the two. The first picture in the top left is produced with $K = 0$. In this condition the two pendula are decoupled, and the orbits are rotating with opposite angular velocity, so to a certain extent we can say they are still "synchronised", but the pendula are not tracing out the same trajectory. If the coupling is increased to $K = 0.2$ there is still not a great difference from the decoupled case. In other words, the coupling term is not effective in reversing the velocity of one of the two oscillators. The condition which causes the first pendulum to change its direction of rotation is reached for $K = 0.4$ when the first pendulum, after approximately 3 cycles of the forcing reverses its velocity, so that both pendula are synchronised with negative angular velocity $\langle\dot{\theta}\rangle$. It seems intuitive to think that the synchronised state is stable for all values of $K > 0.4$. We show, for example, another case for $K = 0.6$, where this time the second pendulum reverses its direction of rotation. The result is still synchronised motion of the two oscillators. The intuition is not completely correct, since surprisingly, we can see that for $K = 1.8$ the two pendula are desynchronised again. However, for even larger values of K there is another case of synchronisation, as we can see in the last picture that for $K = 2.5$, and other zones of stability/instability can probably be found the the whole spectrum of values of K.

1.2.3 Chaotic synchronisation

The title of this Section might sound as a contradiction in terms. The sensitive dependence on initial conditions in all points of the phase space that characterizes the dynamic evolution of a chaotic system seems to imply that every attempt to search for any glimpse of organised behaviour is useless. Nevertheless, coupled chaotic systems can, under certain conditions, synchronise their oscillatory motions, sometimes also with a very strong degree of stability, robust in the presence of noise and even with mismatch of the parameters.

A natural extension of the great interest in the structure behind the complexity of chaotic systems during the '70s and the early '80s [Hao 90] is to consider the examination of the behaviour of these systems when they can influence each others after suitable coupling. We will give here first a brief account of the main works on the subject.

1.2.4 Pre-1990 work

It is not surprising that the first insights towards the study of the chaotic synchronisation came as a consequence of the studies on the phase dynamics of coupled oscillators by Kuramoto, and that the people who first worked in it were Kuramoto's collaborators, namely Hirokazu Fujisaka and Tomoji Yamada. In the years 1983-86 the two Japanese researchers published, in a series of papers in *Progress of Theoretical Physics*, results on their extensive studies on coupled dynamical systems undergoing a transition between non-uniform and uniform chaos, this latter called *synchronized state* [Fujisaka & Yamada 83,86], [Yamada & Fujisaka 83,84]. The authors considered coupled flows as well as discrete maps, where the spatial variation is modelled by adding a diffusion term with constant diffusion matrix $\widehat{D}$. In the first paper of their series they studied a continuous model

$$\frac{d\boldsymbol{x}^{(j)}(t)}{dt} = \boldsymbol{F}(\boldsymbol{x}^{(j)}, t) + \frac{\widehat{D}}{2}\sum_{l}(\boldsymbol{x}^{(l)} - \boldsymbol{x}^{(j)}),\ j = 1, 2, \cdots, N \qquad (1.22)$$

where, in their notation, the sum extends over a certain coupling configuration, that can be all-to-all, or nearest neighbours, with or without periodic boundary

conditions. Regarding discrete time systems, the authors took inspiration from the work of Kaneko on the coupled map lattices (see, for instance, [Kaneko 93]) and studied the same transition occurring in systems like

$$\boldsymbol{x}_{n+1}^{(i)} = \boldsymbol{g}(\boldsymbol{x}_n^{(i)}) + \widehat{D}\sum_{j=1}^{N}\{\boldsymbol{g}(\boldsymbol{x}_n^{(j)}) - \boldsymbol{g}(\boldsymbol{x}_n^{(i)})\}. \tag{1.23}$$

Fujisaka and Yamada firstly developed, with the study of systems (1.22,1.23) the expression for the stability of the synchronous state by means of the Lyapunov matrix approach, and in the case of scalar coupling (*i.e.* $\widehat{D}$ is a diagonal matrix with $\widehat{D}_{ii} = D$, $\forall i = 1, \cdots N$) they firstly hypothesized the possible use of the relation $D_c \propto 2\Lambda$ (where D_c is the point in the parameter D at which the synchronous state loses stability, and Λ the largest Lyapunov exponent in the synchronous state) to produce an accurate laboratory measurement of Λ, later developed by Schuster *et al.* [1986]. At about the same time, Pikovsky [1984] developed a study of diffusively coupled dynamical systems displaying a strange attractor, tracing almost the same research line of Fujisaka and Yamada. In addition, he firstly studied the statistical properties of the fluctuations close to the synchronised state, that we will later discuss in Chapter 4. Another remarkable work in this period is the one of Afraimovich *et al.* [1986], mainly devoted to coupled flows.

1.2.5 Pecora-Carroll's work

The earliest work by Pecora and Carroll [1990] is recognised as popularising the subject of synchronisation to a wider audience and boosting the now huge amount of research on the field. We have pictured the evolution of the "interest" that the scientific community had in the field of chaotic synchronisation since the beginning, that we attribute to the 1983 paper of Fujisaka and Yamada. A search made in BIDS Database (`http://www.bids.ac.uk`) gave the result shown in Figure 1.5. The works prior to 1990 cited before contain all the main characteristics that Pecora and Carroll will later cite (the proof of existence and stability of the invariant subset in maps as in flows), but nevertheless, the popularity that this research theme has now started after their 1990 publication in *Physical Review*

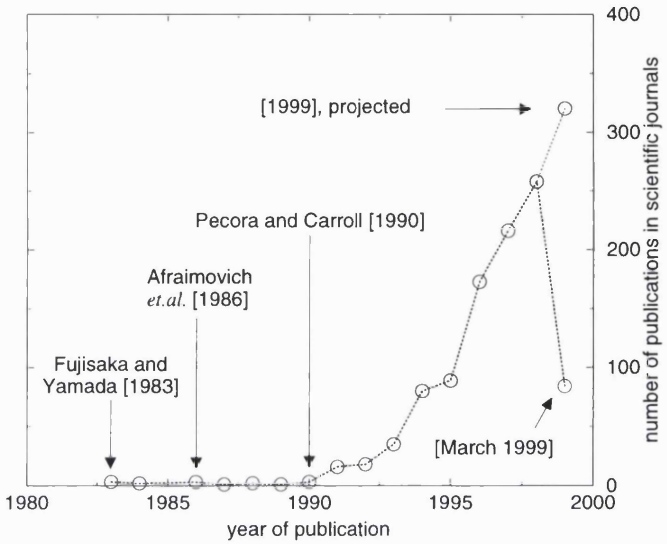

Figure 1.5: Number of publications in scientific journals on the subject of chaotic synchronisation from 1983 to March 1999. We evaluated the prevision for the end of the current year as [1999], projected $\simeq 4\times$[March 1999].

Letters. It is worth noting that the same year, and in the same journal, the first paper on the *control of chaos* [Ott *et al.* 90] by Ott, Grebogi and Yorke was published, showing that chaotic systems, apart from being synchronised, can also be *controlled*, in the specific sense that the chaotic evolution of a dynamical systems can be directed onto a desired periodic orbit embedded in the chaotic attractor. These two areas of research boosted the interest of the scientific community in the study of chaotic systems in view of promising possible applications to real systems. They also proved to be related to each others, if viewing the chaotic synchronisation as a form of *chaos-chaos control*, as in [Konnur 96].

The approach of Pecora and Carroll was to show the existence of chaotic synchronised oscillations with the link between the two systems provided by a common drive signal. Using their original notation, let

$$\dot{u} = f(u) \tag{1.24}$$

be an autonomous n-dimensional dynamical system, divided into two subsystems as $u = (v, w)$,

$$\dot{v} = g(v, w),\ \dot{w} = h(v, w), \tag{1.25}$$

where $v = (u_1, \cdots, u_m)$, $g = (f_1(u), \cdots, f_m(u))$, $w = (u_{m+1}, \cdots, u_n)$, and $h = (f_{m+1}(u), \cdots, f_n(u))$. Now a new subsystem w' must be created identical to the w system, such that

$$\dot{v} = g(v, w), \ \dot{w} = h(v, w), \ \dot{w'} = h(v, w'), \tag{1.26}$$

so that the subsystems w and w' are two identical copies of the same dynamical subsystem driven by the same signal v. With this situation, synchronisation occurs if the difference $\Delta w = w' - w$ goes identically to zero. Pecora and Carroll showed that when this happens the Lyapunov exponents for the subsystems are negative. The authors also pointed out that *the above theorem is a necessary, but not sufficient, condition for synchronization. It says nothing about the set of "initial conditions" in w' which will synchronize with w. (sic).*

In a previous work [Santoboni 96] we reproduced the results of the numerical experiments by Pecora and Carroll in [1990,1991] regarding the synchronisation applied to the Lorenz [1963] and Rössler [1976] systems. Few words deserve to be spent for the Lorenz system; this system is regarded historically to be one of the first ones in which the aperiodicity of a nonlinear system was demonstrated. The equations of motion of the Lorenz model are

$$\begin{cases} \dot{x} = \sigma(y - x) \\ \dot{y} = -xz + rx - y \\ \dot{z} = xy - bz \end{cases} \tag{1.27}$$

where σ, b, and r are real parameters. A three-dimensional portrait of the attractor is shown in Figure 1.6 for the parameter values $\sigma = 10$, $b = \frac{8}{3}$, and $r = 28$. In 1963 E.N. Lorenz derived Eqs. (1.27) as a model to study atmospheric convection, but few years later it was used also as a model describing the behaviour of a $^{15}NH_3$ laser [Haken 75]. According to the model, the parameters σ and b are related to the decay rates of the field κ, to the polarization $\gamma_\perp$, and of the population inversion $\gamma_\parallel$ by $\sigma = \kappa/\gamma_\perp$ and $b = \gamma_\parallel/\gamma_\perp$ and r is related to the pump parameter, while the variables x, y, and z describe the laser field, the polarization and the population inversion, respectively. In what follows, the notation $x(y, z)$ means x as

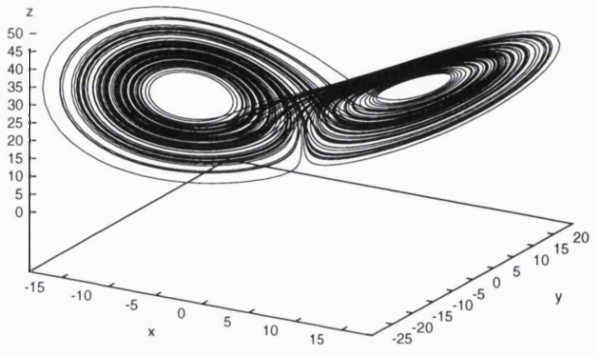

Figure 1.6: Three-dimensional view of the attractor of the Lorenz equations, Eqs. (1.27), for the parameter values $\sigma = 10$, $b = \frac{8}{3}$, and $r = 28$.

the drive signal and (y, z) as the response. The results are shown in Tab. 1.1. In all cases where both exponents for the subsystems are negative the corresponding numerical result showed synchronised behaviour, and desynchronised behaviour when at least one positive exponents. We show two of these cases in Figures 1.7. The first one is the Lorenz $x(y, z)$, represented by

$$\begin{cases} \dot{x} = \sigma(y - x) \\ \dot{y} = -xz + rx - y \\ \dot{z} = xy - bz \end{cases} \quad \begin{cases} \dot{y}' = -xz' + rx - y' \\ \dot{z}' = xy' - bz' \end{cases} \tag{1.28}$$

with the parameters value $\sigma = 16$, $b = 4$ and $r = 45.92$. The initial conditions used are $(x_0, y_0, z_0) = (11, -2, 5)$, and $(y'_0, z'_0) = (15, -7)$. Figure 1.7 shows the trajectories $y(t)$ and $y'(t)$ that synchronise very quickly. The other example is the Rössler $z(x, y)$:

$$\begin{cases} \dot{x} = -(y + z) \\ \dot{y} = x + ay \\ \dot{z} = b + z(x - c) \end{cases} \quad \begin{cases} \dot{x}' = -(y' + z) \\ \dot{y}' = x' + ay' \end{cases} \tag{1.29}$$

with the parameters $a = b = 0.2$ and $c = 9.0$. The initial conditions used are $(x_0, y_0, z_0) = (0, 5, -2)$, and $(x'_0, y'_0) = (-3, 1)$. In this case the Figure 1.7 shows

	P&C[1990,91]		[Santoboni 96]	
System	λ_1	λ_2	λ_1	λ_2
Lorenz $x(y,z)$	-2.5	-2.5	-2.422 ± 0.001	-2.570 ± 0.001
Lorenz $y(x,z)$	-3.95	-16.0	-4 (exact)	-16 (exact)
Lorenz $z(x,y)$	$7.89 \cdot 10^{-3}$	-17.0	0.0 ± 10^{-6}	-17.0 ± 10^{-6}
Rössler $x(y,z)$	0.2	-8.89	0.198 ± 0.001	-8.830 ± 0.002
Rössler $y(x,z)$	-0.056	-8.81	-0.039 ± 0.002	-8.798 ± 0.002
Rössler $z(x,y)$	0.1	0.1	0.099 ± 0.001	0.099 ± 0.001

Table 1.1: Lyapunov exponents for the responding system in 6 cases of synchronisation of the Lorenz and Rössler systems in the Pecora and Carroll's scheme. Data are available from [Pecora & Carroll 90,91] (left), and [Santoboni 96] (right). Pecora and Carroll do not report the uncertainties of their results in the cited papers.

two series that desynchronise very quickly. The first one $x(t)$ display chaotic behaviour, while the $x'(t)$ diverge after few time units.

1.2.6 Unidirectionally coupled chaotic systems

In all examples considered so far we have realised that once synchronised motion is achieved between two coupled identical systems, the dynamics in $\mathcal{S}$ is as if the oscillators were uncoupled. All coupling schemes fulfilling, as in Eqs. (1.1), the requirement that if $\boldsymbol{r}_2 = \boldsymbol{r}_1$, then $\boldsymbol{G}_1(\boldsymbol{r}_1, \boldsymbol{r}_1) = \boldsymbol{G}_2(\boldsymbol{r}_1, \boldsymbol{r}_1) = \boldsymbol{0}$, will give the same dynamics in $\mathcal{S}$, but different forms of $\boldsymbol{G}(\boldsymbol{r}_1, \boldsymbol{r}_2)$ will result in different properties of the motion outside of $\mathcal{S}$, and may or may not converge onto $\mathcal{S}$, at different coupling strengths and with different convergence rates.

From this moment on we will restrict the coupling schemes to have a unidirectionally coupling *i.e.* when one system (drive) influences another one, but without feedback from the second one (response). Suppose we have a drive-response scheme of coupled systems,

$$\boxed{\text{DRIVE}} \longrightarrow \boxed{\text{RESPONSE}}$$

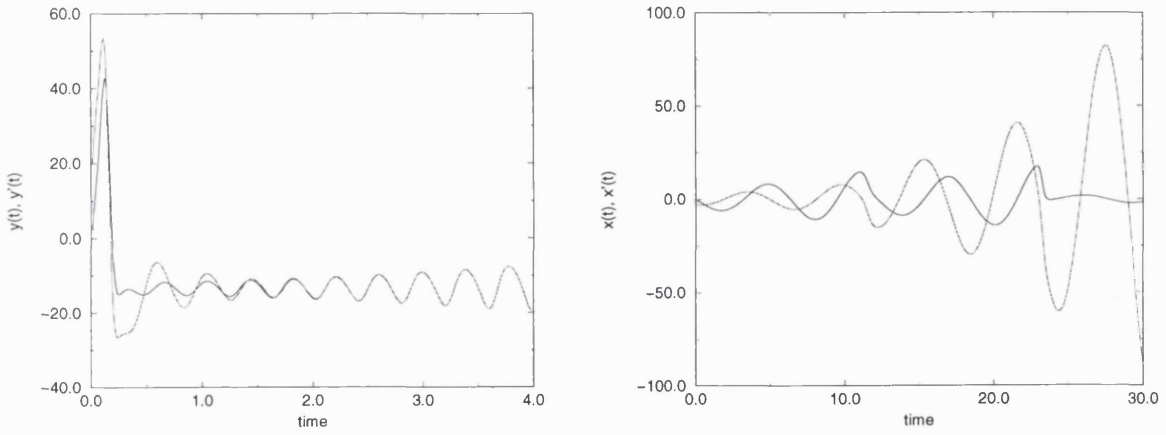

Figure 1.7: Left: Behaviour of $y(t)$ and $y'(t)$ for the Lorenz $x(y,z)$ system, Eqs. (1.28). The y variables of the two subsystems decay very quickly onto the synchronised state. Right: Variables $x(t)$ and $x'(t)$ for the Rössler $z(x,y)$ system (1.29). This time the behaviour is desynchronised, as suggested by the exponents reported in Tab. 1.1.

we can represent the problem in a more mathematical way, setting

$$\begin{cases} \dfrac{d\boldsymbol{r}_1}{dt} = \boldsymbol{F}(\boldsymbol{r}_1) \\ \dfrac{d\boldsymbol{r}_2}{dt} = \boldsymbol{F}(\boldsymbol{r}_2) + K\boldsymbol{G}(\boldsymbol{r}_2, \boldsymbol{r}_1), \end{cases} \tag{1.30}$$

where $\boldsymbol{F}$ is the functional form of the drive and response systems, and as the equations show, the output of $\boldsymbol{r}_1$ drives the one of $\boldsymbol{r}_2$, but no feedback exists. The case when $\boldsymbol{F}$ and $\boldsymbol{G}$ are linear functions of their arguments may be easy to discuss; when the coupling function $\boldsymbol{G}$ is linear in $\boldsymbol{r}_1$ and $\boldsymbol{r}_2$ the problem can be easily solved analytically.

The diffusive coupling of two identical systems as in Eqs.(1.1) automatically generates the simple invariant set $\boldsymbol{r}_1(t) = \boldsymbol{r}_2(t)$, cited before as the synchronisation manifold. From the Eqs.(1.1), the substitution $\Delta\boldsymbol{r} = \boldsymbol{r}_2 - \boldsymbol{r}_1$ leads to

$$\frac{d\Delta\boldsymbol{r}}{dt} = \boldsymbol{F}(\boldsymbol{r}_1 + \Delta\boldsymbol{r}) - \boldsymbol{F}(\boldsymbol{r}_1) - K\boldsymbol{G}(\Delta\boldsymbol{r}) \simeq DF(\boldsymbol{r}_1)\Delta\boldsymbol{r} - \boldsymbol{G}(\Delta\boldsymbol{r}) \tag{1.31}$$

in the case $\boldsymbol{G}(\boldsymbol{r}_2, \boldsymbol{r}_1) = \boldsymbol{G}(\Delta\boldsymbol{r})$, and where DF is the Jacobian matrix of $\boldsymbol{F}$. We simplify further the discussion using a linear coupling, as we shall do in several examples in the rest of the thesis. This corresponds to $\boldsymbol{G} = G \in \mathbb{R}^{n\times n}$, an $n \times n$ real matrix. In this notation, the corresponding characteristic exponents related to the

stability of the invariant subset are computed as the averages of the eigenvalues of the matrix $DF(\boldsymbol{r}_1) - KG$, when Eqs. (1.31) are integrated at the same time of the (1.30). These averages form the transverse Lyapunov exponents that can be computed according to different methods, as reported in [Benettin *et al.* 80, Shimada & Nagashima 79], or as described in [Eckmann & Ruelle 85]. As in the case of a single dynamical system, where a negative Lyapunov exponent indicates the convergence of the trajectory towards a fixed point, a negative transverse Lyapunov exponent indicates the stability of the synchronised state $\boldsymbol{r}_1(t) = \boldsymbol{r}_2(t)$. Unfortunately, this is a necessary but not sufficient condition for the synchronisation to occur, although not so many counterexamples are available [Gauthier & Bienfang 96]. A numerical example of unidirectionally coupled chaotic systems as well as its experimental counterpart will be shown in Chapter 3.

1.3 Varieties of synchronisation

Following [Abarbanel 95], while the diffusive coupling of identical systems leads to the existence of the invariant subset $\boldsymbol{r}_1(t) = \boldsymbol{r}_2(t)$, the coupling of dissimilar systems, *i.e.* in absence of a simply invariant subset, may lead to the presence of a relation between the two systems $\boldsymbol{r}'(t) = \boldsymbol{r}'(\boldsymbol{r}(t))$. This implies that

1. The motion is restricted to a lower dimensional manifold than the full phase space.

2. The evolution of $\boldsymbol{r}_1(t)$ is *predictable* in terms of $\boldsymbol{r}_2(t)$ and *vice versa* if the relation between $\boldsymbol{r}'$ and $\boldsymbol{r}$ is invertible. The identical synchronisation is so defined with this relation being the identity matrix.

We can give the following example, from [Rulkov *et al.* 95, Abarbanel 95]: Consider two identical Rössler [1976] oscillators coupled in a unidirectional way,

$$\begin{cases} \dot{x}_1 = -(y_1 + z_1) \\ \dot{y}_1 = x_1 + a y_1 \\ \dot{z}_1 = b + z_1(x_1 - c) \end{cases} \quad \begin{cases} \dot{x}_2 = -(y_2 + z_2) - K(x_2 - x) \\ \dot{y}_2 = x_2 + a y_2 \\ \dot{z}_2 = b + z_2(x_2 - c) \end{cases} \tag{1.32}$$

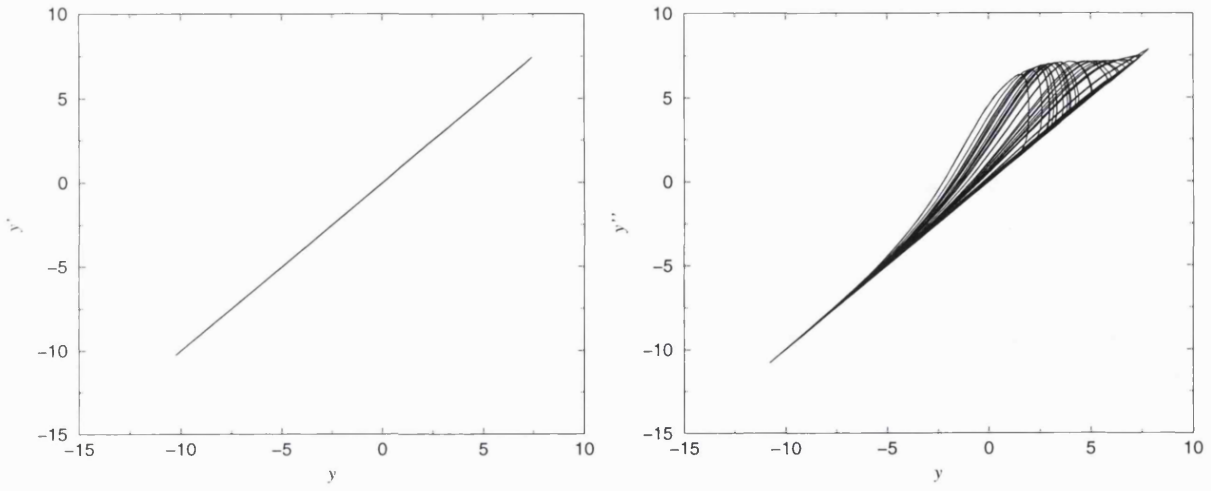

Figure 1.8: Left: y_1y_2 projection of the evolution of the system (1.32), showing identical synchronised motion. Right: A similar projection, but now for the variables y_1, y_3 from the system (1.33), showing a more complex relation between the variables.

with $a = b = 0.2$ and c=5.7. For this parameter set the driving system $\boldsymbol{r}_1 = (x_1, y_1, z_1)$ is known to display a chaotic attractor. Similarly, $\boldsymbol{r}_2 = (x_2, y_2, z_2)$ represents the trajectory of the response system. This is a case of coupling of identical systems so the invariant subset $\boldsymbol{r}_1(t) = \boldsymbol{r}_2(t)$ exists, and for $K = 0.15$ is unstable (with a transverse exponent $\lambda_\perp = 0.024$), while for $K = 0.20$ it becomes stable ($\lambda_\perp = -0.021$). If we plot together for $K = 0.20$, for example, $y_2(t)$ versus $y(t)$, this plot will display a straight line, as in Figure 1.8 (left), indicating that the synchronisation has occurred. Now we will construct a response system which exhibits a *generalized* kind of synchronisation. Making the simple nonlinear transformation $\boldsymbol{r}_2 \to \boldsymbol{r}_3$, with $\boldsymbol{r}_3 = (x_3, y_3, z_3)$ such that

$$x_3(t) = x_2(t),\ y_3(t) = y_2(t) + \alpha z_2(t) + \beta z_2(t)^2,\ z_3(t) = z_2(t)$$

with $\alpha = 0.4$ and $\beta = -0.008$, the response system now looks like

$$\begin{cases} \dot{x}_3 = -(y_3 + (1-\alpha)z_3 - \beta z_3^2) - K(x_3 - x) \\ \dot{y}_3 = x_3 + a(y_3 - \alpha z_3 - \beta z_3^2) \\ \dot{z}_3 = b + z_3(x_3 - c) \end{cases} \tag{1.33}$$

If we plot now $y_3(t)$ versus $y(t)$ for the synchronised state at $K = 0.20$, we no longer see a straight line but the more complex object shown in Fig. 1.8(right).

Nevertheless, the important thing to keep in mind is that since all we did was to perform a smooth change of coordinates, we believe that synchronisation, as a basic property of these coupled oscillators, cannot have been lost. The major goal of [Rulkov *et al.* 95] was to find a way to distinguish states of generalized synchronisation using just observations of the variables $y(t)$ and $y_3(t)$ alone, using the technique of the false nearest neighbours [Abarbanel 95].

Chapter 2

Signatures of chaotic synchronisation

2.1 Preliminaries

When a change of stability of a particular solution occurs in changing the value of a parameter of the system we say a bifurcation has taken place. When this solution is the invariant subset $\mathcal{S}$ of two coupled systems as discussed in the previous Chapter, and within $\mathcal{S}$ the motion is chaotic, then the bifurcation is termed *blowout bifurcation*. To our knowledge, this name was first used in [Ott & Sommerer 94], because of the "dramatic departure of the system state from the vicinity of the invariant manifold", so the orbit is literally "blown out".

The purpose of this chapter is to explain why the blowout bifurcation is so peculiar among many other changes of stability. We will show that when the invariant subset is weakly unstable a new form of intermittency may take place. Furthermore, when the invariant subset is stable, but another stable solution is also present outside the invariant subset, the set of all initial conditions converging to the invariant subset may have a very complicated shape. Finally, we will introduce something about the structure of the blowout bifurcation, and draw a scenario summarizing the events gradually taking place when a coupling parameter is varied across the blowout bifurcation point.

We start with some terminology and definitions for completeness, referring to the notation used in [Ashwin *et al.* 96]. Suppose that $\mathcal{M}$ is a smooth finite-dimensional manifold and $f : \mathcal{M} \to \mathcal{M}$ is a smooth map leaving the manifold $\mathcal{S}$ invariant, that is $f(\mathcal{S}) \subset \mathcal{S}$. Let $\mathcal{A}$ be a compact invariant set for f. The *basin of attraction* $\beta(\mathcal{A})$ is the set of points whose ω-limit set is contained in $\mathcal{A}$. $\mathcal{A}$ is an *asymptotically stable attractor* if:

1. if it is Lyapunov stable, *i.e.* if for every neighbourhood U of $\mathcal{A}$ there exist a neighbourhood V of $\mathcal{A}$ such that $f^n(V) \subset U$ for all n.

2. $\beta(\mathcal{A})$ contains a neighbourhood of $\mathcal{A}$.

An asymptotically stable attractor is also called a *topological* attractor. In many studies it is very common to encounter examples of basins of attraction that are open sets (as when the boundaries separating basins for different attractors are smooth or fractal, as we will show later), although this is not always the case. Consider a neighbourhood U of a point $x \in \beta(\mathcal{A})$. It is possible that a point chosen at random in U has positive probability of being in $\beta(\mathcal{A})$, and positive probability of not being in $\beta(\mathcal{A})$. It is then possible that an attractor will have a basin of attraction such that every point in the basin has points of another attractor basin arbitrarily nearby. According to [Alexander *et al.* 92], this motivates the following weaker definition of Milnor [1985]. $\mathcal{A}$ is a *Milnor attractor* if $\beta(\mathcal{A})$ has a non zero Lebesgue measure and there is no compact subset $\mathcal{A}'$ of $\mathcal{A}$ for which $\beta(\mathcal{A}') = \beta(\mathcal{A})$ up to a set of measure zero. This weaker definition is reflected in this well-known example: the Cantor set of the logistic map at the Feigenbaum point is Lyapunov stable and attracts a set of full Lebesgue measure, but nevertheless is not an asymptotically stable attractor [Buescu & Stewart 94]. Let $\mathcal{L}$ indicate the Lebesgue measure. A Milnor attractor $\mathcal{A}$ has a *riddled basin* [Alexander *et al.* 92] if, for all $x \in \beta(\mathcal{A})$ and all neighbourhoods B of $\mathcal{A}$ in $\mathcal{M}$ we have that

$$\mathcal{L}(B \cap \beta(\mathcal{A})) \neq 0 \text{ and } \mathcal{L}(B \cap \beta(\mathcal{A})^c) \neq 0$$

that is, both the basin of attraction $\beta(\mathcal{A})$ and its complement $\beta(\mathcal{A})^c$ intersect a neighbourhood B of $\mathcal{A}$ in a set of positive measure. This defintion has later been

generalized in [Ashwin *et al.* 94] saying that a Milnor attractor has a *locally riddled basin* if there is an $\varepsilon > 0$ such that for every point $x \in \beta(\mathcal{A})$ any arbitrary small ball centered on x contains a positive measure set of points whose orbits exceed a distance ε from $\mathcal{A}$. This generalizes the definition given before, including the possibility that $\beta(\mathcal{A})$ contains an open neighbourhood of $\mathcal{A}$. There are corresponding definitions for repelling sets too. A chaotic invariant set $\mathcal{A}$ is a *chaotic saddle* if there is a neighbourhood U of $\mathcal{A}$ such that $\beta(\mathcal{A}) \cap U \neq \mathcal{A}$ but $\mathcal{L}(\beta(\mathcal{A})) = 0$. Finally, [Ashwin *et al.* 94] coined a generalization for a chaotic saddle as for the riddled basin before. $\mathcal{A}$ is a *normally repelling chaotic saddle* if $\beta(\mathcal{A}) \neq \mathcal{A}$ and $\beta(\mathcal{A}) \subset \mathcal{S}$. In other words, there is an attractor in $\mathcal{S}$, but all points outside this subspace eventually leave a neighbourhood of $\mathcal{A}$.

2.2 Riddled basins

It is well known that the basin boundaries for two coexisting attractors can be very complex. Furthermore, chaotic transients in a nonlinear system converging towards an attractor imply the presence of fractal basin boundaries, while it is a more recent result that for chaotic systems with an invariant manifold of lower dimension than that of the full phase space, near the threshold of stability of the invariant subspace the presence of *riddled basins* may occur [Alexander *et al.* 92]. In particular, these systems may have an attractor whose basin of attraction is such that *every* point in the basin has pieces of another attractor's basin arbitrarily nearby. This means that if $\boldsymbol{r}_0$ is any point in the first attractor's basin, then the phase space ball of radius ε centered at $\boldsymbol{r}_0$ has a nonzero fraction of its volume lying in another attractor's basin, and this is so no matter how small ε is. Under these conditions, predictability is *qualitatively* an impossible task considering that, for such criticality, in any numerical simulation round-off errors and even differences in the machine used may cause a transient to settle onto any of the stable attractors [Hayli & Vidovic 94]. The presence of this phenomenon has been also reported in [Heagy *et al.* 94c, Lai & Grebogi 96a,b], and its formation commented and tentatively explained in [Lai *et al.* 96], and [Maistrenko *et al.* 98a,b].

If two attractors A and B coexist, let $\beta(A)$ be the basin of attraction for the attractor A and $\beta(B)$ the same for the attractor B; quite often the boundaries between $\beta(A)$ and $\beta(B)$, may possess intricate patterns, but a qualitative distinction can be made between:

(i) regular (with smooth boundaries). This is the case for the motion of a particle in a double-well potential [Thompson & Stewart 86], or for two mutually stable solutions of Chua's oscillator [Madan 93]. This system may show convergence towards two different periodic solutions, the final outcome depending from the initial conditions. In Fig. 2.1(top left) we show a basin of attraction for the stability of two different periodic solutions of Chua's oscillator,

$$\begin{cases} C_1 \frac{dv_1}{dt} = \frac{1}{R}(v_2 - v_1) - f(v_1) \\ C_2 \frac{dv_2}{dt} = \frac{1}{R}(v_1 - v_2) + i_L \\ L \frac{di_L}{dt} = -v_2 - R_0 i_L \end{cases}$$

These well-known equations model an electronic circuit with all linear elements except a negative piecewise resistor whose $v - i$ characteristic is represented by the function $f(v_1) = G_b v_1 + \frac{1}{2}(G_a - G_b)(|v_1 + B_p| - |v_1 - B_p|)$. This circuit will be more extensively discussed in the next Chapter. To generate this picture we used the parameter values $C_1 = 10.5nF$, $C_2 = 92.0nF$, $R = 2.03k\Omega$, $R_0 = 2.41\Omega$, $L = 20.0mH$, $G_a = -0.725mS$, $G_b = -0.370mS$, $B_p = 1.0V$, for which the Chua's oscillator exhibits two coexisting periodic attractors, with positive or negative x-coordinate. The black dots represent points belonging to the basin of the positive x-coordinate solution.

(ii) fractal (non-smooth boundaries). This case has been reported in many different systems, from nonlinear maps [Grebogi *et al.* 83a], to continuous systems as the damped driven pendulum [Baker & Gollub 90]. This system is modelled as in Eq. (1.20), with the parameters set to $\gamma = \frac{1}{2}$, $A = 1.48$, $\omega = 1$, and $\omega_0 = 2/3$, for which the system displays two mutually stable chaotic attractors, different in the value of the average angular velocity $\langle\dot{\theta}\rangle$. Black dots represent initial points in the basin of the attractor with positive $\langle\dot{\theta}\rangle$, while the negative average angular velocity attractor has its basin represented by the white zones.

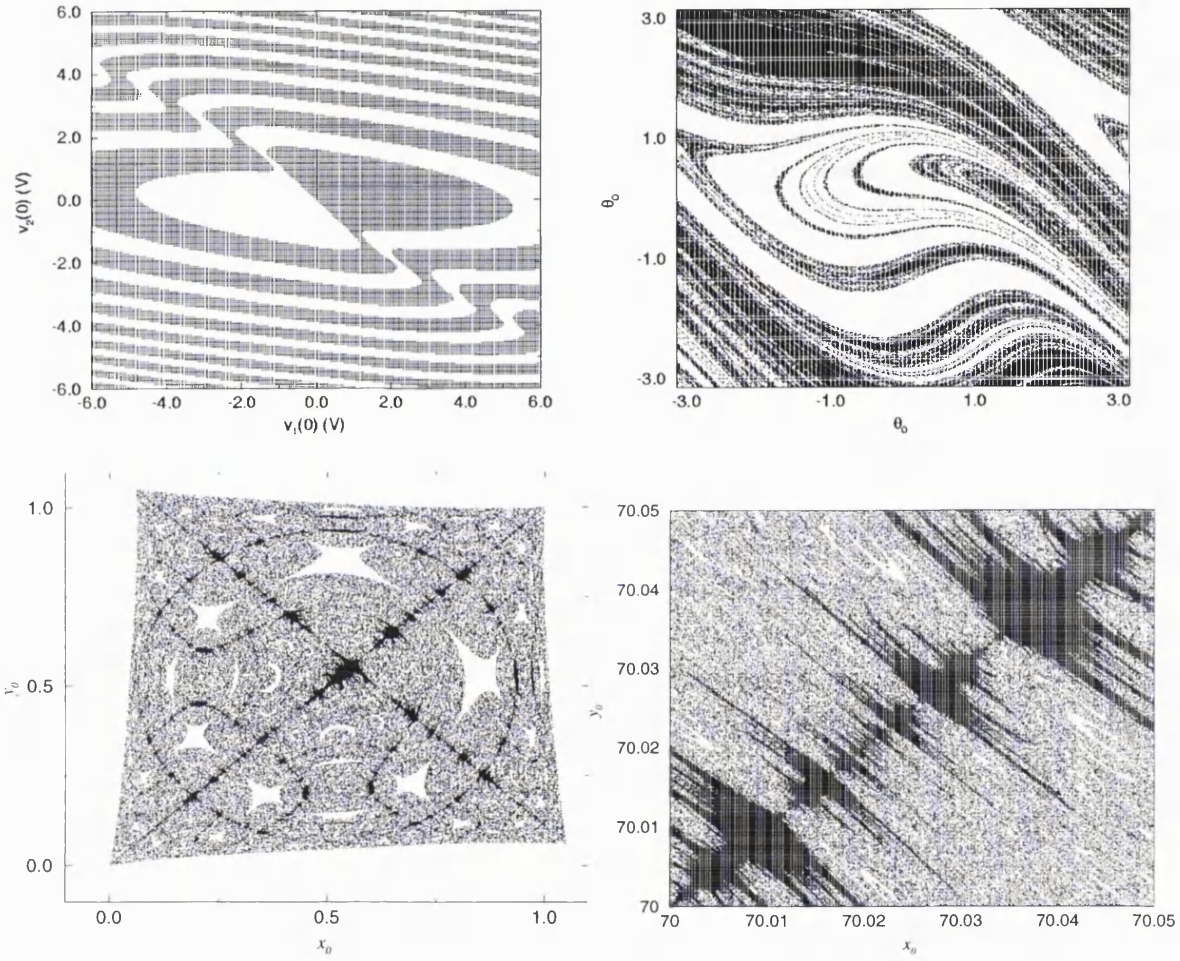

Figure 2.2: Top left: Basin of attraction for the stability of two different period-1 solutions of the Chua's oscillator. Black dots mark any initial point belonging to the basin of positive x-coordinate attractor. Top right: Portrait showing the fractal structure of the basin's boundaries for two different mutually stable attractors, different in the value of the average angular velocity $\langle\dot{\theta}\rangle$. Black dots represent initial points in the basin of the attractor with positive $\langle\dot{\theta}\rangle$, while the negative average angular velocity attractor has its basin represented by the white zones. Bottom left: Basin of attraction for the stability of the synchronised state of two linearly coupled logistic maps. Black dots represent points that converge to the invariant subset, while in the white zone they converge to a periodic solution outside the invariant subset, or diverge at infinity, anyway always desynchronised. Bottom right: enlargment of a portion of the basin of the Bottom left figure.

(iii) riddled (with no boundaries). An example of locally riddled basins is show in the bottom plots of Fig. 2.1. The system considered is a two dimensional system consisting of two linearly coupled logistic maps,

$$\begin{cases} x_{n+1} = ax_n(1 - x_n) - \varepsilon(x_n - y_n) \\ y_{n+1} = ay_n(1 - y_n) + \varepsilon(x_n - y_n) \end{cases} \tag{2.1}$$

where $\varepsilon = -0.2$, and $a = 3.574...$, so that a systems is at a band-merging (in increasing a) point in the bifurcation diagram where the attractor changes from 8-bands to 4-bands, where the motion can be proved to have an absolutely continuous invariant measure [Jakobson 81]. The example is taken from [Maistrenko *et al.* 98b].

2.2.1 Further examples

To show some of the qualitative features of a riddled basin, we consider a second example [Santoboni *et al.* 98] where the functional form $\mathbf{F}$ is represented by the Lorenz equations [Lorenz 63], whose equations of motion were given in (1.27). The equations of motion of the extended system are

$$\begin{cases} \dot{x} = \sigma(y - x) \\ \dot{y} = -xz + rx - y \\ \dot{z} = xy - bz - K(z - z') \end{cases} \quad \begin{cases} \dot{x}' = \sigma(y' - x') \\ \dot{y}' = -x'z' + rx' - y' \\ \dot{z}' = x'y' - bz' + K(z - z'). \end{cases} \tag{2.2}$$

The parameter values chosen are $\sigma = 16$, $b = 4$, $r = 45.92$, and $K = 5.6$. This case, however, is rather particular, because the Lorenz equations display a symmetry of inversion with respect of the z-axis, *i.e.* if (x, y, z) is a solution of Eqs. (1.27), so is $(-x, -y, z)$. The consequence of the particular kind of coupling in Eqs. (2.2) is the existence of two invariant subsets, defined by $(x, y, z) = (\pm x', \pm y', z')$. The threshold of stability of *both* the invariant subsets is located at $K \simeq 2$, so our choice here of $K = 5.6$ is beyond the threshold of stability, but which of the two subsets will result depends upon of the initial conditions. The riddled structure of the basin of attraction in this example is shown by a section of all the initial conditions converging towards one or other of the invariant subset.

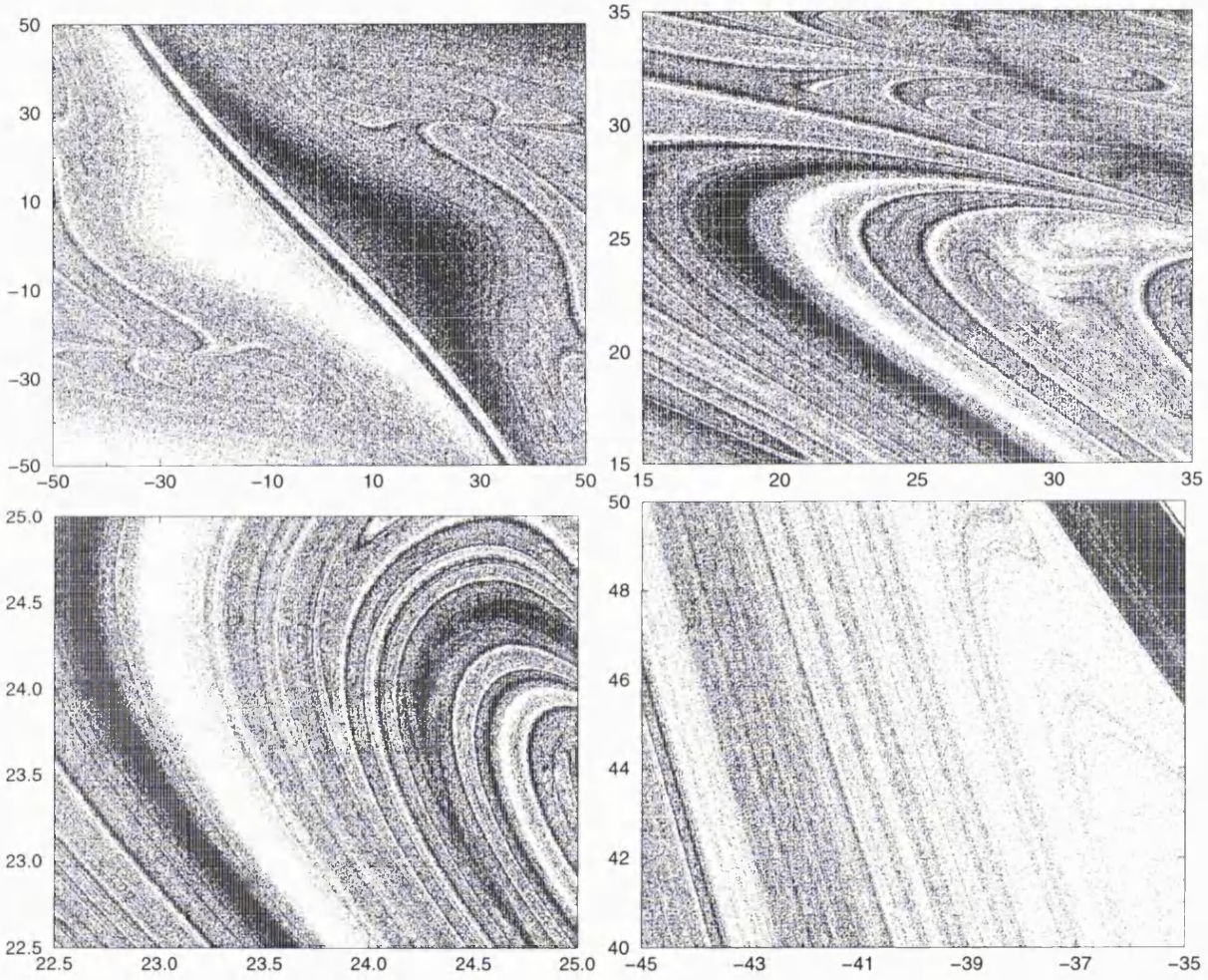

Figure 2.3: Four sections of the basin of attraction for the Eqs. (2.2) in the plane $(\Delta x_0, \Delta y_0)$, as defined in (2.3). The black dots represent initial conditions whose evolution converges towards $(x, y, z) = (x', y', z')$, while $(x, y, z) = (-x', -y', z')$ for the white zones. The last three pictures represent enlargments of the top left one, in order to show the intricate structure of the basin. An adaptive stepsize Runge-Kutta algorithm with initial step of $\Delta t = 0.01$ has been used to derive these plots.

We fix the initial conditions for the (x, y, z) system as $(x_0, y_0, z_0) = (1, -2, 5)$, and we use the simple rule

$$\begin{cases} x'_0 = x_0 + \Delta x_0 \\ y'_0 = y_0 + \Delta y_0 \\ z'_0 = z_0 \end{cases} \tag{2.3}$$

to define the initial conditions for the (x', y', z') system, where $(\Delta x_0, \Delta y_0)$, the deviations from the identical conditions case, vary in an appropriate interval. With the parameters set as above we find a portion of the basin of attraction in the plane $(\Delta x_0, \Delta y_0)$ for any of the two coordinates varied within $[-50, 50]$ as shown in the top-left picture of Fig. 2.2. In this figure three different enlargements of the basin are also shown. In all plots a black dot marks an initial condition whose evolution converges towards $(x, y, z) = (x', y', z')$, while all the other points evolve towards $(x, y, z) = (-x', -y', z')$. The first picture (top left) shows a very intricate structure where black and white zones tend to merge with each other with no definite boundaries. This first impression is confirmed by the first enlargement (top right) and other subsequent enlargements (bottom left) reveal more and more structure. The last picture (bottom right) is an enlargement but on a different point, from where it seems that the white zone is dominant, but with the presence of an arbitrary number of points belonging to the other basin in any point of it.

The numerical integration routine used to integrate the equations of motion have nevertheless some influence on the basin of attraction. As [Hayli & Vidovic 94] had already shown, if we use two different integration schemes we will see two different results, in the sense that several points will have different final destinations, when their evolution is differently computed. Nevertheless, the "pattern" shown by the basin still looks similar, indicating that there should be an underlying structure in the phase space. An insight towards this structure was shown by [Maistrenko *et al.* 98a,b] with the utilisation of the so-called *absorbing area*, defined by the locus of the zeros of the Jacobian matrix [Mira *et al.* 96].

2.3 On-off intermittency

Bifurcations induce structural changes in the dynamical behaviour of a system. Take the example of a periodic orbit undergoing a bifurcation, in varying a system parameter, and giving birth to a chaotic attractor (below). It is plausible that shortly after the bifurcation point, the chaotic wandering of the trajectory will resemble the previously stable periodic orbit for some interval of time, interrupted by finite duration "bursts" in which the orbit behaves differently. We consider the example of the stable period-3 solution of a logistic map, $x_{n+1} = f(x_n) = ax_n(1 - x_n)$ undergoing a tangent bifurcation for $a = 1 + \sqrt{8} = 3.828427...$, when before this point a chaotic solution takes its place. The details of this bifurcation are given in Figure 2.3. In the left picture, the bifurcation diagram of the logistic map is given in the interval $a \in [1, 4]$. An enlargment of this diagram, showing in better detail the period three window is shown in the middle picture. The period three window is created, in increasing a, from chaotic behaviour by a tangent bifurcation where a stable and unstable period-3 orbits meet at $a = 1 + \sqrt{8}$, and ends via a period doubling cascade returning to chaotic behaviour. The picture on the right hand side gives a pictorial representation of the mechanism of the tangent bifurcation leading to chaos. Before the tangent bifurcation, the time series x_n shows the presence of intermittent behaviour. A trajectory, starting from a typical initial condition, will spend a lot of time close to the period-3 orbit, during the chaotic wandering of the trajectory. These time intervals have been termed *laminar phases.* The length of the laminar phases depends crucially on the distance of the parameter a from the bifurcation point a_t. Let $\varepsilon = a_t - a$. We show in Figure 2.4 three time series of $f^3(x_n)$ for three different values of ε. Using the three-times iterated map, a period-3 orbit is thus represented by a fixed point. 1000 iterations for each value of ε are shown in Figure 2.4. The description of *intermittency* was first been given in [Pomeau & Manneville 80], using as an example a tangent bifurcation in the Lorenz model where a periodic solution loses stability giving way to chaotic behaviour with long laminar phases close to the bifurcation point. The length of a laminar phase can be quite different within the

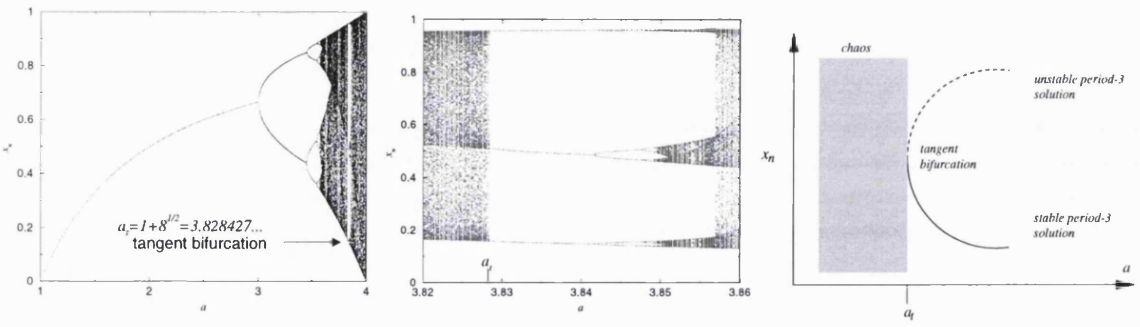

Figure 2.3: Mechanism of route to chaos through inverse tangent bifurcation in the logistic map. The point in parameter space a of the map is first shown in the left, and in the middle picture an enlarged view is given of the period-3 window. A schematic mechanism of the bifurcation is then given in the right picture, where is shown the collision between a stable and unstable period-3 orbit at $a = a_t = 1 + \sqrt{8}$ leading to chaos for $a < a_t$.

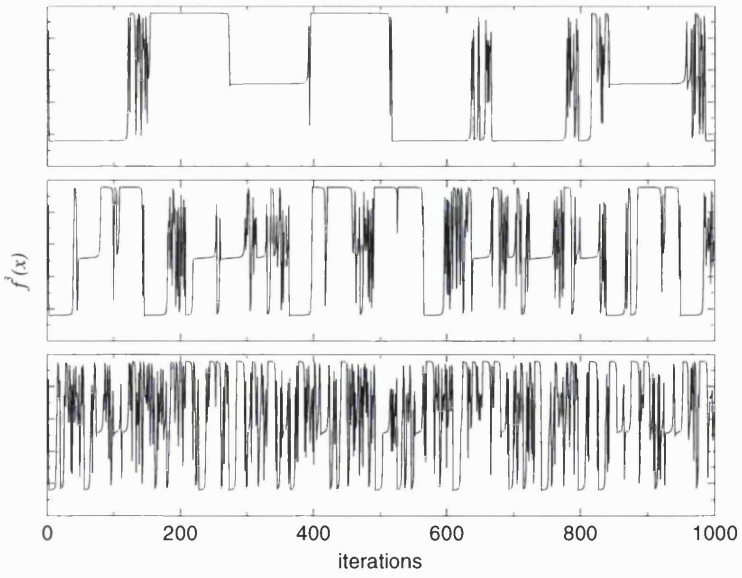

Figure 2.4: Three time series of the three-times applied $(f^3(x_n))$ logistic map for $a = a_t - \varepsilon$, with $\varepsilon = 10^{-5}$ (top), $\varepsilon = 10^{-4}$ (middle) and $\varepsilon = 10^{-3}$ (bottom), where in the same iterations number it is shown the different length of the laminar phases, represented by fixed points.

Type	Bifurcation	α	β
I	saddle-node (tangent)	1/2	1/2
II	subcritical Hopf	1	2
III	inverse period doubling	1	3/2

Table 2.1: Summary of the power law exponents of the three types of intermittency as classified by Pomeau and Manneville [1980].

same time series, and it will be likely to be longer when the bifurcation parameter is close to the bifurcation point, as Figure 2.4 shows. It is interesting to ask how the average laminar phase varies as the parameter a is changed, and also if/how the type of bifurcation creating the intermittent bevaviour influences the distribution of laminar phases. Let p be a parameter for a certain dynamical system, and p_c a bifurcation point. Pomeau and Manneville [1980] classified three different types of intermittent behaviours according to the bifurcation occurring and the respective scaling properties, such as the average laminar phase lenght $\bar{l}$, and the distribution of laminar phases $P(l)$, as shown in Tab. 2.1. Both these quantities scale as a power law function of $p - p_c$, and Tab. 2.1 gives the exponents α and β, appearing in $\bar{l} \sim (p - p_c)^{-\alpha}$, and $P(l) \sim (p - p_c)^{-\beta}$, respectively.

A bifurcation from periodic to chaotic behaviour is not the only mechanism for intermittency. Another case is the *crises induced intermittency*, when an interior (merging) crises takes place, *i.e.* when the size of a chaotic attractor suddenly changes [Grebogi *et al.* 83b].

A new kind of intermittent behaviour has been recently discovered by Fujisaka and Yamada [1985], and characterized by Platt and coworkers [Platt *et al.* 93, Heagy *et al.* 94a, Hammer *et al.* 94], taking place when a systems undergoes a blowout bifurcation, and named *on-off intermittency.* This intermittent behaviour derives its name from its characteristic two-state nature. The "off" state is nearly constant (the laminar phase), and can remain so for long periods of time, interrupted by the "on" state, a sudden bursting event that quickly returns to the off

state. Consider a simple dynamical system modelled by the iterative process

$$\begin{cases} x_{n+1} = f(x_n) \\ y_{n+1} = G(x_n, p)g(y_n), \end{cases} \tag{2.4}$$

where the function G models the external drive to the y dynamics, and p is a scalar parameter. With the restriction that $g(0) = 0$ the system (2.4) has the invariant subset defined by $y_n = 0$, that we regard as the asymptotic value of the off state. We illustrate the details of the intermittent process with a specific numerical example, taken from [Lai 96], where $f(x)$ represents the tent map, and

$$y_{n+1} = \frac{1}{2\pi} p x_n \sin(2\pi y_n). \tag{2.5}$$

The characteristic exponent associated with the stability of the state $y_n = 0$ is given by

$$\lambda_\perp = \int_0^1 \log \left| \frac{\partial y_{n+1}}{\partial y_n} \right|_{y_n=0} \rho(x)dx = \int_0^1 \log |px| dx = \log p - 1, \tag{2.6}$$

so the system (2.4) undergoes a blowout bifurcation at $p_c = e = 2.71828...$, where the $y_n = 0$ state is stable for $p < p_c$, and stable intermittent behaviour can occur for $p > p_c$. Figure 2.5 shows two cases of 1000 iterations for the system (2.4) for $p = 2.8$ showing on-off intermittency. In the top picture a random sequence x_n in [0,1] drives the y systems, while in the bottom picture the driving part is a deterministic system, namely the symmetric tent map[1] $x_{n+1} = 1 - |1 - 2x_n|$. For both pictures the time series of $|y|$ and $\log_{10}|y|$ are shown. The time series of y displays this kind of intermittency, with long stretches of time (laminar phases) during which the trajectory approaches the invariant subset (at distances sometimes below 10^{-8} in the top picture, and 10^{-10} in the bottom one), interrupted by sudden bursts where the trajectory reaches values of the same order of magnitude as the attractor in $\mathcal{S}$.

[1]The symmetric tent map must numerically be implemented with care. It is well known that the numerical iteration of this map converges to the zero fixed point, although a chaotic attractor can be proven to exist. To overcome this problem here (and onwards) we decide to shift the inversion point of the map of a small amount $\varepsilon = 10^{-10}$. The map loses its symmetry about 1/2, but the asymmetry is so slight that its shape is not significantly affected.

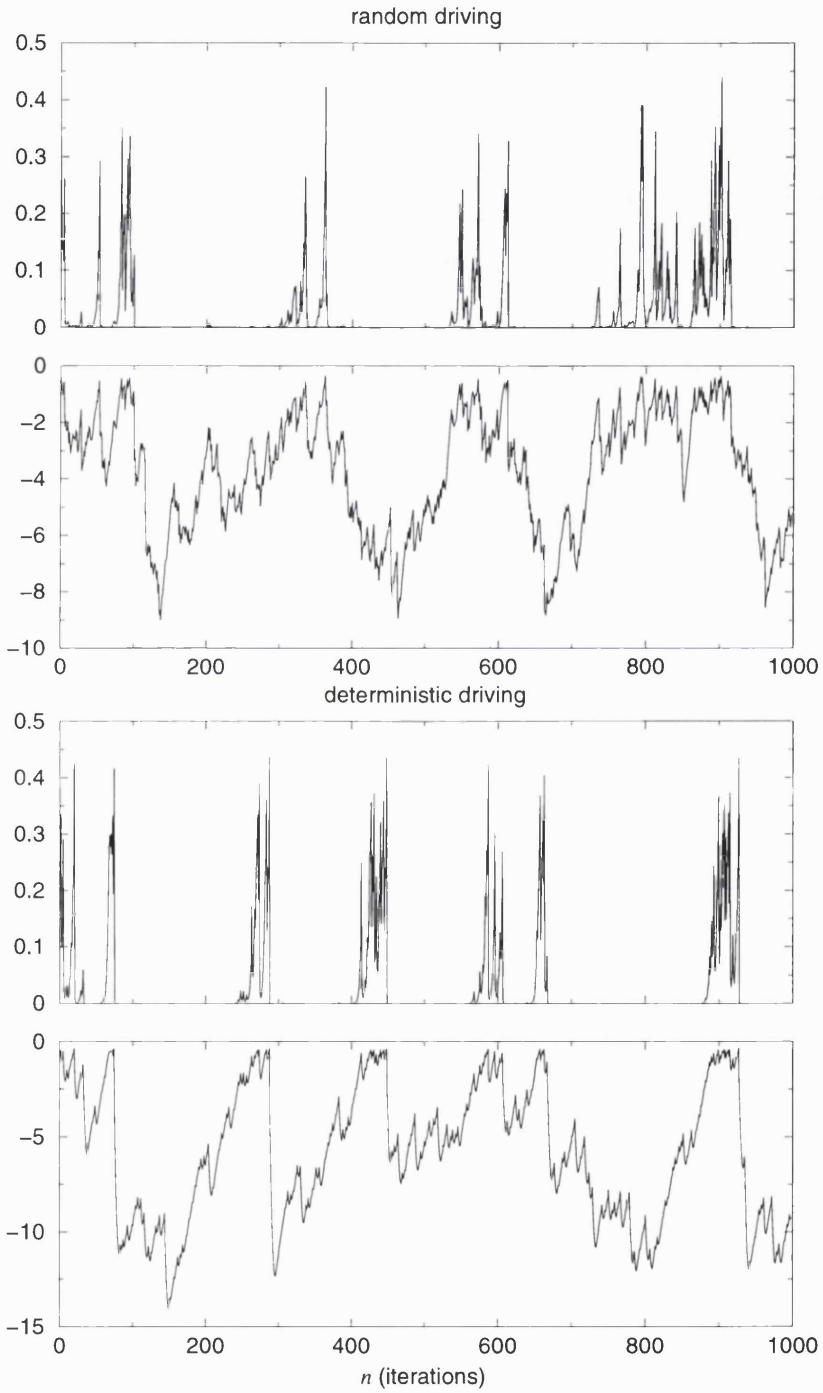

Figure 2.5: On-off intermittent time series from Eq. (2.4) with random driving (top picture) and deterministic driving (bottom picture). For both pictures $|y|$ and $\log_{10}|y|$ are given.

In systems with an invariant subset, another kind of intermittent behaviour has been reported when small changes in the dynamical system that destroys the invariant subspace, like a mismatch of parameters, or the presence of noise. This additional form of "noise-induced" intermittency has been termed *bubbling*, from [Ashwin *et al.* 94, Venkataramani *et al.* 96].

An on-off intermittent series has a statistical characterisation as does the Pomeau-Manneville types discussed previously, and in [Heagy *et al.* 94a] some results on the study of these statistical properties were reported for both deterministic and random driving. The laminar phases for $p \gtrsim p_c$ are stretches of time during which the trajectory of y stays very close to zero, so an investigation of the properties of that time series must start from the linearized equations corresponding to the (2.5). From (2.5) we have that for $y \simeq 0$, $y_{n+1} = p x_n y_n + \mathcal{O}(y_n^2)$, thus giving

$$y_n = P_n y_0 = p^n \left[\prod_{i=0}^{n-1} x_i \right] y_0 \tag{2.7}$$

keeping only the linear term in y. The long-term behaviour of the variable y is thus determined by the asymptotic behaviour of the random product P_n. We review now the main result contained in [Heagy *et al.* 94a], fowarding the reader to the paper for the details of the proof. For a portion of the trajectory of y to be in a laminar phase we have to define a small threshold τ below which the signal is considered to be "off". This said, a laminar phase of length n is defined as

$$\{y_1 \leq \tau, y_2 \leq \tau, \cdots, y_n \leq \tau, y_{n+1} > \tau\}$$

and we are interested in finding the probability that a laminar phase has length n if $y_0 \leq \tau$. This probability is expressed by the conditional probability

$$\Lambda_n = \text{Prob} \left[\bigcap_{j=1}^{n} \{ y_j \leq \tau \cap y_{n+1} > \tau | y_1 \leq \tau \} \right]. \tag{2.8}$$

Heagy *et al.* [1994a] found an expression for the asymptotic probability for large n and a parameter $p = e + \delta$,

$$\Lambda_n \sim \frac{e}{2\sqrt{2\pi}} e^{-\frac{n\delta^2}{2e^2}} n^{-3/2} \tag{2.9}$$

so that the distribution of laminar phases scales as a power-law of n with exponent -3/2 at the blowout, for $\delta = 0$. In the same paper the exponent of the power-law scaling has numerically been shown to be the same for a large class of discrete maps, and then proved to be universal for, at least, all dynamical systems posessing a natural density with zero mean and finite variance. To confirm this prediction, Hata and Miyazaki [1997] derived an *ad hoc* system consisting of a three-dimensional map with on-off intermittency. The 3D map they derived posesses the Markov condition so that enabled them to find analytical expressions for the probability density function $P(n)$ as well as the distribution of the laminar phases, that agrees with the (2.9), showing a distribution $\Lambda_n \sim n^{-3/2}$, at the blowout.

2.4 The blowout bifurcation

The typical scenario for the change of stability of an attractor $\mathcal{A}$ in an invariant subset $\mathcal{S}$ of the global phase space can be as follows [Ashwin *et al.* 94]. Assume that there is a parameter, say K, that tunes the strength of dissipation in the direction transverse to the invariant subspace, without changing the dynamics on it. Such a parameter is called *normal*, because it acts only to change the dissipation in the direction transverse to $\mathcal{S}$ (some studies have already been presented for the blowout bifurcation when a *non-normal* parameter is changed [Covas *et al.* 97]). Briefly following the original discussion of Ashwin, Buescu and Stewart [1994], there are three parameter values $K_0 < K_1 < K_2$ such that:

i. For $K < K_0$ $\mathcal{A}$ is a normally repelling chaotic saddle.

ii. For $K_0 < K < K_1$ $\mathcal{A}$ is a chaotic saddle.

iii. For $K_1 < K < K_2$ $\mathcal{A}$ is an attractor with a locally riddled basin.

iv. For $K > K_2$ $\mathcal{A}$ is an asymptotically stable attractor.

At K_0 the chaotic subset $\mathcal{A}$ becomes a chaotic saddle. At K_1 a blowout bifurcation takes place, and the transverse Lyapunov exponent $\lambda_\perp$ computed with the

natural measure on $\mathcal{A}$ becomes zero. In the region $K_1 < K < K_2$ $\mathcal{A}$ is not asymptotically stable, but it is still an attractor in the weaker sense, a Milnor attractor as defined at the beginning of the chapter. Finally, at K_2 $\mathcal{A}$ gains asymptotic stability, so all cycles embedded in $\mathcal{A}$ becomes transversely attracting.

Ott and Sommerer [1994] first noted and then Ashwin *et al.* [1998] later classified two possible different scenarios for the occurrence of the blowout bifurcation. These scenarios are the *hysteretic* and *non-hysteretic* types, whose difference in the phenomenology is due to the different route to the loss of stability. These scenarios are summarised in Figure 2.6. They can be briefly described as

1. Hysteretic (subcritical) scenario: riddled basins before the blowout give rise to a "hard" loss of stability, where after blowout almost all points eventually never return close to $\mathcal{S}$.

2. Non-hysteretic (supercritical) scenario: the loss of stability is a less dramatic one; after the blowout bifurcation on-off intermittent behaviour takes place, where trajectories return close to $\mathcal{S}$, staying there for long periods of time.

Is there any indicator of stability of the synchronised state? For any dynamical system we can evaluate the stability of a solution looking at how perturbations away from the solution evolve. If these perturbations grow then the solution is unstable but if they shrink it is stable. In a similar way in which the stability of a fixed point or of a periodic solution is examined, we look at the evolution of perturbations in direction transverse to the invariant subset, that is, the synchronisation manifold. The stability of the attractor $\mathcal{A}$ in the submanifold $\mathcal{S}$ of the phase space $\mathcal{M}$ can be described in terms of the *transverse Lyapunov spectrum*, the spectrum of exponents introduced when considering the attractor as a subset of the global phase space $\mathcal{M}$ instead of just the invariant manifold $\mathcal{S}$. For a more detailed description we forward the reader to the work of Ashwin, Buescu and Stewart [1996], citing here just two important remarks that point out the peculiarities that make the blowout bifurcation so special.

First, the Lyapunov exponents give only a linearized picture of stability. They are obtained as a Taylor series expansion of the differential equations describing

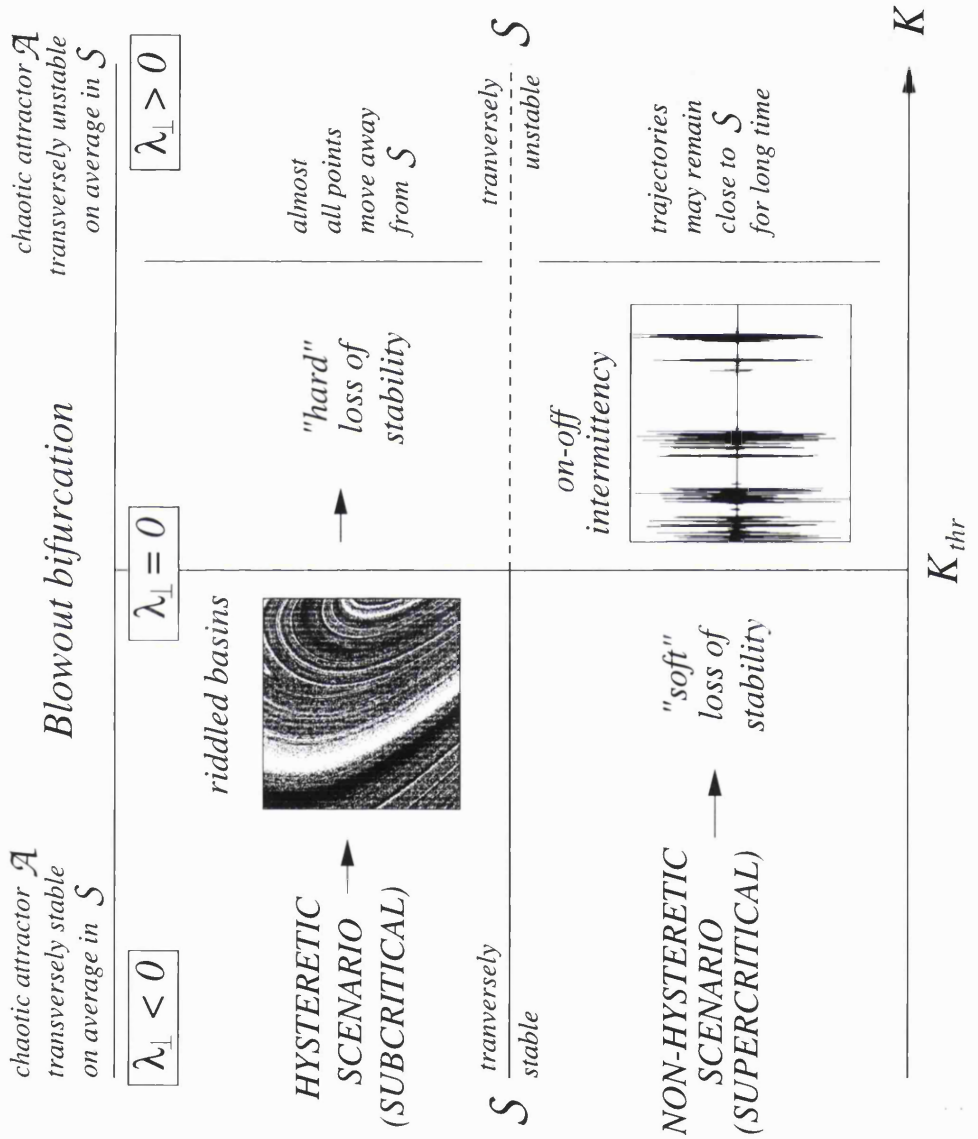

Figure 2.6: Two different scenarios for the loss of stability of a chaotic attractor $\mathcal{A}$ in an invariant subset $\mathcal{S}$ (adapted from [Ashwin *et al.* 98]).

the behaviour of perturbations transverse to the invariant submanifold, where the series is truncated at the first order. For this reason they give a faithful qualitative description of the dynamics of such perturbations only in the neighbourhood of the attractor $\mathcal{A}$. But the *global* stability of $\mathcal{A}$ in $\mathcal{S}$ will typically be determined by the dynamics far from $\mathcal{A}$, and as Ott and Sommerer noticed [1994], so far, there are at least two different types of global dynamics, as presented in the distinct scenarios in Figure 2.6: intermittency, where the local unstable manifolds fold back on $\mathcal{A}$, so the presence of fluctuations away from $\mathcal{A}$ that are forced to return back to $\mathcal{A}$, and riddled basins, where the dense set of unstable manifolds are contained in the basin of a second, distinct attractor. Another important remark is directed at the nature of the blowout bifurcation. Lyapunov exponents are defined in terms of a measure, so that they are almost everywhere constant (thus removing the spatial dependence), when computed with the stable measure, the measure whose support is the stable attractor. In the case of a chaotic attractor this is the natural invariant measure, but embedded in a chaotic attractor there is an uncountable set of unstable periodic orbits. Invariant measures are not unique. Associated with each unstable periodic orbit embedded in the chaotic attractor is a Dirac ergodic measure whose support is the orbit. Now, each ergodic measure carries its own Lyapunov exponent, so the question of stablility in the transverse direction arises independently for every ergodic measure supported in the chaotic attractor. The scenario is now quite clear: it is possible that two different periodic solutions may have different degrees of transverse stability, even different from the one of the chaotic attractor. If the maximum transverse exponent, computed with the natural measure, is positive it means that the attractor $\mathcal{A}$ is unstable in $\mathcal{S}$, but it is possible that the same exponent computed along some unstable periodic orbits embedded in $\mathcal{A}$ could be negative. These periodic orbits, unstable in the manifold $\mathcal{S}$, are nevertheless transversely stable, thus forcing the dynamical evolution to move towards $\mathcal{S}$, when the trajectory gets close to their stable manifolds. In this condition, transversely attracting trajectories can be embedded into a chaotic set (now a chaotic saddle) which is repelling only "on average", so $\mathcal{A}$ is not a topological attractor. This is a modified version of stability, termed *weak stability* or *stability in*

the Milnor sense, from [Milnor 85], and also [Ashwin *et al.* 96, Bischi *et al.* 98].

Chapter 3

Experimental evidence of chaotic synchronisation

3.1 Chaos in electronic circuits

Chaos is a dynamic phenomenon that can arise in physical nonlinear systems of very different natures, but nowhere else is it so ubiquitous and easily observed as in electronic circuits [Thompson & Chua 95]. We can identify two main reasons for this. First, the simplicity and inexpensive nature of the devices used, and second, the physics of electronic devices is well understood, so that the modelling equations of motion are the best expression of the particular physical phenomenon. Moreover, these circuits could be integrated into LSI (Large Scale Integration) chips if practical applications should emerge.

The earliest observations of chaos in electronic circuits were in forced nonlinear oscillators, like the sinusoidally excited neon bulb relaxation oscillator (firstly studied by B. van der Pol and J. van der Mark [1927]) and the forced negative resistance oscillator [Ueda & Akamatsu 80]. But among all electronic circuits, Chua's circuit [Matsumoto 84, Chua 92] deserves a special place, for its simplicity and universality. Simple because it consists of all linear elements but one, a nonlinear resistor (Chua's diode) with a piecewise-linear $v-i$ characteristic. Universal because many characteristic features of chaotic motion (like period doubling, intermittency, torus

breakdown, etc) have all been observed in this circuit [Madan 93].

The presence of noise and inherent experimental uncertainty in the definition of physical parameters make the task of an exact comparison between experimental and numerical results unfeasible. Although the overall scenario may be *qualitatively* comparable, particular thresholds, basin boundaries, bifurcations, may be *quantitatively* hard to locate. On the other hand, it is quite common for the behaviour of a chaotic circuit to be affected by the perturbation introduced by the switching mechanism at instant $t = 0$, when a rough switch-on takes place. This restricts the reproducibility of a particular experimental situation, especially when a specific initial condition is required to be set up.

3.2 Chua's circuit

In Fig. 3.1 we show a schematic representation of a single Chua circuit [1], whose experimental setup folllows the description given in [Kennedy 92]. The equations of motion representing the circuit are

$$\begin{cases} C_1 \frac{dv_1}{dt} = \frac{1}{R}(v_2 - v_1) - f(v_1) \\ C_2 \frac{dv_2}{dt} = \frac{1}{R}(v_1 - v_2) + i_L \\ L \frac{di_L}{dt} = -v_2 - R_0 i_L \end{cases} \tag{3.1}$$

where v_1, v_2, and i_L are, respectively, the voltages across capacitors C_1 and C_2, and the current flowing across inductor L. As usual, R and R_0 are the resistance at the top of the circuit and the internal resistance of the inductor. In the Eqs. (3.1), $f(v_1)$ is the piecewise linear function

$$f(v_1) = G_b v_1 + \frac{1}{2}(G_a - G_b)(|v_1 + B_p| - |v_1 - B_p|) \tag{3.2}$$

where B_p is the breakpoint and G_a and G_b are the slopes of the linear parts beyond the breakpoints. The circuit set-up has been assembled at the Dipartimento di Scienze Fisiche at the University of Cagliari, Italy, where the experiment took

[1] This circuits was originally called the *double-scroll circuit* [Matsumoto 84], a denomination sometimes still in use.

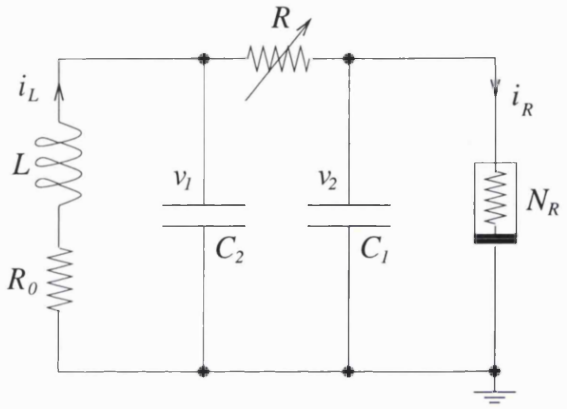

Figure 3.1: Schematic representation of the Chua's oscillator. The Chua's oscillator consists of a linear inductor L with series resistance R_0, a linear resistor R, two capacitors C_1 and C_2, and a nonlinear resistor N_R.

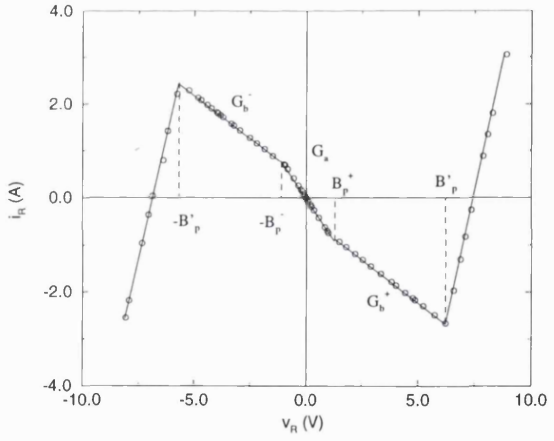

Figure 3.2: Measured $v - i$ characteristic of the nonlinear resistor N_R. The circles represent the experimental points, while the solid line represents the numerical fit used to extract the parameter values. In the negative slope regions, the inner part has slope G_a, while for the outer part the slope is $G_b^{\pm}$. For higher $|v_R|$-values the slope becomes positive, as for every physical realizable nonlinear resistor. The fitted values revealed that $G_b^+ \neq G_b^-$ and $B_p^+ \neq B_p^-$, so that the characteristic is asymmetric.

Parameters	Experimental
C_1	$(10.03 \pm 0.02)nF$
C_2	$(91.32 \pm 0.02)nF$
L	$(18.70 \pm 0.05)mH$
R_L	$(2.600 \pm 0.001)\Omega$
G_a	$(-0.725 \pm 0.004)mS$
G_b^+	$(-0.370 \pm 0.004)mS$
G_b^-	$(-0.371 \pm 0.004)mS$
B_p^+	$(1.045 \pm 0.005)V$
B_p^-	$(0.957 \pm 0.005)V$

Table 3.1: Experimental values used in the circuit set up.

place under the supervision of Prof. Guido Pegna. With the circuit, a device able to select the initial voltages $v_1(0)$ and $v_2(0)$ was prepared, that enabled us to map the basins of attraction for multistable solutions in the circuit [Pegna *et al.* 99]. We characterized the circuit by measuring all its parameters, and we found the values reported in Tab. 3.1. The experimentally determined $v - i$ characteristic of Chua's Diode is shown in Fig. 3.2, with the experimental points represented by open circles. The solid line represents the numerical fit used to derive those values present in Tab. 3.1; the fitting operation revealed to us that the $v - i$ characteristic is slightly asymmetric, presumably due to slight differences between the positive and negative saturation voltages of the amplifiers used in our circuit, so for parameters in the formula (3.2) we use G_b^+, B_p^+, or G_b^- and B_p^-, whether $v_1(t)$ is positive or negative. The asymmetry is not pronounced for $G_b^{\pm}$ which, according to the data in Tab. 3.1, are equal within the experimental uncertainty, but this is not the case for $B_p^{\pm}$, whose difference is larger that the uncertainty associated with the measurement.

A better match between positive and negative slopes of the $v - i$ characteristic could likely be obtained by the use of better quality operational amplifiers, such as, for instance, model AD712 by Analog Devices.

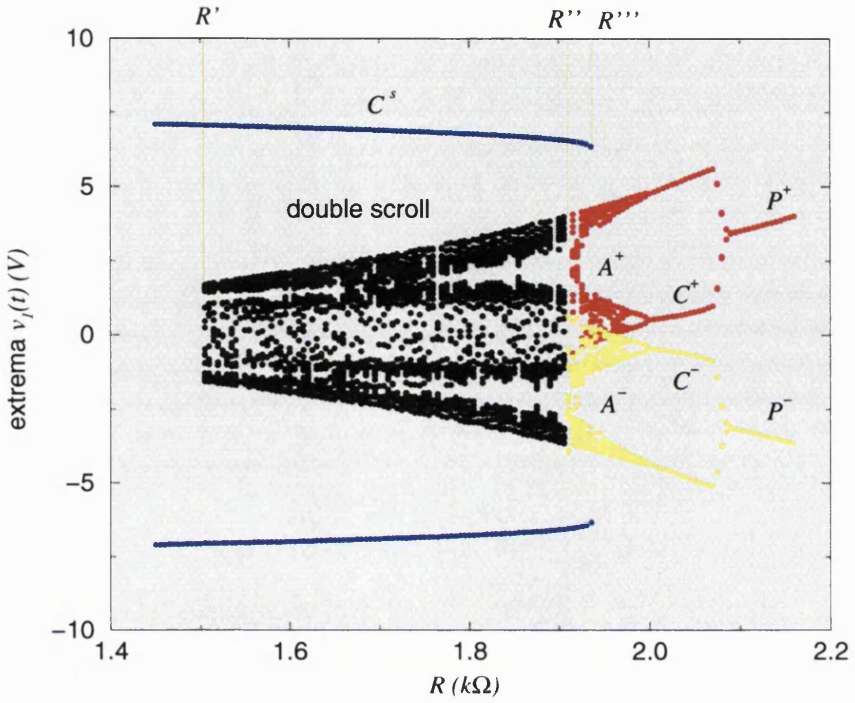

Figure 3.3: Schematic bifurcation diagram of the Chua's circuit, Eqs. (3.1), obtained by sampling, for several values of $R \in [1.45, 2.15]$ the relative maxima and minima of the time history of $v_1(t)$. The different colours show all qualitatively different solutions. The black points belong to the double-scroll chaotic attractor, in the interval $R \in [R', R'']$. In this range of R-values, the double-scroll attractor and the large periodic solution $\mathbf{C}^s$ (blue points) coexist. The red and yellow points belong, respectively, to $\mathbf{A}^+$ and $\mathbf{A}^-$ just after the crises in R'', so in the small interval $R \in [R'', R''']$ the three solutions $\mathbf{A}^\pm$ and $\mathbf{C}^s$ coexist. Finally, the red and yellow branches undergo a reverse period-doubling sequence in increasing R, to $\mathbf{C}^\pm$ and $\mathbf{P}^\pm$.

between the simulated flow and the output of the circuit showed a good agreement, as the comparison in Figure 3.4 suggests. Figure 3.3 shows the bifurcation diagram of Chua's circuit, Eqs. (3.1), in the interval $R \in [1.45, 2.15] k\Omega$. The different colours identify different coexisting solutions of Eqs. (3.1). The black points form the *double-scroll* chaotic attractor, ranging in the interval $R \in [R', R'']$. This attractor coexists, for a large interval of R-values, with a large-amplitude periodic solution, which we label $\mathbf{C}^s$, represented with blue points in Fig. 3.3. The double-scroll attractor loses its stability at R' with trajectories subsequently converging towards $\mathbf{C}^s$, and at R'' through a crises [Ott 93] giving birth to two new chaotic

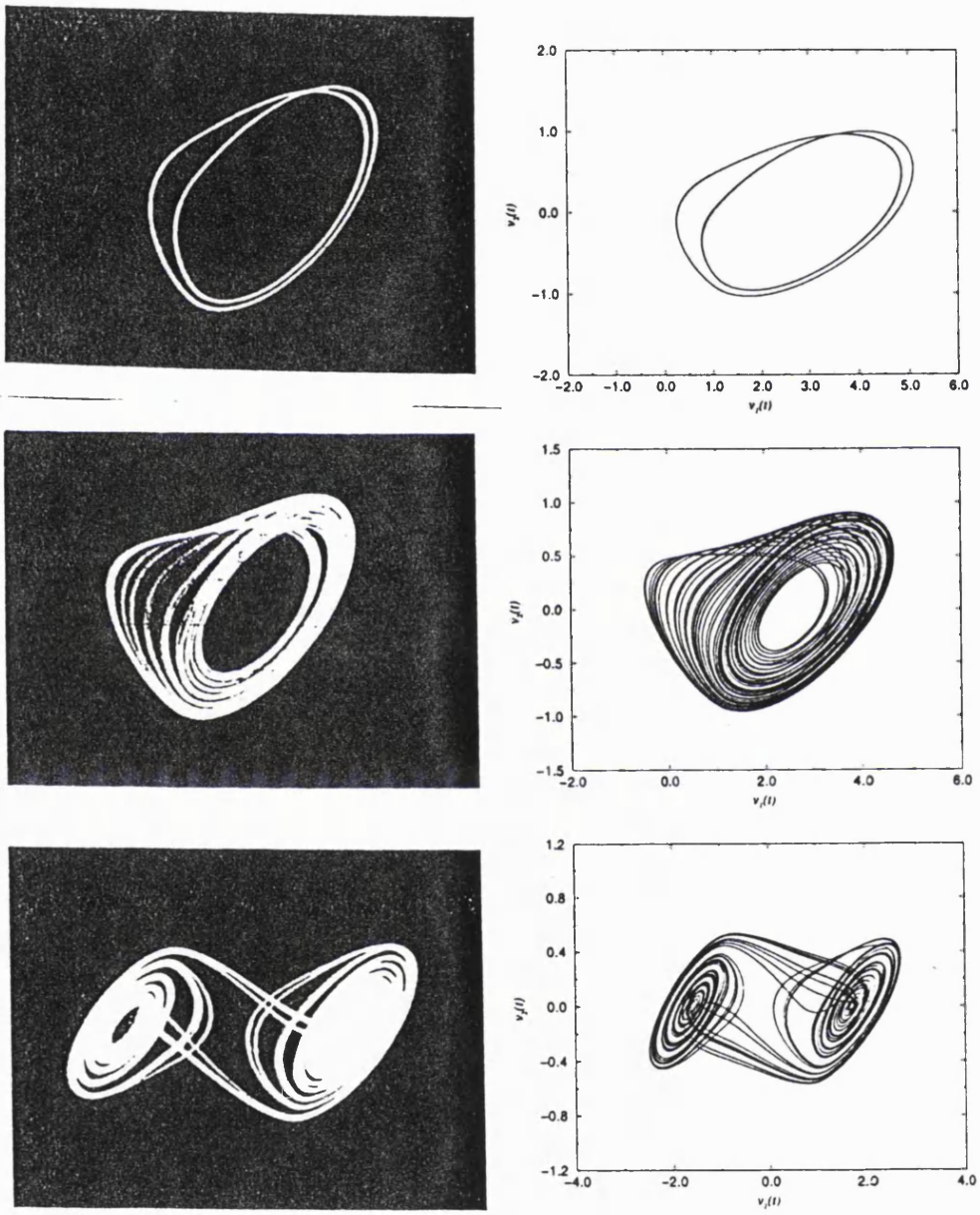

Figure 3.4: Comparison between the output from the experimental circuits (on the left) and the numerical simulations (on the right) for the cases $R = 1.985k\Omega$ (periodic case), $R = 1.93k\Omega$ (single scroll $\mathbf{A}^+$ chaotic attractor, and $R = 1.690k\Omega$ (double scroll chaotic attractor).

towards $\mathbf{C}^s$, and at R'' through a crises [Ott 93] giving birth to two new chaotic solutions called *single-scroll* attractors. We label these attractors $\mathbf{A}^{\pm}$, whether the attractor stays mostly in the positive ($\mathbf{A}^+$) or negative ($\mathbf{A}^-$) v_1 axis. In Figure 3.3, $\mathbf{A}^+$ and $\mathbf{A}^-$ are represented, respectively, by red and yellow points. At point R''' there is a bifurcation in which the large-amplitude periodic solution $\mathbf{C}^s$ loses its stability, giving way to one of the two chaotic attractors $\mathbf{A}^{\pm}$. As the resistance R increases, the chaotic single-scroll solutions experience a reverse period-doubling bifurcation sequence, until the periodic solutions $\mathbf{C}^{\pm}$, and the two bistable fixed points gain stability along the way.

To show a first example of the comparison between the output from the experimental circuits and the numerical simulation of Eqs. (3.1), Figure 3.4 shows the respective outputs for three different measured values of the resistance R of the circuit. On the left hand side of the figure we show photographs from the trace of the oscilloscope of the signals coming from v_1 and v_2, the voltages at the ends of the capacitors C_1 and C_2, respectively, for the values of the resistance R chosen as $R = 1.985k\Omega$ (periodic case), $R = 1.93k\Omega$ (single scroll $\mathbf{A}^+$ chaotic attractor, and $R = 1.69k\Omega$ (double scroll chaotic attractor). The right hand side we show the numerically simulated trajectories of Eqs. (3.1) for the same values of the parameters. The comparison indicates a good agreement between the two.

3.3 The coupled circuits

We proceed now to the coupling of two Chua's circuits. We will study the situation both numerically and experimentally, and compare the two situations. We obviously know that if the equality of the parameters is a necessary condition for the synchronised behaviour to exist, this situation is certainly not reliable in practice, since the equality of two real components is always defined within the experimental uncertainly of the measurement which is unavoidable. Anyway, if the difference in parameters is small enough we hope we can reach a certain degree of synchronisation between the two circuits. As we stated at the beginning of this Chapter, the physics of electronic circuits is well understood, and even the simplest

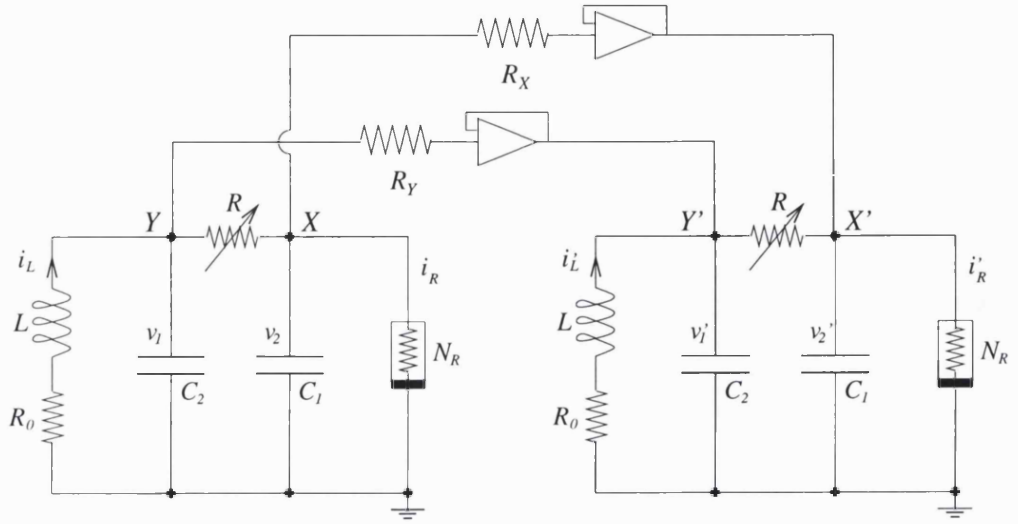

Figure 3.5: Two unidirectionally coupled Chua's circuits, either via the XX' or YY' points.

measurement techniques (for instance, with bridges) are able to give satisfactory results.

We start with Eqs. (3.1) coupled via a unidirectional coupling scheme as schematically pictured in Fig. 3.5, whose equations of motion are

$$\begin{cases} C_1 \frac{dv_1}{dt} = \frac{1}{R}(v_2 - v_1) - f(v_1) \\ C_2 \frac{dv_2}{dt} = \frac{1}{R}(v_1 - v_2) + i_L \\ L \frac{di_L}{dt} = -v_2 - R_0 i_L \\ C_1 \frac{dv_1'}{dt} = \frac{1}{R}(v_2' - v_1') - f(v_1') - \frac{1}{R_X}(v_1' - v_1) \\ C_2 \frac{dv_2'}{dt} = \frac{1}{R}(v_1' - v_2') + i_L' - \frac{1}{R_Y}(v_2' - v_2) \\ L \frac{di_L'}{dt} = -v_2' - R_0 i_L' \end{cases} \tag{3.3}$$

assuming that all parameters are equal within the experimental uncertainty. Whether we set $1/R_Y = 0$ or $1/R_X = 0$, we will deal with what is known in literature as x-coupling or y-coupling, alternatively. We will not treat any coupling from the i_L variable, because it occurs when there is mutual induction between the two inductors that, by its own definition is first of all not unidirectional, and second, it does not lead to any invariant subset.

3.3.1 Synchronisation by y-coupling

Let us now set $1/R_X = 0$, which corresponds to the coupling of the two circuits via the points YY' only (see Fig. 3.5). Once the coupling has been set up, we locate the transition from desynchronised motion to a synchronised one, in lowering the value of the resistance R_Y. We start our investigations considering parameters for which the uncoupled circuits display periodic motion, using the periodic solution for which $R = 1.985k\Omega$, shown at the top left hand side of Figure 3.4. The situation is summarized in Figure 3.6. At the top of the Figure is shown a plot with the composition of the motions $v_1(t)$ and $v_1'(t)$ in the case of zero coupling ($1/R_Y = 0$). We do not have an experimental counterpart of this Figure because we realized that even the slightest perturbation of this situation was able to produce synchronised motion (so the trace in the oscilloscope on the bottom of this Figure). Although the real inductors in the two circuits have been accurately shielded, and the connection between the nodes XX' set at infinte resistance, we could not be sure that a very small influence could have been exerted between the two, but large enough to produce the transition.

In the middle of Figure 3.6 shows the composition of the same motions for the case of synchronised motion, that we numerically found to be stable for values of the coupling parameter $1/R_Y \geqslant 0.0015mS$, corresponding to resistances below $R_Y \simeq 650k\Omega$.

We turn now to a case of synchronisation of two coupled Chua's circuits when the motion of the uncoupled units is chaotic. We choose the double-scroll chaotic attractor as base dynamics that is visible at the bottom of Figure 3.4. The diagram in Figure 3.7 represents values of the *local average distance* between the trajectories (v_1, v_2, i_L) and (v_1', v_2', i_L') generated by Eqs. (3.3) when $1/R_X = 0$, and several values of R_Y [2]. The way these data are generated is explained in Figure 3.8. First of all, a time series of the Euclidean distance is numerically generated via Eqs. (3.3). Then, a *local maximum* is selected in the time series of

[2]The Euclidean distance between the trajectories (v_1, v_2, i_L) and (v_1', v_2', i_L') is, by definition, a quantity whose dimension is spurious, because it comes from an addition between voltages and currents.

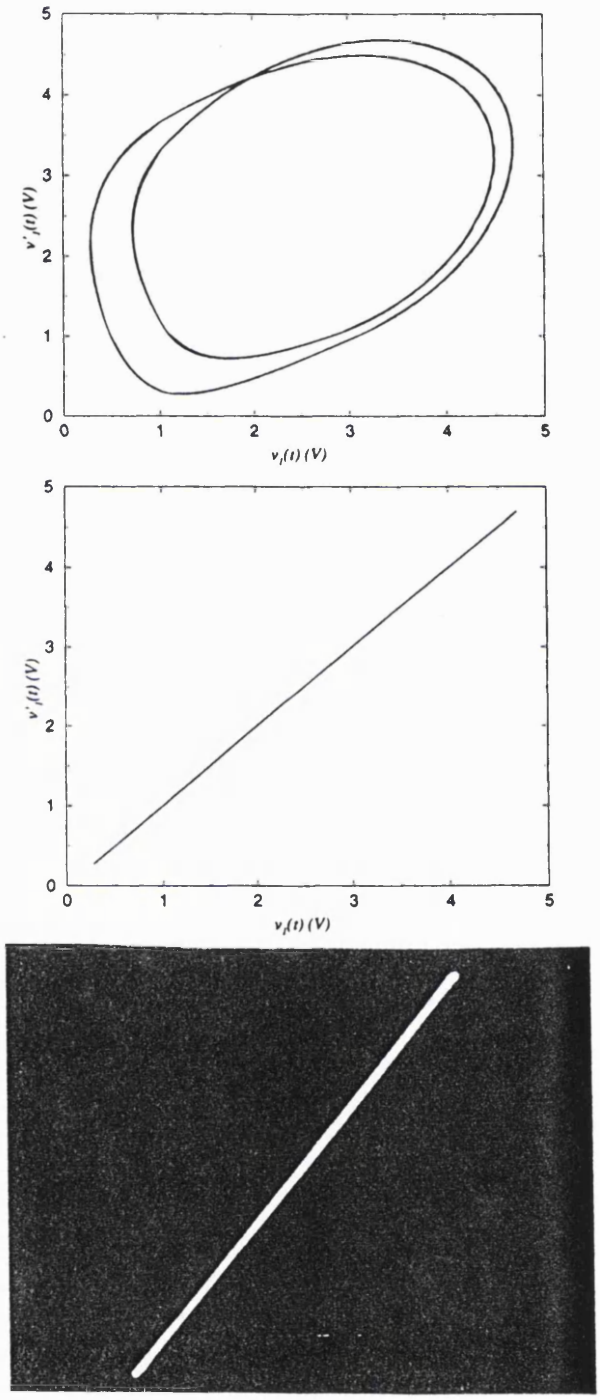

Figure 3.6: Top: Composition of the motions $v_1(t)$ and $v_1'(t)$ for two uncoupled $(1/R_Y = 0)$ periodic orbits, as in the top of Figure 3.4, of the Chua's equations. Middle: Synchronised behaviour of the coupled model, stable for values of the coupling constant $1/R_Y \geq 0.0015mS$. Bottom: Trace of the oscillator for the compositions of the signals from Y and Y' for the coupled periodic orbits. In the real circuit synchronisation was produced even by the slightest perturbation of the uncoupled circuits.

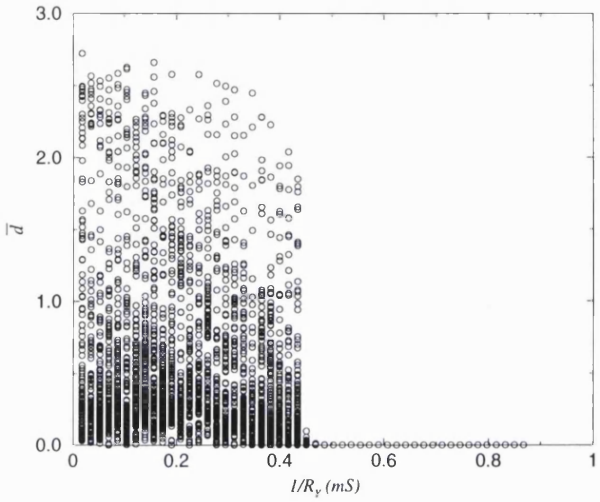

Figure 3.7: Local average distance between the trajectories of the drive and the response circuits, as simulated from Eqs. (3.3) for $R = 1.690k\Omega$, giving a double scroll chaotic attractor. The visible transition to the synchronised state is located at $1/R_Y \simeq 0.47mS (R_Y \simeq 2.13k\Omega)$.

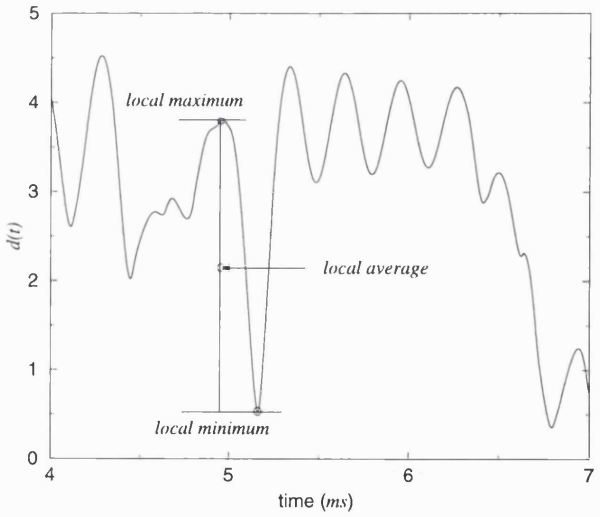

Figure 3.8: Schematic diagram of how to compute the local average distance.

$d(t)$, and it is averaged with the subsequent *local minimum*, as explained in Figure 3.8, so generating all *local averages* $\overline{d}(t)$, represented in Figure 3.7 for several values of R_Y across the transition to synchronised state. Figure 3.7 reveals that the transition to synchronisation, for the model used to simulate the dynamical evolution of the circuit, is located at $1/R_Y \simeq 0.47mS$, corresponding to $R_Y \simeq 2.1k\Omega$. Experimentally, a similar value has been found for the threshold of coupling resistance, namely, of $R_Y = 2.05k\Omega$, this confirming the suitability of the equations model we used.

3.4 Transverse Lyapunov exponents

We now turn our attention to the computation of the transverse Lyapunov spectrum for the two Chua's circuit coupled through the YY' points only. We will use the approach we have already outlined in the first Chapter, that is, to average the eigenvalues of the Jacobian matrix for the difference equation, (1.2-1.4). Indicating with $\Delta \boldsymbol{r} = \boldsymbol{r}' - \boldsymbol{r} = (\Delta v_1, \Delta v_2, \Delta i_L)$, where $\boldsymbol{r} = (v_1, v_2, i_L)$, and $\boldsymbol{r}' = (v_1', v_2', i_L')$, we can write down the differential equation corresponding to (1.1), as

$$\begin{cases} \dfrac{d\boldsymbol{r}}{dt} = \boldsymbol{F}(\boldsymbol{r}) \\ \dfrac{d\boldsymbol{r}'}{dt} = \boldsymbol{F}(\boldsymbol{r}') - K(\boldsymbol{r}' - \boldsymbol{r}). \end{cases} \tag{3.4}$$

where the functional form $\boldsymbol{F}$ is given by the Eqs. (3.1). K is the matrix with $K_{22} = 1/R_Y$ the only element different from zero. From this coupling form we derive the equations of motion for the difference

$$\begin{cases} C_1 \dfrac{d\Delta v_1}{dt} = \dfrac{1}{R}(\Delta v_2 - \Delta v_1) - h(\boldsymbol{r}, \Delta \boldsymbol{r}) \\ C_2 \dfrac{d\Delta v_2}{dt} = \dfrac{1}{R}(\Delta v_1 - \Delta v_2) + \Delta i_L - \dfrac{\Delta v_2}{R_Y} \\ L \dfrac{d\Delta i_L}{dt} = -\Delta v_2 - R_0 \Delta i_L \end{cases} \tag{3.5}$$

where $h(\boldsymbol{r}, \Delta\boldsymbol{r}) = [f(v_1+\Delta v_1) - f(v_1)]$ is the only term dependent on the equations of the driving term. The corresponding Jacobian matrix is given by

$$DH(\boldsymbol{r})|_{\Delta\boldsymbol{r}=\mathbf{0}} = \begin{pmatrix} -\frac{1}{C_1}\left(\frac{1}{R} + f'(v_1)\right) & \frac{1}{RC_1} & 0 \\ \frac{1}{RC_2} & \frac{1}{C_2}\left(\frac{1}{R_Y} - \frac{1}{R}\right) & \frac{1}{C_2} \\ 0 & -\frac{1}{L} & -\frac{R_0}{L} \end{pmatrix} \tag{3.6}$$

because $\partial h(\boldsymbol{r}, \Delta\boldsymbol{r})/\partial\Delta v_1|_{\Delta\boldsymbol{r}=\mathbf{0}} = f'(v_1)$. The averaged eigenvalues of the matrix (3.6) over a typical orbit of Eqs. (3.3) are the transverse Lyapunov exponents (TLEs). Several methods exist to compute all characteristic exponents from the matrix (3.6), for example in [Shimada & Nagashima 79, Geist *et al.* 90], but for our purposes we only need to compute the largest of all three, saving considerable computational effort, via the numerical integration of the first equation of the system (3.4) with the

$$\frac{d\Delta\boldsymbol{r}}{dt} = DH(\boldsymbol{r})|_{\Delta\boldsymbol{r}=\mathbf{0}} \cdot \Delta\boldsymbol{r}$$

and seek for the leading eigendirection of $\| \Delta\boldsymbol{r} \|$.

A computation of the the largest TLE $\lambda_\perp$ for several values of $1/R_Y$ across the transition to the stability of the synchronised state is shown in Figure 3.9. The value of the largest TLE crosses zero in lowering the coupling resistance at approximately $1/R_Y \simeq 0.47mS \simeq 2.13k\Omega$, in very good agreement with the numerical evolution on the Euclidean distance shown in Figure 3.7, but most of all, with the experimental results reported at the end of the previous section.

3.5 Parameter mismatch

As stated before, the equality of the components of the two circuits is bounded to the experimental uncertainty associated with the measurement process. This is an unavoidable source of error that even if does not seem to influence significantly the previously shown comparison between experimental and numerical outputs, certainly makes a difference in the analytical treatment of the problem. Strictly speaking, the simple invariant subset $\boldsymbol{r} = \boldsymbol{r}'$ only exists when the functional form $\boldsymbol{F}$

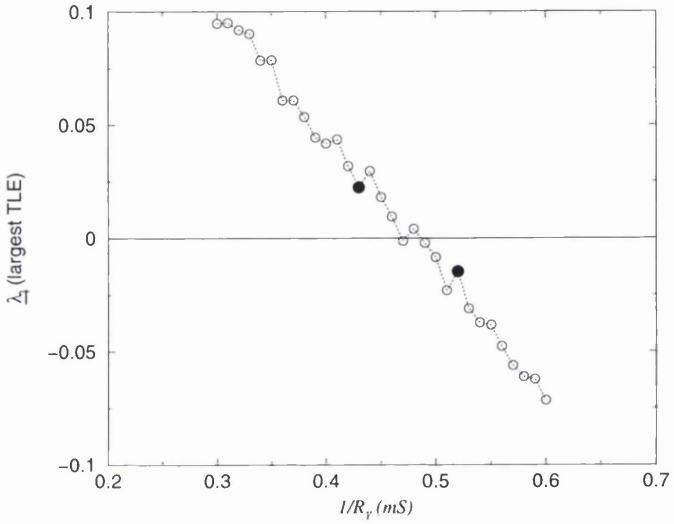

Figure 3.9: Transverse Lyapunov exponents $\lambda_\perp$ for two y-coupled Chua's circuit as in Eqs. (3.3) with $1/R_X = 0$. The two black circles correspond to the two time series shown in Figure 3.10.

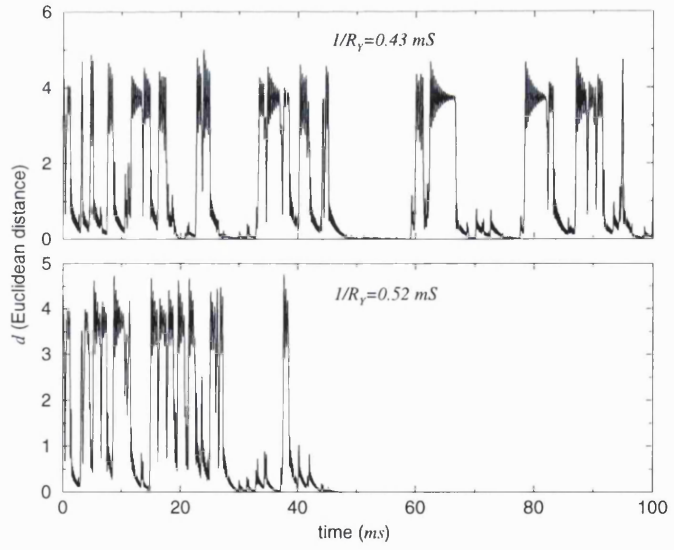

Figure 3.10: Evolution of the Euclidean distance for the two cases corresponding to the black circles in the previous Figure. The characteristic on-off intermittent evolution is the stable output for $1/R_Y = 0.43mS$ (top), while is only a transient state for $1/R_Y = 0.52mS$ (bottom).

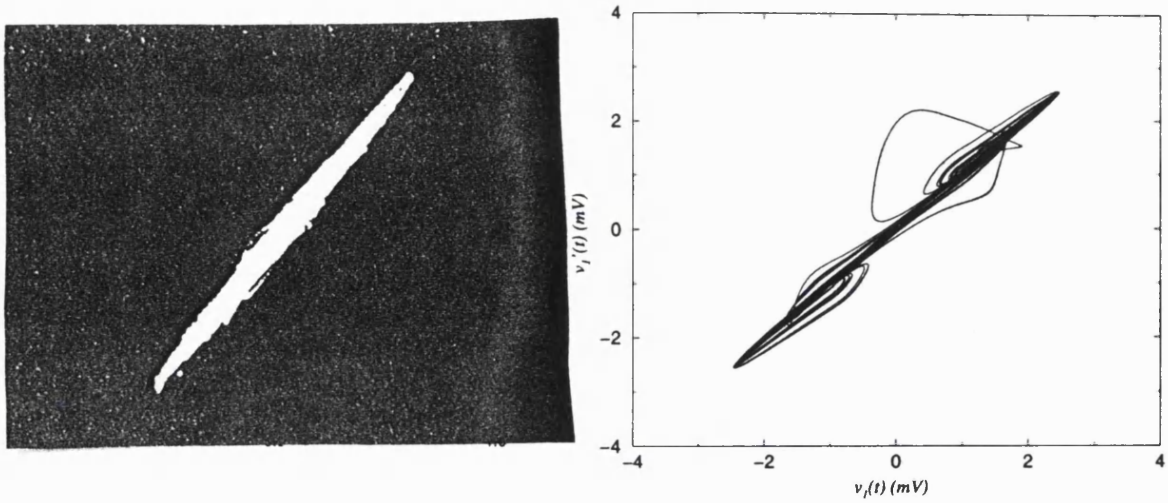

Figure 3.11: Left: Experimental composition of the signals $v_1(t)$ and $v_1'(t)$ for the coupled Chua's circuits via the YY' points. Between the driving circuit and the response one there is a mismatch in the resistance R of 20Ω. Right: Numerical counterpart of the left picture.

in Eqs. (3.4) is the same for both circuits, *i.e.* when all parameters in the equations of motion of the two coupled Chua's circuits are exactly the same. Despite this analytical reality, experimentally it is not a problem to synchronize two coupled circuits, and numerically the trajectory of the extended system will converge to a region very close to $\boldsymbol{r} = \boldsymbol{r}'$, in presence of both mismatch of the parameters and white additive noise, provided that both are reasonably small.

For the coupled Chua's circuits, we realized this situation by imposing a different between the two resistances R, of the two circuits. We set the driving circuit with a resistance $R = 1.690k\Omega$, while the response circuit was set to $R' = 1.710k\Omega$, still having a chaotic double scroll as a stable response. The mismatch between the two is 20 Ω, and the coupling resistance is set to $1/R_Y = 1.0mS$. The numerical simulation of the trajectory reproduces quite well the experimental output, nevertheless showing some bursts which significantly deviate from the line $v_1(t) = v_2(t)$, but whose excursion is so fast that they result hardly visible to the eye.

Chapter 4

Before the bifurcation

The presence of an unstable invariant subset, *i.e.* when $\lambda_\perp > 0$, still influences the dynamics of the coupled oscillators for coupling parameter values before the bifurcation which leads to synchronisation. Even though the subset is unstable on average, there may still be local zones of transverse attraction that may cause temporary convergence towards $\mathcal{S}$, as discussed in the case of *on-off intermittency* in the Chapter 2. If we consider two identical (but the discussion also generally holds for slightly different) continuous (or discrete) systems performing chaotic motion, the ergodicity of the trajectory means that the systems may eventually become very close to each other for some time, regardless of any dissipative mechanism due to a coupling function. The presence of dissipation in the transverse direction is an additional means to push the trajectory towards the invariant subset $\mathcal{S}$, and the stronger the dissipation (if we measure it using the largest TLE), the smaller the distance, on average, between the trajectory and $\mathcal{S}$ within a fixed time interval.

There are zones in the parameter space for which the distance between the trajectory and $\mathcal{S}$ may be small enough to be comparable to the roundoff error of the computing machine. In this situation it is possible that the results of a numerical experiment can be misleading. Some authors, for instance [Shuai *et al.* 97], have reported the presence of synchronised behaviour with positive TLE (the authors preferred the terminology "conditional Lyapunov exponent"), while on-off intermittent behaviour, with very "deep" laminar phases, was the real output of the

dynamics.

In the rest of this chapter we will consider simple discrete maps, whose simplicity sometimes provides us with a statistical description of their macroscopic properties, such as the probability density. We will see whether or not these analytical characteristics can help us to more fully understand the synchronisation process.

4.1 Dynamics of coupled maps

Consider the case of two simple one dimensional maps $x_{n+1} = f(x_n)$ unidirectionally coupled

$$\begin{cases} x_{n+1} = f(x_n) \\ y_{n+1} = f(y_n) - K[f(y_n) - f(x_n)] \end{cases} \tag{4.1}$$

where the x system is effectively driving the y system, with no feedback present. K is taken to be a real parameter that tunes the strength of the nonlinear coupling between the two systems. We consider f to be a map on the unit interval and $K \in [0, 1]$. Under these restrictions, initial conditions within the unit square will always stay within the unit square. The invariant subset, denoted $\mathcal{S}$, corresponds to the exact equality of the coordinates $x_n = y_n$. From Eqs. (4.1), if a trajectory converges onto $\mathcal{S}$, it will remain in the invariant subset forever, regardless of the dynamical evolution of the x system, performed in $\mathcal{S}$. It is easy to derive a relationship between the transverse Lyapunov exponent and the coupling parameter K. Using the difference variable $z_n = y_n - x_n$, the second equation in (4.1) can be rewritten as

$$z_{n+1} = (1 - K)[f(x_n + z_n) - f(x_n)] \tag{4.2}$$

that in the limit $z_n \to 0$ yields the linearized equations

$$\begin{cases} x_{n+1} = f(x_n) \\ z_{n+1} = (1 - K)f'(x_n)z_n. \end{cases} \tag{4.3}$$

The second equation represents the dynamics in the direction transverse to $\mathcal{S}$. The rate of growth of perturbations in this direction is simply computed as

$$\frac{1}{n}\log\left|\frac{\delta z_{n+1}}{\delta z_0}\right| = \log(1-K) + \frac{1}{n}\sum_{i=0}^{n}\log|f'(x_i)|,$$

that is, in the limit $n \to \infty$,

$$\lambda_\perp = \log(1-K) + \Lambda, \tag{4.4}$$

where Λ is the Lyapunov exponent related to the motion of the y system. The blowout bifurcation [Ott & Sommerer 94] is defined as the point in the parameter space $K = K_{thr}$ say, for which $\lambda_\perp = 0$, so that from (4.4),

$$K_{thr} = 1 - e^{-\Lambda}, \tag{4.5}$$

An *apriori* knowledge (analytical or numerical) of Λ leads to a known value for the threshold K_{thr}.

4.1.1 Coupled tent maps

As an illustrative example, we consider a pair of coupled maps where the function $f(x)$ in Eqs. (4.1) is given by the tent map

$$f(x) = \begin{cases} x/c & \text{if } 0 \le x < c \\ (1-x)/(1-c) & \text{if } c \le x \le 1. \end{cases} \tag{4.6}$$

The synchronised behaviour in two linearly coupled maps (4.6) has been previously treated in [Hasler & Maistrenko 97]. This map is chosen since in this particular case the natural invariant density is given by $\rho(x) = 1$ for all $c \in (0,1)$ up to a set of measure zero, so that the map fills the unit interval uniformly. In other words, the natural measure of the map (4.6) is the Lebesgue measure. The Lyapunov exponent of this map as a function of c is expressed as

$$\Lambda(c) = -c\log c - (1-c)\log(1-c), \tag{4.7}$$

and from relation (4.5) we have

$$K_{thr}(c) = 1 - e^{c\log c + (1-c)\log(1-c)} = 1 - c^c(1-c)^{1-c}. \tag{4.8}$$

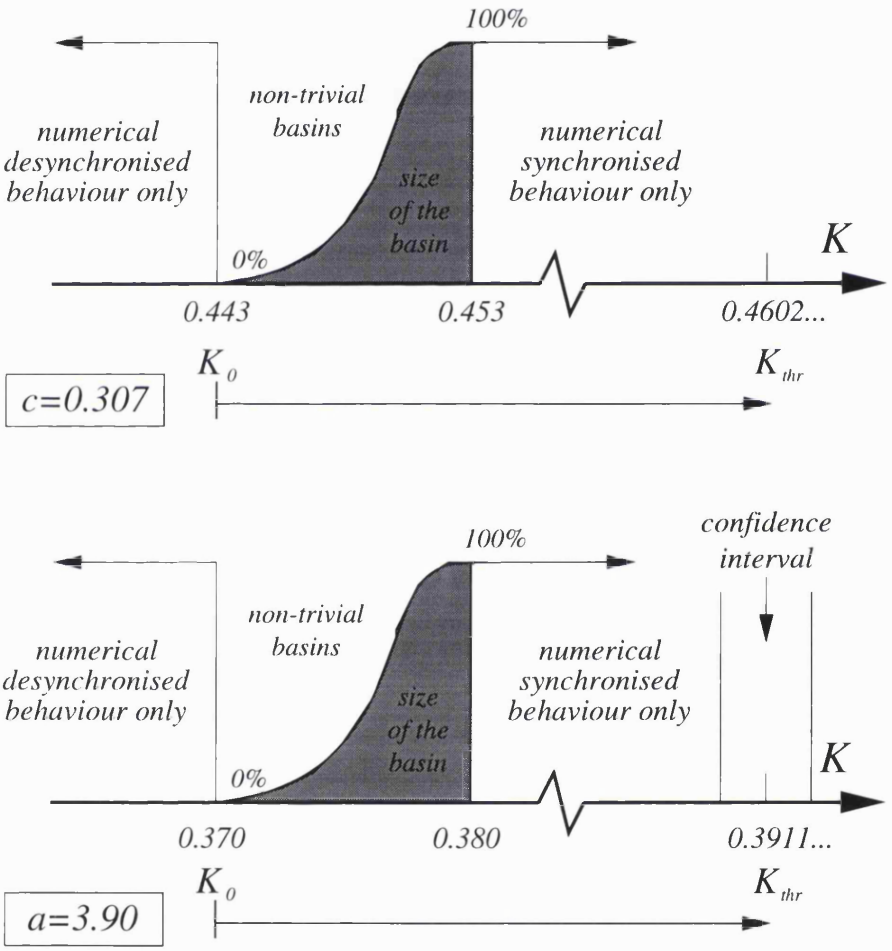

Figure 4.1: Schematic representation of events as the coupling parameter K is increased in the coupled tent maps system with $c = 0.307$ (top), and for the logistic map with $a = 3.9$ (bottom).

Although a numerical evaluation of Λ gives us the quantity predicted by the formula (4.7), the blowout bifurcation point does not always correspond with the numerical change of transverse stability K_n, the value we measure in a particular numerical simulation for an individual trajectory.

Initially consider a fixed, but typical value of $c = 0.307$ for which, from the relations (4.7) and (4.8), $\Lambda = 0.6166...$, and $K_{thr} = 0.4602....$ For an arbitrarly chosen initial condition the numerical value detected for the convergence onto $\mathcal{S}$ was found to be $K_n \simeq 0.4470$, which is before the predicted *exact* value of K_{thr}, so we say that the synchronisation here is *premature* [1]. This value of K_n is valid only for this particular numerical experiment; a different initial starting point will probably result in a slightly different numerical threshold, but always before K_{thr}. A diagram representing the events occurring in increasing the value of K is schematically drawn in Figure 4.1. In this diagram, instead of a single trajectory, a grid of 49×49=2401 different initial points uniformly distributed in the unit square (0,1)×(0,1) is considered. Let K_0 be the smallest value of K for which at least one of this grid of initial conditions achieves synchronisation, and denote K_1 to be the smallest value of K where all initial conditions in the unit square produce synchronised motion. For each initial condition the map has been iterated at most 10^6 times. In the case of the coupled skewed tent map, the numerical value K_n is always lower than K_{thr}, and for typical initial conditions synchronisation first occurs in the interval $[K_0, K_1] \simeq [0.443, 0.453]$, hence the synchronised state within this interval has a non-trivial numerical "basin" of attraction; some initial conditions will converge onto $\mathcal{S}$, others may not. For $K \simeq K_0$ the percentage of initial conditions ending below the level of the roundoff error is so low that we expect the "premature" synchronisation to be a very rare event, even in a very long time series. In the same Figure 4.1, a pictorial representation of this percentage is given for the number of initial points that converge onto $\mathcal{S}$ within 10^6 iterations. This percentage gives us an estimate of the "size" of the basin of attraction for

[1] The term "synchronisation" here can be quite misleading since in this case there is no neighbourhood of $\mathcal{S}$ whose initial conditions (up to a zet of zero measure) all converge onto $\mathcal{S}$, as its stability would imply.

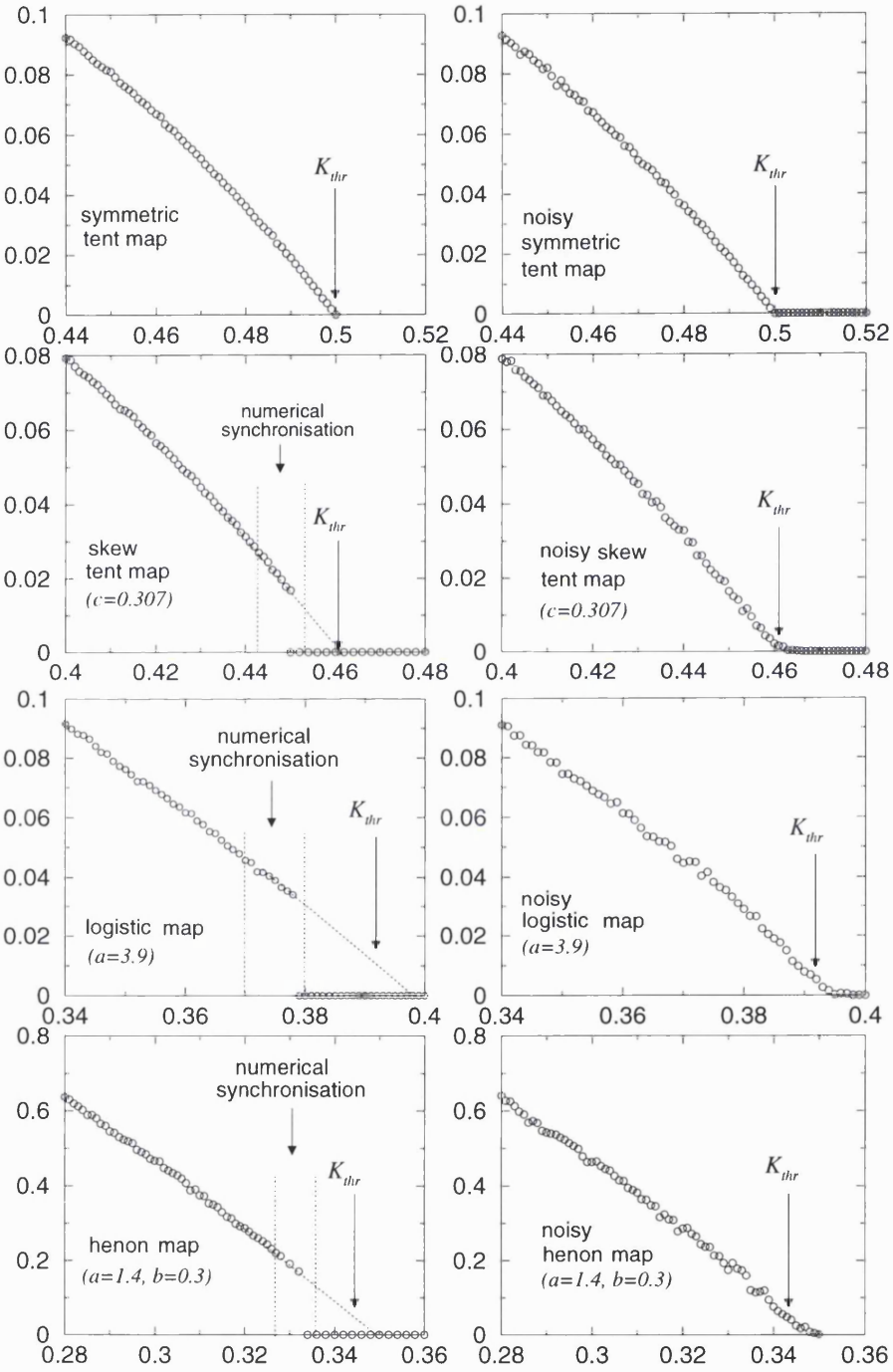

Figure 4.2: Average distance for increasing values of K for four different dynamics models. From top to the bottom, the (almost) symmetric tent map, a skew tent map ($c = 0.307$), the logistic map ($a = 3.9$), and the Henon map ($a = 1.4$, $b = 0.3$). The right column show the noisy version of the left column.

the attracting set in $\mathcal{S}$. For $K < 0.443$ no point achieves synchronisation and the basin has size zero, then its size grows, the percentage reaching the 100% at $K_1 \simeq 0.453$.

4.1.2 Other coupled Maps

Figure 4.2 shows the behaviour of the average distance in increasing K for four different maps. In addition to the already discussed skewed tent map, in this Figure are present calculations on the (almost) symmetric tent map, the skewed tent map, the logistic map and the Henon map. All pictures are determined in absence of noise. The noisy counterpart of the same numerical experiment is show in the right column, with amplitude 10^{-12}. The average distance in increasing K close to the blowout bifurcation has already shown to decrease linearly in [Ashwin *et al.* 98]. This is easily seen in the symmetric tent map, but in all other cases the linear decay is broken and slightly before the location of K_{thr} the trajectory has zero distance on average, that is, it shows synchronisation. The "premature" type of synchronisation detected in the last three examples is lost whenever a small noise term is added, in this particular case, to the response system, as all plots in the right column reveal. We discuss now the three remaining cases in more detail. No sign of "premature" synchronisation is detected for the symmetric tent map. As we already discussed in Chapter 2, the symmetric tent map is, in the numerical experiment, a skewed tent map with $c = 0.5+\varepsilon$, where $\varepsilon = 10^{-10}$. The quantity ε is small enough to have negligible effect on the local divergence of typical trajectories (as we will discuss later for the distribution of the finite-time Lyapunov exponents), but larger than the roundoff error of the computing machine, so it prevents a typical trajectory to converge towards the zero fixed point, as commonly known. The phenomenon of "premature" synchronisation can be seen in a coupled logistic map system where $f(x) = ax(1-x)$ in Eqs. (4.1). Using the value $a = 3.90$, $f(x)$ performs a chaotic motion with a maximum Lyapunov exponent numerically evaluated as $\Lambda = 0.4960$, with a standard deviation of $\sigma = 1.6 \times 10^{-4}$. This value for the Lyapunov exponent is determined by the average value found over

a sample of 100 random initial conditions, with 10^6 iterations for each initial condition. Once the value of Λ is known, we can obtain an analytic expression of the threshold of stability of the invariant subset $\mathcal{S}$ (*i.e.* the synchronised state), given by $K_{thr} = 1 - e^{-\Lambda} = 0.3911 \pm 0.0003$. In numerical simulations however synchronisation was achieved for $K_n < K_{thr}$, down to a value $K_1 \simeq 0.380$ for the whole phase space to be synchronised, using the same grid as before, and as low as $K_0 \simeq 0.370$ for at least a few initial points to become synchronised. Nevertheless, these two values of the coupling parameter are located outside the interval of confidence given by the error distribution of Λ, see the lower diagram of Figure 4.1.

As further confirmation of the presence of this roundoff induced phenomenon in coupled maps, we also consider the case of a two-dimensional mapping of the plane, the Henon map that is non-hyperbolic and invertible. The coupling used in the case of this two-dimensional mapping is a vectorial form of Eqs. (4.1). Consider the driving system to be

$$\begin{cases} x_{n+1} = g(x_n, y_n) = a - x_n^2 + by_n \\ y_{n+1} = h(x_n, y_n) = x_n, \end{cases} \tag{4.9}$$

where $a = 1.4$ and $b = 0.3$. This is one of the most frequently used examples of dynamics of a two-dimensional map that is believed to possess a chaotic attractor, see [Thompson & Stewart 86], for example. The equations of motion for the response system (x'_n, y'_n) are now

$$\begin{cases} x'_{n+1} = g(x'_n, y'_n) - A_{11}[g(x'_n, y'_n) - g(x_n, y_n)] \\ y'_{n+1} = h(x'_n, y'_n). \end{cases} \tag{4.10}$$

This form of coupling is a vector version of Eqs. (4.1), where f and K in (4.1) are substituted by (g, h) and a 2×2 matrix A_{ij} where the only nonzero element is $A_{11} = K$, respectively, in (4.10). The usual variational analysis in the neighbourhood of the invariant subset $\mathcal{S}$ allows us to find again the relation (4.4), where this time Λ is the maximum Lyapunov exponent of the Henon map.

4.1.3 Further explorations

K_0 and K_1 (with respect to K_{thr}) quantify the effect of the roundoff on the convergence of trajectories. In an ideally perfect numerical experiment, with infinite number of iterations and infinite precision, a typical initial condition will have $K_0 = K_1 = K_{thr}$. This condition is actually fulfilled in the degenerate case $c = \frac{1}{2}$ for the tent map because, as we will see later, in this case the transverse stability of every orbit (stable or unstable in $\mathcal{S}$) changes at K_{thr}, so that no local attraction exist for $K < K_{thr}$, and no local repulsion for $K > K_{thr}$. We should now ask how these two points will modify their positions in varying three parameters in the numerical experiment.

1. The precision used. What is going to happen if we use a level of roundoff closer to $\mathcal{S}$? Zhou and Lai [1998] have already shown calculations using different precision (they reported computations in single ($A = 10^{-8}$), double ($A = 10^{-16}$) and quadruple ($A = 10^{-32}$) precision). A trajectory of z_n going below the threshold of 10^{-8} in single precision is regarded to be synchronised in single precision, but not in double and quadruple. This means that the use of better precision will result in shifting the points K_0 and K_1 towards K_{thr}.

2. The number of iterations. The ergodicity of the trajectory implies that there is a nonzero probability that a typical trajectory will get as close as we want to $\mathcal{S}$, although the probability can be so small to be considered negligible, so that a very long time is needed to see convergence. Increasing the number of iterations gives more time to a trajectory to to reach the level of the roundoff, so it results in moving the points K_0 and K_1 away from K_{thr}.

3. The grid size. We used a grid of 49×49=2401 initial conditions to derive the numerical results presented. Increasing the grid size, the visible result will be to stretch the interval $[K_0, K_1]$, because additional initial conditions may converge (in a fixed number of iterations) below the roundoff error for $K < K_0$, as well as they may not converge for $K > K_1$.

So the "size" shown in Figure 4.1 does not truly refer to a real basin of attraction for the existence of different coexisting solutions, but a mere probablity of convergence of a group of initial conditions in a fixed time. It would be interesting to determine if such a "basin" has a particular structure in the y variable, where so far we have not been able to recognize any. We note, however, that this numerical artifact is not displayed by all systems undergoing a blowout bifurcation, but only to those built by coupling of identical units, because the convergence to the invariant set is monitored through the difference of the respective variables. For example, in the system (2.5), from [Lai 96], whether $f(x)$ represents a symmetric ($c = \frac{1}{2}$) or skewed ($c \neq \frac{1}{2}$) tent map, a blowout bifurcation exists for $p = e = 2.71828...$, and the $y = 0$ state is stable for $p < e$, but for $p = e + \varepsilon$ the computing machine never attributes a zero value to y, no matter how small ε is. The difference is generated by the algorithm used. Although the order of magnitude of a number can be expressed even when it is below 10^{-16}, in 16 digit precision if two numbers differ than less then 10^{-16}, they are considered to be equal. A useful trick to perform, in order to override this problem can be to substitute the original equations (4.1) by the corresponding variational equations (4.3), only when the difference $|z|$ is very small. Similar problems have been treated in [Ashwin & Rucklidge 98].

4.2 Statistical description of on-off intermittency

The smaller the dispersion around the mean of the finite-time Lyapunov exponents, the smaller are the fluctuations around the mean contraction/expansion rate, *i.e.* the behaviour described by the natural measure is most representative of the real dynamical evolution. This situation is fulfilled for Eqs. (4.1) when the coupling parameter K is large, or alternatively, when particular dynamical systems are chosen, for which chaotic behaviour is accompanied with negligible dispersion of the finite-time Lyapunov exponents. Many studies were recently devoted to understanding the distribution of the finite-time Lyapunov exponents and, of special interest, the classification of the distribution depending on the nature of the attractor. For hyperbolic sets it can be proved that the central limit

theorem holds for a number of averaged quantities, such as Lyapunov exponents, so that the density is a Gaussian function [Ott 93] while for other outputs (as the Pomeau-Manneville types of intermittency cited in Chapter 2) fluctuations lead to different density functions [Benzi *et al.* 85].

For $K \gg K_{thr}$ the average contraction rate will be strong enough to overwhelm all other contraction/expansion rates from all the other atypical solutions, but in the case $K \simeq K_{thr}$, so when $\lambda_\perp \simeq 0$, the stability/instability is weak enough that fluctuations can certainly have noticeable effects on the dynamics. An analytical description of the fluctuations cannot be mathematically formulated explicitly, but their characteristics can at least be given on average.

4.2.1 Stochastic differential equations

Consider the motion in one dimension of a particle of mass m immersed in a fluid where the only force acting on the particle is the friction force $F_c = -\alpha v$, where v is the velocity of the particle, and α is the friction coefficient. The equation of motion for the particle is $m\dot{v} + \alpha v = 0$ or, with $\gamma = \alpha/m$,

$$\dot{v} + \gamma v = 0 \tag{4.11}$$

whose solution $v(t) = v_0 e^{-\gamma t}$ describes the decay of an initial velocity v_0 to zero with an exponential decay rate. The phenomenon at the basis of the decay is the sequence of collisions that the particle experiences against the molecules of the fluid, causing a transfer of momentum mv to them.

As described by the equation above, this process is entirely deterministic, but Eq. (4.11) is valid only if the mass of the particle is so large that its velocity due to thermal fluctuations is negligible. From the law of equipartition of energy, the mean energy of a particle due to thermal fluctuations is given by

$$\frac{1}{2}m\langle v^2\rangle = \frac{1}{2}kT \tag{4.12}$$

where k is the Boltzmann constant and T is the temperature in Kelvin. For a very small mass m, the thermal velocity $v_{th} = \sqrt{\langle v^2\rangle} = \sqrt{kT/m}$ may be observable,

making Eq. (4.11) inaccurate for the description of the phenomenon. A modification used for Eq. (4.11) to take into accounts the contribution of the thermal fluctuation is to add a stochastic force $\Gamma(t)$, thus giving

$$\dot{v} + \gamma v = \Gamma(t). \tag{4.13}$$

This stochastic or *Langevin force*, whose properties will be given only in the average, arises from the unsolvability of the coupled equations of motion for all the molecules of the fluid and for the small particle. Apart from the large number of molecules involved (of order 10^{23}) we also do not have exact information on *all* the initial positions and velocities of the particle and the molecules. The stochastic force $\Gamma(t)$ "averages" the contribution of the all collisions occurring in a random fashion in the fluid, that generate the thermal energy transferred to the particle. This is the description of the so-called *Brownian motion*, whose first observations date back to 1827 by the naturalist Robert Brown, studying the erratic motion of pollen particles suspended in water. A good description can be found in [Grimmett & Stirzaker 92]. The Eq. (4.13) is a *stochastic differential equation* or, as usually referred in the physical literature, a *Langevin equation*. We can enumerate some properties of the Langevin force $\Gamma(t)$. First of all, its average over the ensemble of the systems should be zero,

$$\langle \Gamma(t) \rangle = 0,$$

justified assuming that there is not a preferred direction for any collision to occur and also derived from the requirement that the average velocity $\langle v \rangle$ should behave according to (4.11). The product of two Langevin forces at different times should have average zero for time differences $t - t'$ larger than the duration τ_0 of a single collision, *i.e.*

$$\langle \Gamma(t)\Gamma(t') \rangle = 0, \text{for } |t - t'| \geq \tau_0.$$

This assumption is reasonable because the collisions of different molecules of the fluid with the small particle are approximately independent. Considering that usually $\tau_0 \ll 1/\gamma$, we can take the limit $\tau_0 \to 0$ as a reasonable approximation,

giving

$$\langle \Gamma(t)\Gamma(t')\rangle = q\delta(t-t'). \tag{4.14}$$

Say now we want to solve Eq. (4.13) with the initial condition $v(t=0)=v_0$. For this initial condition we have

$$v(t) = v_0 e^{-\gamma t} + \int_0^t e^{-\gamma(t-t')}\Gamma(t')dt'$$

so the correlation function of the velocity reads

$$\langle v(t_1)v(t_2)\rangle = v_0^2 e^{-\gamma(t_1+t_2)} + \int_0^{t_1}\int_0^{t_2} e^{-\gamma(t_1+t_2-t_1'-t_2')} q\delta(t_1'-t_2')dt_1'dt_2'.$$

The double integral is easily calculated as

$$\int_0^{t_1}\int_0^{t_2}\cdots dt_1'dt_2' = q\int_0^{\min(t_1,t_2)} e^{-\gamma(t_1+t_2-2t_1')}dt_1' = \frac{q}{2\gamma}(e^{-\gamma|t_1-t_2|} - e^{-\gamma(t_1+t_2)})$$

that is unchanged upon the interchange of t_1 and t_2. Finally,

$$\langle v(t_1)v(t_2)\rangle = v_0^2 e^{-\gamma(t_1+t_2)} + \frac{q}{2\gamma}(e^{-\gamma|t_1-t_2|} - e^{-\gamma(t_1+t_2)}).$$

We are interested in the thermodynamic limit of the behaviour of the "Brownian" particle in the fluid, so for large t, $\gamma t_1 \gg 1$, $\gamma t_2 \gg 1$

$$\langle v(t_1)v(t_2)\rangle = \frac{q}{2\gamma}e^{-\gamma|t_1-t_2|}$$

that is independent of v_0 and only a function of the time difference $|t_1-t_2|$. This stationary state is characterized by the average energy of the Brownian particle, given by

$$\langle E\rangle = \frac{1}{2}m\langle [v(t)]^2\rangle = \frac{1}{2}m\frac{q}{2\gamma}$$

so from the equipartition law (4.12) the constant q is determined as $q = 2\gamma kT/m$.

For the Brownian motion of a particle is difficult to measure the velocity correlation function, although can be easier to measure the mean-square value of its displacement $x(t)$. Assume that $x(t=0)=x_0$, and $v(t=0)=v_0$ as before, the mean-square value of its displacement at time t is given by

$$\begin{aligned}\langle (x(t)-x_0)^2\rangle &= \left\langle \left[\int_0^t v(t_1)dt_1\right]^2\right\rangle = \left\langle \int_0^t v(t_1)dt_1 \int_0^t v(t_2)dt_2\right\rangle \\ &= \int_0^t\int_0^t \langle v(t_1)v(t_2)\rangle dt_1dt_2.\end{aligned}$$

Based on the previous results we have

$$\langle (x(t) - x_0)^2 \rangle = \left(v_0^2 - \frac{q}{2\gamma} \right) \left(\frac{1 - e^{-\gamma t}}{\gamma} \right)^2 + \frac{q}{\gamma^2} t - \frac{q}{\gamma^3}(1 - e^{-\gamma t}). \tag{4.15}$$

Starting not with the sharp value v_0^2, but with a probability distribution, we already know that the average square of the velocity is given by $\langle v_0^2 \rangle = \frac{q}{2\gamma}$, and the first term on the right-hand side of (4.15) would vanish. For large t ($\gamma t \gg 1$) the leading term in (4.15) is

$$\begin{aligned} \langle (x(t) - x_0)^2 \rangle &= 2Dt, \\ D &= \frac{q}{2\gamma^2} = \frac{kT}{m\gamma} \end{aligned} \tag{4.16}$$

that is the well known result of Einstein [1905] for the diffusion constant D.

These general considerations on diffusive systems lead us to a very straightforward question: considering an ensemble of systems (*i.e.* initial conditions) for which $\Gamma(t)$ is a stochastic quantity, what is the probability to find the particle in the interval of position $(x, x + dx)$? We denote with $P(x, t|x_0, t_0)$ the probability density function for the process, that is, $P(x, t|x_0, t_0)dx$ is the probability that a trajectory will be in the interval $x, x + dx$ at time t when starting from x_0 at time t_0. Determining a differential equation to find this probability can be cumbersome, so we direct the interested reader to [Risken 84] for a detailed derivation. We just state here that a Langevin equation as the (4.13) satisfies the so-called *Fokker-Planck equation*

$$\begin{aligned} \frac{\partial P(x, t|x_0, t_0)}{\partial t} &= L_{FP} P(x, t|x_0, t_0) \\ L_{FP} &= -\frac{\partial}{\partial x}\lambda(x, t) + \frac{\partial^2}{\partial x^2} D(x, t) \end{aligned} \tag{4.17}$$

and the *Kolmogorov equation*

$$\begin{aligned} \frac{\partial P(x, t|x_0, t_0)}{\partial t} &= L_K P(x, t|x_0, t_0) \\ L_K &= \lambda(x_0, t_0)\frac{\partial}{\partial x_0} + D(x_0, t_0)\frac{\partial^2}{\partial x_0^2} \end{aligned} \tag{4.18}$$

whose solution $P(x, t|x_0, t_0)$ is the probability density that we are searching for. Equations (4.17) and (4.18) are also called the *forward* and *backward diffusion equations*, and coefficients λ and D are respectively called the *drift* and *diffusion*

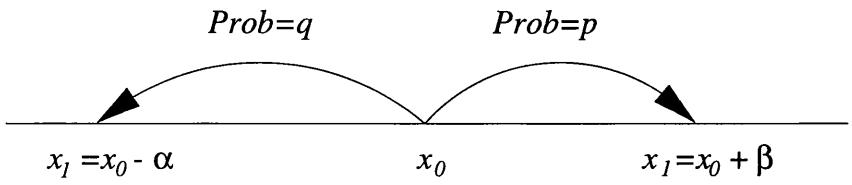

Figure 4.3: Schematic representation of the evolution of the x variable under a random walk process.

coefficients. As (4.17) and (4.18) suggest, they may also depend on position and time. We will sometimes omit the specifications of (x_0, t_0) when their knowledge is not relevant to the discussion.

4.2.2 Random walk models

Let us consider now the simplest stochastic process describing motion of a Brownian particle in one dimension, where the steps are fixed. A simple picture of the dynamics of the particle can be seen in Figure 4.3. The variable x starts from the value x_0, then having the value $x_1 = x_0 + \beta$ with probability p, or the value $x_1 = x_0 - \alpha$ with probability $q = 1 - p$. If the increments/decrements are given at random, with no particular sequence, just with their probabilities defined as above, this model dynamics is called *random walk model* (RWM) in one dimension. In the case the steps are of the same length, the process depicted in Figure 4.3 is a *simple* random walk, sometimes commonly known in probability theory as the "gambler's ruin problem" [Feller 57].

The tent map is a good candidate for the development of a RWM since it is piecewise linear. In the limit of small z_n, we can write an equation of motion for the $|z_n|$, from Eq. (4.3) and (4.6) as

$$|z_{n+1}| = \begin{cases} \frac{1-K}{c}|z_n| & \text{if } 0 \leq x_n < c \\ \frac{1-K}{1-c}|z_n| & \text{if } c \leq x_n \leq 1. \end{cases} \tag{4.19}$$

With the substitutions $\tilde{z}_n = -\log|z_n|$, $\alpha = \log\frac{1-K}{c}$ and $\beta = -\log\frac{1-K}{1-c}$, Eqs.

(4.19) are rewritten as

$$\tilde{z}_{n+1} = \begin{cases} \tilde{z}_n - \alpha & \text{if } 0 \leq x_n < c \\ \tilde{z}_n + \beta & \text{if } c \leq x_n \leq 1. \end{cases} \tag{4.20}$$

Eq. (4.20) represents a RWM in one dimension. For the tent map, x_n has a uniform natural invariant density, so in one iteration $\tilde{z}_n$ can go backward in space a length $-\alpha$ with probability c, and one step forward of $+\beta$ with probability $1-c$. This approach had been already used by [Ott *et al.* 94]. The RWM as in the previous equation is able to explain some peculiarity of the convergence to the synchronised state. Please note that in the new variables the synchronised state is given by $\tilde{z} = +\infty$, and the threshold $A = 10^{-16}$ (the lower bound for two numbers to be equal in double precision) corresponds now to $\tilde{z} = 16 \log 10 = 36.84....$ This threshold has to be compared with the steps in both directions that, for the values $c = 0.307$ and a value of $K = 0.46 \simeq K_{thr}$, are $\alpha \simeq 0.245$, and $\beta \simeq 0.11$. What is now the probability that the variable $\tilde{z}$, evolving according to the dynamical law (4.20), will reach a value $\tilde{z} = -\log A$, say? The probability distribution of a trajectory of the random-walk model is known to be binomial, and the peak of the distribution is given by the mean value [Grimmett & Stirzaker 92]. We have an analytical formula for this binomial distribution for finite N, only in the case the walk is simple, but anyway we can still deal with the mean value of the distribution for finite N. In N iterations of x, we will have, on average, that cN iterations will be in $(0, c)$ and $(1-c)N$ iterations in $(c, 1)$, for N large. The average displacement $\langle \tilde{z}_N - \tilde{z}_0 \rangle$ of $\tilde{z}$ after N iterations will then be given by

$$\langle \tilde{z}_N - \tilde{z}_0 \rangle = -cN\alpha + (1-c)N\beta.$$

With the above definitions of α and β, and choosing $\tilde{z}_0 \simeq 0$ (*i.e.* $|z_0|$ of the order of unity), we have the average displacement, or *drift* per iteration

$$\frac{\langle \tilde{z}_N \rangle}{N} \simeq -\log(1-K) + c \log c + (1-c)\log(1-c) = -\lambda_\perp. \tag{4.21}$$

Let N_p represent the average number of iterations that a trajectory will spend before arriving at $A = 10^{-16}$, the level of the roundoff error; if $\langle \tilde{z}_{N_p} \rangle = -\log A =$

$16 \log 10 \simeq 37$, then $N_p \simeq -37/\lambda_\perp$, for $\lambda_\perp < 0$. The result is shown in Figure 5.3 in Chapter 5, where the numerical position of the peak of the distribution N_p for the logistic map at fully developed chaos is compared to the analytical estimation above. The same result can be obtained remembering that in two coupled dynamical systems with an invariant subset, the distance d_n between the two evolves as $d_n \sim \exp(\lambda_\perp n)$, *on average*. This estimation is made *on average*, so it works supposing that there is only one expansion/contraction rate for the dynamics. In fact, it can easily be numerically proved [Santoboni *et al.* 99b] that it holds for the symmetric tent map ($c = \frac{1}{2}$) as for the fully developed logistic map ($a = 4$), that are conjugate [2]. Both maps have fully developed chaos and all their typical and atypical orbits have the same characteristic exponents (with an exception: see footnote).

The RWM as seen above, makes the assumption that a trajectory z is driven towards (or away from) the invariant subset by a uniform contraction (expansion) rate, quantified by the transverse Lyapunov exponent. Unfortunately, when the dynamics in $\mathcal{S}$ is chaotic, the natural measure is not the only measure present in the system. No indication is given of the contribution of other unstable measures, *i.e.* the delta measures whose supports are given by the unstable periodic orbits embedded in the chaotic attractor in $\mathcal{S}$. The simplification is at the heart of the difference between a pure RWM and the dynamical system shown in (4.20). A RWM has the *Markov property*, that can briefly be explained saying that, conditional upon knowing the value of the process at nth step, its values after the nth step do not depend on its values before the nth step. If p is the probability that the subsequent increment will be $+\beta$, from x_i to x_{i+1}, this will be regardless of the previous history, $x_0, \cdots, x_{i-1}$. The system (4.20) meets this requirement only on average, for a large enough number of iterations. If x_i is very close to an unstable fixed point x_p, we can be fairly sure that x_{i+1} will still be close to x_p, moving away

[2] Actually, despite this conjugacy, the eigenvalue at the zero fixed point is not the same for the two maps ($\log 2$ for the tent map, $\log 4$ for the logistic map), so this fixed point has a different degree of transverse stabilty for the two different maps.

from it as

$$|x_n - x_p| \simeq |x_0 - x_p| e^{\Lambda_p n} \tag{4.22}$$

for small $|x_0 - x_p|$, that is, with an exponential rate where Λ_p is the eigenvalue of the fixed point x_p. In the case (4.20), the increments are given simply according to which side of the unit interval respect to c an iteration lies. For $c = 0.307$, the fixed point is located at $x_p = \frac{1}{2-c} \simeq 0.59$, and its eigenvalue is $\Lambda_p \simeq 0.3667$. According to (4.22), we can estimate that an initial point located at $|x_0 - x_p| = 0.005$ will exit the interval $[c, 1]$ in almost 20 iterations, this resulting, according to Eq. (4.20) in an anomalously deep contraction towards $\mathcal{S}$. An enlighting example is shown in Figure 6.1 in Chapter 6, where 10000 iterations of $|z|$ for this model of coupled skewed tent maps with $c = 0.307$ are shown, compared with the trajectory of the driving x system. Under this condition, the evolution of the skewed tent map cannot in principle be approximated as a random process obeying the Markov property, although they have the same macroscopic statistical quantities, as they both have uniform natural density.

Another basic problem, precluding in our case, any possible development is that the model (4.20) is not simple, as defined above, *i.e.* the steps are not the same in both directions, which is a basic assumption under which all major theorems, in the subject of RWMs, are derived. Ott *et al.* [1994], as well as Ashwin *et al.* [1998], for instance, studied a skew product system where the evolution of the distance from the invariant subset has the form of a simple RWM.

4.2.3 Drift-diffusion approximation

As we stated above, in the most general case there is no exact solution when the RWM is not simple. Despite this misfortune, we can partially overcome the unsolvability of the model and find some macroscopic properties of the process (4.1),(4.20) "simulating" it with the *drift-diffusion approximation* (DDA) [Risken 84]. Our major aim in this study is to find an expression for the probability distribution $P(|z|, n)$ for the variable $|z|$ in view of our numerical problem on the "premature" convergence of trajectories in $\mathcal{S}$.

The main ingredients of the DDA are the *average drift per iterate* $\lambda = \langle \delta\tilde{z} \rangle$, where $\delta\tilde{z}$ is the increment in $\tilde{z}$ in one iterate, and the *diffusion per iterate* D. If the random walk model have uncorrelated steps, we have $D = \frac{1}{2}\langle (\delta\tilde{z} - \langle \delta\tilde{z} \rangle)^2 \rangle$ [Ott *et al.* 94].

The average drift per iterate $\lambda = \langle \delta\tilde{z} \rangle$ for our model is given by $\lambda = -c\alpha + (1-c)\beta$ that, remembering the previous expressions for α and β,

$$\lambda = -c \log \frac{1-K}{c} - (1-c) \log \frac{1-K}{1-c} = -\log(1-K) - \Lambda = -\lambda_\perp \tag{4.23}$$

so that, from (4.4), is exactly the inverse of the TLE, while for the diffusion coefficient,

$$D = \frac{1}{2}[(1-c)(\beta - \lambda)^2 + c(-\alpha - \lambda)^2] = \frac{1}{2}c(1-c)(\alpha + \beta)^2. \tag{4.24}$$

Having estabilished these parameters, the law of evolution of the probability $P(\tilde{z}, n)$ is given by

$$\frac{\partial P(\tilde{z}, n)}{\partial n} = -\lambda \frac{\partial P(\tilde{z}, n)}{\partial \tilde{z}} + D \frac{\partial^2 P(\tilde{z}, n)}{\partial \tilde{z}^2} \tag{4.25}$$

which is called the *drift-diffusion equation.* This equation can easily be recognized as a special form of the Fokker-Planck equation (4.17) discussed at the end of Section 4.2.1, when the drift and diffusion coefficients are constants, independent on time and position. Eq. (4.25) is valid when we work at the thermodynamic limit, that is when $n \to \infty$, so that we can actually consider n as a continuous variable and carry out the derivative at the left-hand side of (4.25). Moreover, its validity holds when the average drift per iterate λ is small compared with the actual steps in both directions, that is

$$|\lambda| \ll \alpha, \beta. \tag{4.26}$$

Considering that for the values previously given for the tent map, α, β are of the order of unity, condition (4.26) yields $|\lambda_\perp| \ll 1$, that is, in other words, that $K \simeq K_{thr}$. Thus, the DDA is valid only close to the blowout bifurcation point. Ott and coworkers [1994] compared the exact probability distribution for a simple

RWM and its diffusion approximation, showing that they agree close to the blowout bifurcation point.

We can now try to solve Eq. (4.25), using as a boundary condition the requirement that all trajectories of $|z|$ for the coupled tent map system (4.1) are bounded between 0 and 1. While at $|z| = 0$ ($\tilde{z} = +\infty$) there is the limit to the synchronised state, $|z| = 1$ ($\tilde{z} = 0$) is the upper bound for the distance between x and y in (4.1). Under the change of coordinates $\tilde{z} = -\log|z|$, the intervals change in $[0, 1] \to [0, \infty]$. For a typical initial condition there will be no flux at $\tilde{z} = 0$, that means

$$\lambda_\perp P(0, n) + D \left.\frac{\partial P(\tilde{z}, n)}{\partial \tilde{z}}\right|_{\tilde{z}=0} = 0. \tag{4.27}$$

It can be quite cumbersome to find an analytical expression for the solution of the drift-diffusion equation (4.25), as well as for the Fokker-Planck equation (4.17) in the general case, and different techniques have been developed, that unfortunately can be applied only in special cases [Risken 84]. Nevertheless, there is an important piece of information we can extract, that is the analytical form of the stationary distribution, solution of the equation $\frac{\partial P(\tilde{z},n)}{\partial n} = 0$. This distribution, that we denote with $P(\tilde{z})$ represents the density probability function towards which all $P(\tilde{z}, n)$ evolve in the thermodynamic limit ($n \to \infty$). We can rewrite Eq. (4.25) as

$$\frac{\partial P(\tilde{z}, n)}{\partial n} = \frac{\partial}{\partial \tilde{z}} \left(\lambda_\perp P(\tilde{z}, n) + D \frac{\partial P(\tilde{z}, n)}{\partial \tilde{z}} \right), \tag{4.28}$$

so the stationary solution is a solution of

$$\lambda_\perp P(\tilde{z}) + D \frac{\partial P(\tilde{z})}{\partial \tilde{z}} = \text{constant}$$

where according to the boundary conditions, the constant is equal to zero. After normalization, given by

$$\int_0^\infty P(\tilde{z}) d\tilde{z} = 1 \tag{4.29}$$

we arrive at the stationary probability distribution

$$P(\tilde{z}) = \eta e^{-\eta \tilde{z}}, \ \eta = \frac{\lambda_\perp}{D}, \tag{4.30}$$

Where the integral (4.29) converges only for $\eta > 0$, that corresponds to $\lambda_\perp > 0$, as is the case we are studying. The qualitative behaviour expressed by this last

equation is meaningful compared to the actual dynamics of the coupled map system (4.1). When $\lambda_\perp > 0$ the probability density (4.30) is an exponentially decreasing function of $\tilde{z}$, meaning that the higher probability to find the trajectory of $\tilde{z}$ is around zero, that in the original variable means z of the order of unity, *i.e.* desynchronisation, with rare excursions with large $\tilde{z}$, as rare as larger is the value of $\lambda_\perp > 0$. The opposite situation, $\lambda_\perp < 0$, results in $P(\tilde{z})$ being an exponentially increasing function of $\tilde{z}$, that means that a trajectory approaches the synchronised state when $\lambda_\perp < 0$, and spends a long time there.

In the original variable $|z|$, we have, according to the law for the transformation of probabilities densities (for example, in [Beck & Schlögl 93]),

$$\widehat{P}(|z|) = P(\tilde{z}(|z|)) \left| \frac{d\tilde{z}(|z|)}{d|z|} \right| = \eta |z|^{-1-\eta} \tag{4.31}$$

that is the stationary probability distribution for $|z|$.

4.3 "Premature" synchronisation

We can now turn our attention back to the problem of the "premature" synchronisation, to see if the statistical issues we developed in the last Sections are of any use or not. We believe that the reason behind this "premature" type of synchronisation has to be found in the roundoff error of the computing machine, that considers two numbers equal if they differ by less than 10^{-16}. Although there are methods to override this problem, as discussed at the beginning of Section 4.2, it is still interesting to consider this behaviour from the statistical point of view, which can help our understanding of which parameter values where $|z|$ gets below 10^{-16}, and also from the dynamical systems point of view (as in Chapter 6), for pointing our attention to what causes the convergence of the trajectories. Considering the skewed tent map, Figure 4.4(top) shows the actual numerical value found for K_0 (open circles), compared with the curve K_{thr} (4.8). We see that the analytical curve, Eq. (4.8), is very close to the numerical one although slight differences can be detected. These differences are highlighted by looking at the behaviour of $|K_{thr}(c) - K_0(c)|$ vs c, in Figure 4.4(middle). The curve $|K_{thr}(c) - K_0(c)|$ is sym-

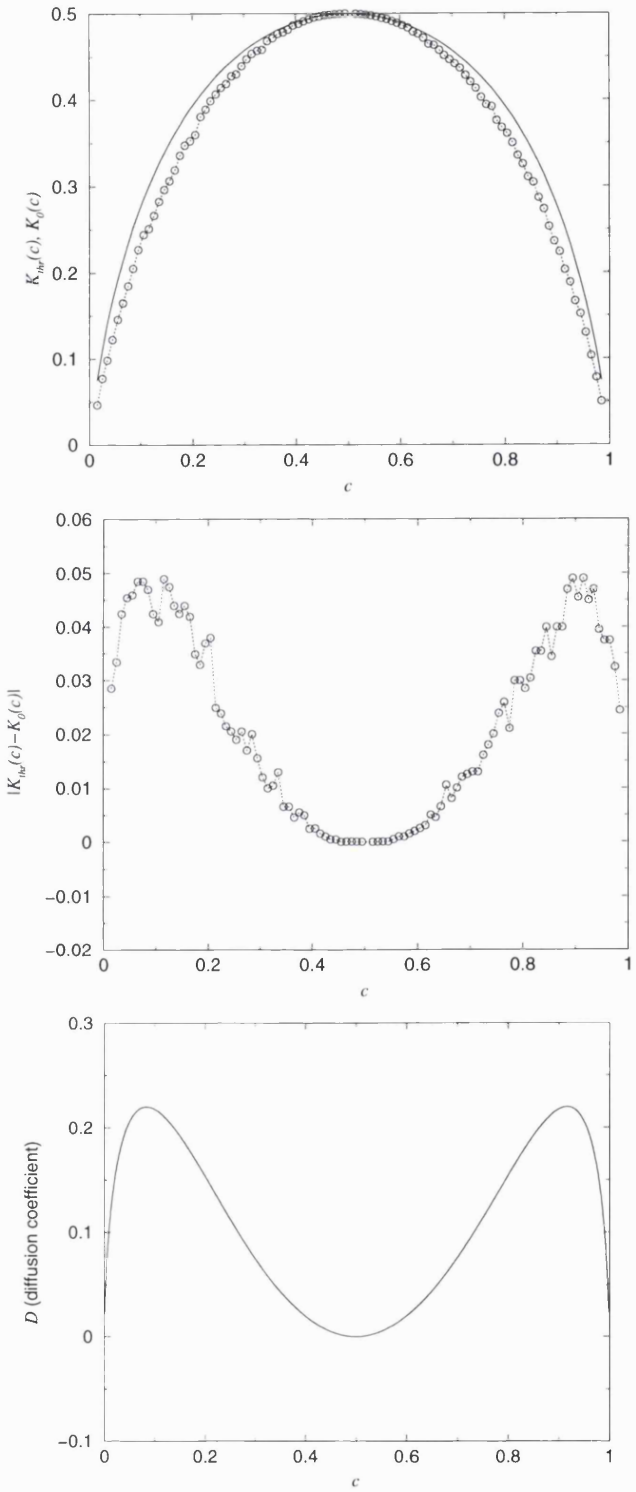

Figure 4.4: Top: plot of $K_{thr}(c)$ and $K_0(c)$ vs c in (0,1). Middle: from the same data as in the left picture, the behaviour of $|K_{thr}(c) - K_0(c)|$ is shown. Bottom: plot of the diffusion coefficient $D(c)$ as a function of c. Note the similarity with the middle picture.

metric around $c = \frac{1}{2}$, where it has a minimum value of zero at $c = \frac{1}{2}$, from which it seems to grow parabolically within the interval $c \simeq [0.1, 0.9]$ beyond which it starts decreasing[3]. There is no evidence of "premature" synchronisation in a neighbourhood of $c = \frac{1}{2}$, while on the contrary, the difference between K_0 and K_{thr} grows quadratically with $|c - \frac{1}{2}|$, before decreasing again. Can we relate the statistical properties of the on-off intermittent time series in the coupled tent map system with the spurious type of synchronisation we observe? Consider the diffusion coefficient D in the drift-diffusion equation. D is constant respect to the position x and the number of iterations n, but it is still a function of the parameters c and K. We have already derived in (4.24) the formula

$$D = \frac{1}{2}[(1-c)(\beta-\lambda)^2 + c(-\alpha-\lambda)^2] = \frac{1}{2}c(1-c)(\alpha+\beta)^2,$$

so that D is defined to be positive. Substituting the expressions for the steps α and β we obtain

$$D = \frac{1}{2}c(1-c)\left(\log\frac{1-K}{c} - \log\frac{1-K}{1-c}\right)^2 = \frac{1}{2}c(1-c)\left(\log\frac{1-c}{c}\right)^2 \qquad (4.32)$$

that is independent of K. Thus the diffusion constant is only a function of the form of the map, characterized by the inversion point c of the skewed tent map. In particular, for $c = 0.307$, we have $D \simeq 0.086$. The diagram in the bottom of Figure 4.4 shows the plot of the function D in (4.32) for c in the unit interval. The similarity with the middle picture, where the behaviour of $|K_{thr}(c) - K_0(c)|$ vs c is shown cannot pass unobserved, leaving us the possibility of conjecturing that the two quantities can be proportionally related. This is intuitively true, considering that the integral

$$\int_0^N \int_{\tilde{z}'}^{\tilde{z}''} \left[\lambda_\perp P(\tilde{z}, n) + D\frac{\partial P(\tilde{z}, n)}{\partial \tilde{z}}\right] dndz$$

represents the flux of trajectories passing through the interval $[\tilde{z}', \tilde{z}'']$ in the integration time $(0, N)$. This quantity is proportional to D by definition, so an heuristic argument for the similarity of the two plots in Figure 4.4.

[3]As in Chapter 2, in all numerical simulations we have taken particular care to avoid the point $c = \frac{1}{2}$ exactly, for the well known numerical problem that causes *numerical* convergence to the zero fixed point by magnification of the roundoff error.

The ultimate goal of this study is to see if we can predict the occurrence of those spurious synchronisation events considering that they are roundoff-induced at a cut-off of $A = 10^{-16}$. The most valuable approach to the problem seems to be by the probability distribution. If we have a probability distribution for $|z|$ (or alternatively, for $\tilde{z} = -\log|z|$) we can use this information to evaluate how remote can be the probability that the distance of two coupled maps can go below the threshold value indicated by A. We will use again the skewed tent map to model the base dynamics f in (4.1), and the expression for the probability distribution is in the variable $\tilde{z}$, linked to the original distance z as $\tilde{z} = -\log|z|$. As we saw previously, this choice will lead to a significant simplification in all the procedures.

With the drift-diffusion equation (4.25) we have found the stationary probability distribution (4.30) for $\tilde{z}$ subjected to the boundary conditions (4.27), that is

$$P(\tilde{z}) = \eta e^{-\eta\tilde{z}}, \ \eta = \frac{\lambda_\perp}{D},$$

where we remind ourselves that the normalisation factor η exists only for $\eta > 0$, from the convergence of the integral in (4.29). In this representation, $|z| = A = 10^{-16}$ corresponds to $\tilde{z} = \tilde{z}_A = 16\log 10 \simeq 37$. As stated at the beginning of the Chapter, for the precision used, we found non-trivial "basins" of attraction in the interval $[K_0, K_1] \simeq [0.443, 0.453]$, where every initial condition has been iterated for at most 10^6 iterations to check its convergence below A. This suggests that we can search for those K values where the probability $P(\tilde{z}_A)$ is sufficiently large that at least one initial condition will fall in the region $\tilde{z} > \tilde{z}_A$ (that is $|z| < A$) in 10^4 initial conditions. $P(\tilde{z}_A) = 10^{-4}$, say, indicates that at least one initial condition in 10000 will fall in $\tilde{z} > \tilde{z}_A$. From the formula (4.30) we have,

$$-\log_{10} P(\tilde{z}_A) = \mathcal{F}(K) = -\frac{1}{\log 10}\left[\log\frac{\lambda_\perp}{D} + \frac{\lambda_\perp}{D}\tilde{z}_A\right]. \tag{4.33}$$

In this formula, the transverse Lyapunov exponent $\lambda_\perp$ is the only quantity in the right hand side of (4.33) that actually depends on K, as in (4.4). Clearly, the expression (4.33) holds only for $\lambda_\perp > 0$.

We plot in Figure 4.5 the curve $\mathcal{F}(K)$ representing the right hand side of (4.33), for various values of K in the interval [0.440,0.460], note that $K_{thr} \simeq$

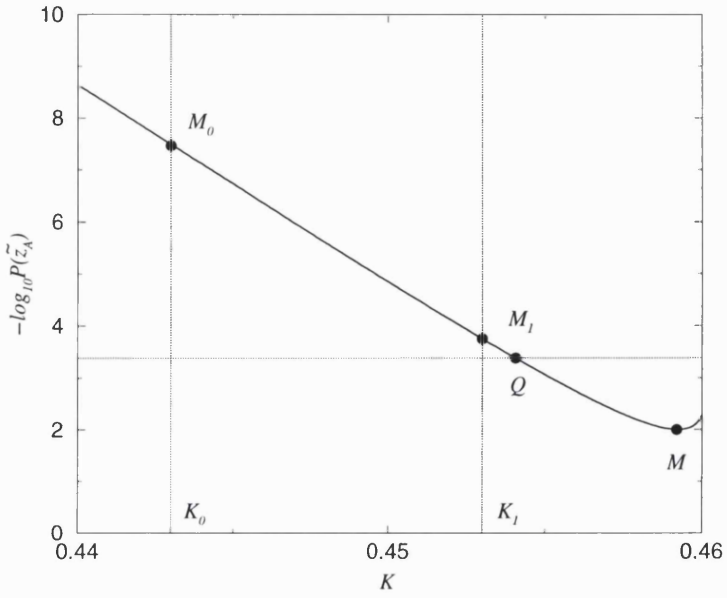

Figure 4.5: The thick solid curve represents the behaviour of $\mathcal{F}(K)$, that is the right-hand side of Eq. (4.33) for various values of $K < K_{thr} (\simeq 0.4602)$.

0.4602.... Some representative points are shown on the curve $\mathcal{F}(K)$. The coupling parameter is on the horizontal axis, and in particular points K_0 and K_1 are marked, representing the edges of the interval where non-trivial "basins" are numerically evaluated. On the y-axis, M_0 and M_1 correspond on the curve to K_0 and K_1 respectively, having coordinates $M_0 \equiv (K_0, \simeq 7.45)$ and $M_1 \equiv (K_1, \simeq 3.69)$. In the case of K_0 for instance, the ordinate 7.45 indicates that to see at least one initial condition converging in the region $|z| < A$ is an event with probability $-\log_{10} P = 7.45$, thus it should take approximately 2.8×10^7 initial conditions to see all the phase space visiting the region $|z| < A$. We remind that the a grid of 49×49=2401 initial conditions are used in the numerical experiments described at the beginning of the chapter. The horizontal line $-\log P(\tilde{z}_A) = \log_{10} 2401$ intersects $\mathcal{F}(K)$ in $Q \equiv (\simeq 0.454, \log_{10} 2401)$. The abscissa of this point gives us the value of K at which (theoretically, according to the DDA at the limit $t \to \infty$) we should expect all initial conditions in the unit square to converge in $|z| < A$. This point is clearly seen to fall outside the interval $[K_0, K_1]$ but very close to M_1, suggesting that even in the strong limitation of using the stationary probability distribution, the DDA can be a useful tool to investigate the dynamic.

An additional matter of curiosity (whether meaningful, considered the limitation cited above) comes from the fact that the curve $\mathcal{F}(K)$ shown in Figure 4.5 has a minimum, a point denoted with M, whose abscissa K_M is then evaluated from $d\mathcal{F}/dK = 0$, thus giving

$$K_M = 1 - e^{-(\Lambda + \frac{D}{\tilde{z}_A})} \simeq 0.4592.$$

We note that $\tilde{z}_A \simeq 37$, and $D \simeq 0.086$, $D/\tilde{z}_A \simeq 2 \times 10^{-3}$ is a small number, then K_M is just slightly below K_{thr}, from the expression given in (4.5). An interesting issue is whether the formula (4.33) can help us in deriving how a different precision, number of iterations, and grid size may modify the numerical results, as previously discussed in Section 4.1.3. The precision used is represented in the formula (4.33) by $\tilde{z}_A = -\log A$, while a different grid size will shift the point Q in the curve in Figure 4.5. No mention is instead present of the number of iterations used in the in the formula (4.33). This is the major limitation of the approximation we used, because the formula (4.33) is derived from the stationary probability distribution (4.30), while we are seeking to describe a finite-time effect. A more complete approach will be of solving the full drift-diffusion equation (4.25), but although an explicit solution can be found applying the Laplace transformation of all terms in it, no inverse transform exist.

As a concluding remark to this chapter, we remember that in the diffusion approximation the diffusion coefficient D chracterizes the decrease, in increasing time, of the dispersion of finite time Lyapunov exponent, sometimes called *local Lyapunov exponents* (LLEs). If after n iterations the TLE $\lambda_\perp$ has a distribution $F(\lambda_\perp, n)$ with

$$\langle (\delta\lambda_\perp)^2 \rangle^{1/2} = \left[\int (\lambda_\perp - \langle \lambda_\perp \rangle)^2 F(\lambda_\perp, n) d\lambda_\perp \right]^{\frac{1}{2}}$$

the dispersion will approach zero as $1/\sqrt{n}$,

$$\langle (\delta\lambda_\perp)^2 \rangle^{1/2} \simeq \sqrt{\frac{2D}{n}},$$

although we do not have a precise idea of what its distribution will look like during the transient before convergence to the mean value. This problem is actually of

great interest in dynamical systems theory, since it provides a bridge between the nature of the phase space of a dynamical system and its statistical properties. As we mentioned at the beginning of Section 4.2, for hyperbolic sets it can be proved that the central limit theorem holds for a number of averaged quantities like Lyapunov exponents, so that the distribution of LLEs is Gaussian [Ott 93].

In presence of a certain dissipation in the direction transverse to $\mathcal{S}$ a trajectory of $|z_n|$ (or an equivalent measure of the distance from $\mathcal{S}$) experiences attraction towards the invariant subset, and this can be alternatively viewed (and even characterized) via the distribution of the LLEs. More precisely, close to the blowout bifurcation point, for small $\lambda_\perp > 0$, the distribution of LLEs can have a significant negative tail, so $\lambda_\perp$ can be negative if averaged on a short time interval, while its mean value is positive. Consider, for example, the case of the *noise-induced synchronisation* pointed out by Maritan and Banavar [1994a]. In their work, two continuous or discrete chaotic systems coupled with an identical random noise can synchronise above a certain noise amplitude. This finding generated some discussion [Pikovski 94, Maritan & Banavar 94b], and finally in [Herzel & Freund 95] was shown how the non-zero value of the mean of the noise could, above a certain noise amplitude, modify the distribution of the LLEs, generating a significant tail on the negative side.

In Figure 4.6 we show two series of four plots of the distribution of the LLEs for two different number of iterations (left column $n = 50$, right column $n = 1000$), and four values of K (given in Figure) across the blowout bifurcation for the skewed tent map. We can see how the distribution narrows towards a delta function peaked at the mean value in increasing n, but also that for $K = 0.450$ there is a significant negative tail, exactly for a value of K that lies in the interval $[K_0, K_1]$.

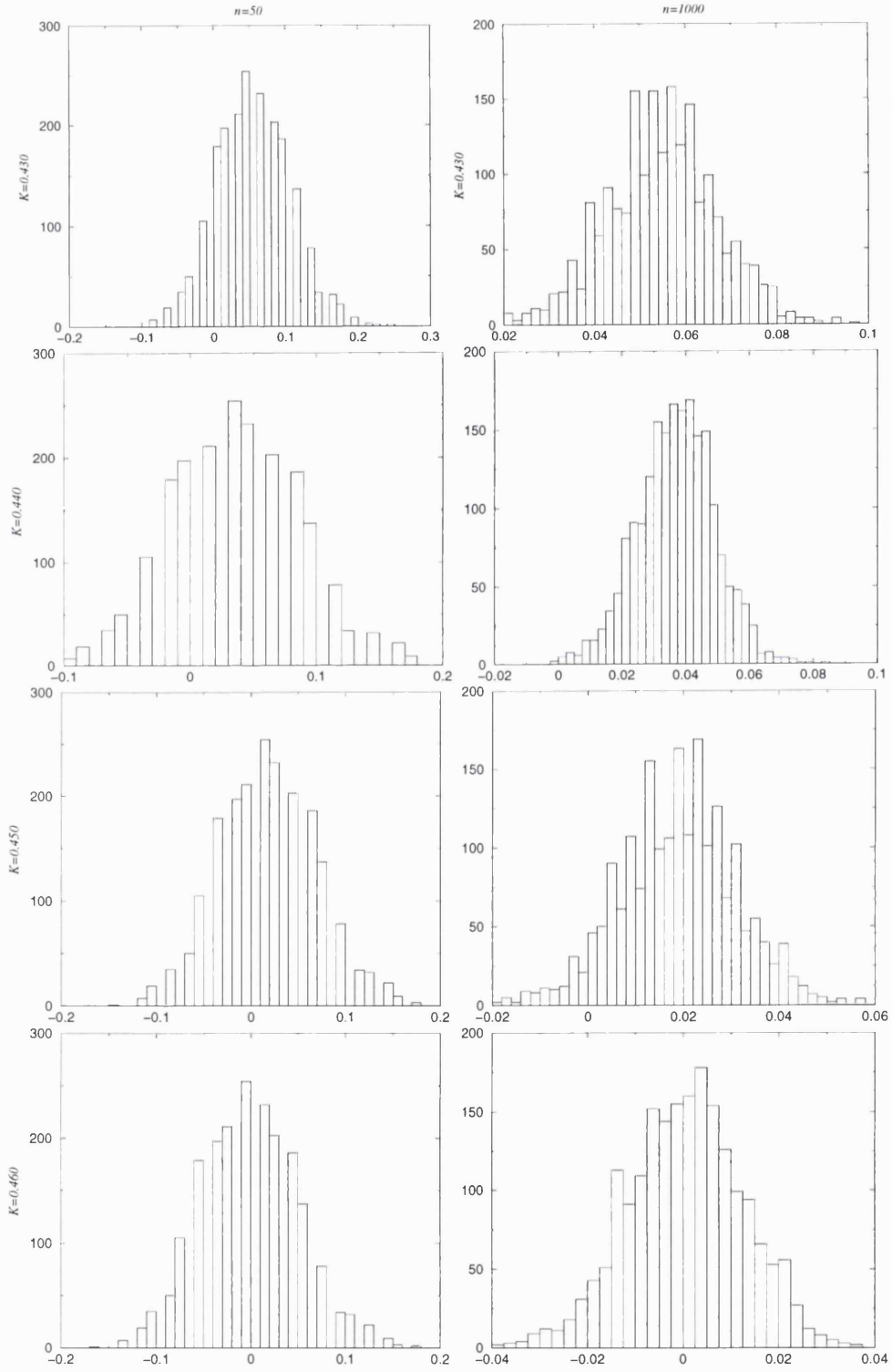

Figure 4.6: Plots of the distribution of the finite-time Lyapunov exponents for the skewed tent map system. Two plots are made for each value of K for the four rows, and four plots for each value of n, the number of iterations on which the average is produced.

Chapter 5

Transient phenomena

A dissipative dynamical system reaches a stable solution only after a certain transient, that may intuitively depend on the structure of its phase space (*i.e.* how many possible attractors are in it), its initial starting conditions, and the stability properties of the final stable attractor (*i.e.* the rate of dissipation). Stationary solutions attract nearby trajectories through their stable manifolds, and the rate which a trajectory approaches a stationary solution is given by the leading eigenvalue of the stable subspace. The subject of this chapter is to identify how transient phenomena behave when the stable solution is the synchronised state, *i.e.* the invariant subset described in the introductory chapters. In the subject of chaotic dynamics, there are some intrinsic difficulties in characterizing the properties of stationary solutions. Several indicators, such as surfaces of section, characteristic exponents and dimensions can characterize solutions of nonlinear equations of motion that, in the case of chaotic systems, can be particularly uneasy to handle due to their sensitivity to initial conditions. Nevertheless, this is only about stationary solutions, in other words at thermodynamic equilibrium. What about the transient process that leads to a stationary solution, that is, not at equilibrium? Much less in this case is known, and only qualitative observations have been made, for example, that stable periodic solutions and fixed points can be reached after chaotic transients, originated after transverse homoclinic intersections (so the existence of a Smale horseshoe) in the case of the escape from a potential well [Thompson 89]

with basins of escaping and non-escaping zones separated by fractal boundaries, or similarly, in case there is a solution whose basin has measure one, when a Cantor set (that never escapes, as in the example of Section 3.1 in [Ott 93]) is present in the phase space, with chaotic dynamics on it.

We now turn to the case of synchronised states. If the synchronised state $\mathcal{S}$ of coupled dynamical systems is stable, it follows that there must be a neighbourhood of $\mathcal{S}$ whose initial conditions, up to a set of zero measure, are attracted to it. We will investigate in this Chapter whether the transient motion, originated by initial conditions in this neighbourhood, has typical features, and whether or not scaling laws exist for the length of their transient wandering before convergence. We will first see an introductory case of the properties of chaotic transients after a boundary crises [Grebogi *et al.* 83b], and turn our attention afterwards to the motion of coupled dynamical systems with an invariant subset. We use coupled 1-dimensional maps on the unit interval because in some cases we can derive some conditions analytically (as we already did at the beginning of the previous Chapter). Then, to illustrate some observed characteristics for a higher dimensional case we investigate a system consisting of two separate Duffing oscillators with identical parameters which are coupled through a unidirectional linear relationship. Our interest is focused on the behaviour of the system when it is in a chaotic state with values of the coupling parameter which lead to synchronisation of the two systems and, in particular, in the time of transient decay onto the synchronised state. Thus, we shall discuss a very straightforward problem: if we have a system with a stable synchronised state, how long does a trajectory take to converge onto it? Different initial conditions may converge at different rates, thus it may be important to assess not only the rate of convergence but also any spatial variation. It is also important to examine how these two aspects alter as we vary system parameters. A particular system but viewed at different parameters may also have different degrees of stability for the invariant subset, influencing the convergence of the trajectory towards the synchronised state.

Our study will discuss if there is a particular distribution of the transient time to synchronisation when the degree of stability varies (*i.e.* as we change a coupling

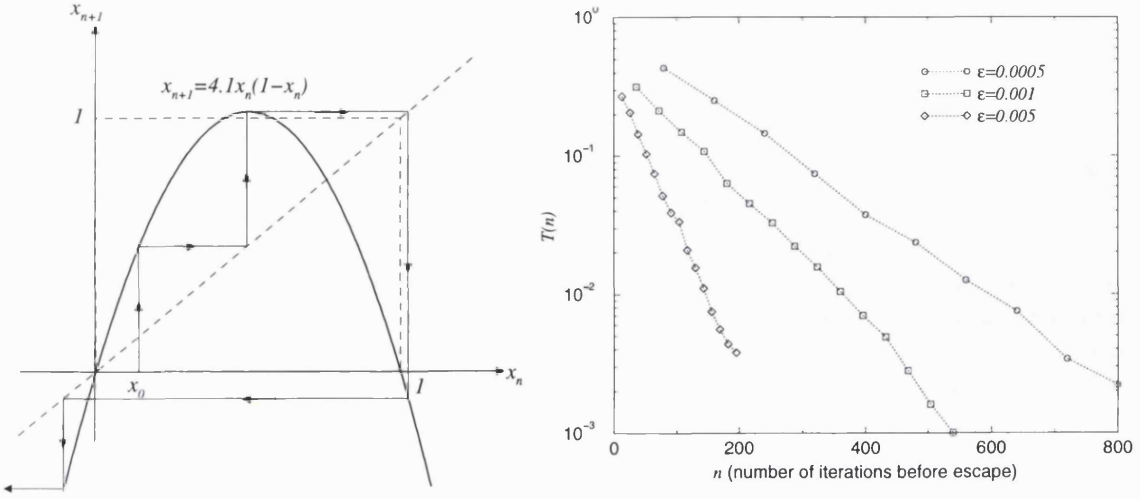

Figure 5.1: Left picture: schematic representation of the action of the map $x_{n+1} = ax_n(1 - x_n)$, for $a = 4.1$. The dashed lines mark the unit square and the the fixed points line. Right picture: three plots of the distributions $T(n)$ for three values of ε given. The logarithmic scale shows the exponentially decreasing behaviour.

parameter, the maximum transverse Lyapunov exponent may become smaller in magnitude, weakening the stability) and, for fixed parameters, in the space of initial conditions of the driving system.

5.1 Chaotic transients from a boundary crises

When a stable chaotic attractor collides at the parameter value, $p = p_c$ say, with an unstable periodic orbit, then a *boundary crises* is said have occurred [Grebogi *et al.* 83b, Ott 93]. For $p > p_c$, the chaotic attractor is replaced by chaotic transients of length τ, with the scaling of $\langle\tau\rangle$ found to behave as $\langle\tau\rangle \propto (p - p_c)^{-\gamma}$ close to, but just beyond the bifurcation point, where γ is the scaling exponent. Consider the following example, where the parameter a of a logistic map is set slightly larger than 4. The left picture of Figure 5.1 shows the dynamic of this map. The iterations of the map $x_{n+1} = ax_n(1 - x_n)$ go out of the unit square for every typical initial condition, because sooner or later they enter the interval centered around $\frac{1}{2}$ where the maximum is above 1. So a trajectory starting from x_0 will experience a certain transient before escaping, that will obviously depend

upon the value of the parameter a, as well as on the initial point taken in [0,1]. The larger the value of a, the faster the escape will be on average, since the interval that leads to escape after one iteration will be larger, but the choice of initial condition makes a difference as well. Consider $a = 4 + \varepsilon$. Numerical investigations show that the distribution $T(n)$ of the escape time of a set of initial conditions, uniformly distributed in the unit interval, is exponentially decreasing, of the form $T(n) \propto e^{-n/\langle n \rangle}$, where the characteristic transient lifetime $\langle n \rangle$ has been shown to vary as $\langle n \rangle \propto \varepsilon^{-\gamma}$, with $\gamma = \frac{1}{2}$ [Ott 93]. The exponential distributions for three values of ε are shown in the right picture of Figure 5.1.

As we said at the beginning of this section, a boundary crises takes place when a chaotic attractor collides with an unstable periodic orbit that was in the basin boundary before the crises. For different low-dimensional systems undergoing a boundary crises the sudden dynamical transition is apparently due to a single unstable periodic orbit, and the relationship $\langle n \rangle \propto \varepsilon^{-\gamma}$, with $\gamma \simeq \frac{1}{2}$ can be heuristically derived assuming a quadratic tangency at the critical point $\varepsilon = 0$ [Grebogi *et al.* 87b].

5.2 Coupled Maps

As we described in the previous chapter, the advantage of using coupled maps relies on the fact that we can sometimes have analytical information on the stability of invariant subsets. Consider the system of coupled maps (4.1) we already investigated in the previous chapter, namely

$$\begin{cases} x_{n+1} = f(x_n) \\ y_{n+1} = f(y_n) - K[f(y_n) - f(x_n)], \end{cases}$$

where the x system drives the y system with no feedback from it. An analytic expression of the threshold of stability of the invariant subset $\mathcal{S}$ (*i.e.* the synchronised state) in (4.1) is given by $K_{thr} = 1 - e^{-\Lambda}$, relation (4.5). We have already discussed how the numerically evaluated threshold of synchronisation does not exactly coincide with the semi-analytical estimation from (4.5), so now we concentrate here on the study of the transient time a typical trajectory spends before

converging onto $\mathcal{S}$. We remind ourselves that for the coupled maps problem, the convergence onto $\mathcal{S}$ is numerically evaluated with the requirement that x_n and y_n will be equal for the computing machine, so below the threshold level of 10^{-16}, operating in double precision. We already know that from this consideration there is the possibility of premature numerical convergence due to roundoff errors, so we will consider only cases for which $\lambda_\perp < 0$, so when $\mathcal{S}$ is a stable subset in the real meaning of the term.

We perform some numerical experiments on the synchronisation of two coupled maps, the logistic map $f(x) = ax(1-x)$, for $a = 3.9$ (not at fully developed chaos), and the skewed tent map (4.6) for $c = 0.307$, coupled as in (4.1). Relations (4.4) and (4.5) derived in Section 4.1 holds for both cases. To investigate the distribution of transient times to synchronisation in this coupled map system (4.1), we introduce the simplification of taking a section for a fixed y_0 and checking the transient distribution times of 10000 initial conditions x_0 uniformly distributed in [0,1]. This is a reasonable approach to take since the dynamics transverse to $\mathcal{S}$ is dependent mainly upon the dynamics of the driving system. We examine the changes in the form of the distribution $T(n)$ of transients to convergence towards $\mathcal{S}$ when the value of K is altered. All points used form the distribution of number of iterations that is actually a measure of the probability $T(n, x_0)$ for the initial point x_0 to converge in n iterations. Assuming we have chosen only typical points in the phase space of both maps, we can drop the spatial dependence and simply write $T(n)$. Figure 5.2 shows the numerical evaluation of $T(n)$ for the two maps for different values of K. Looking at the top picture for the logistic map we remind ourselves that the threshold of stability of synchronisation is located at $K_{thr} \simeq 0.3911$, whereas for the tent map it is located at $K_{thr} \simeq 0.4602$. From an observation of both sets of pictures it can be easily seen that the evolution of $T(n)$ is qualitatively the same for both maps. While for $K \gtrsim K_{thr}$, $T(n)$ shows an exponentially decaying tail (as for the case of the boundary crises), when K is increased consistently this distribution gets closer to a binomial (Gaussian) one. In all graphs, an arrow marks the position of N_p, a quantity representing the average number of iterations needed to converge onto $\mathcal{S}$, under the assumption that

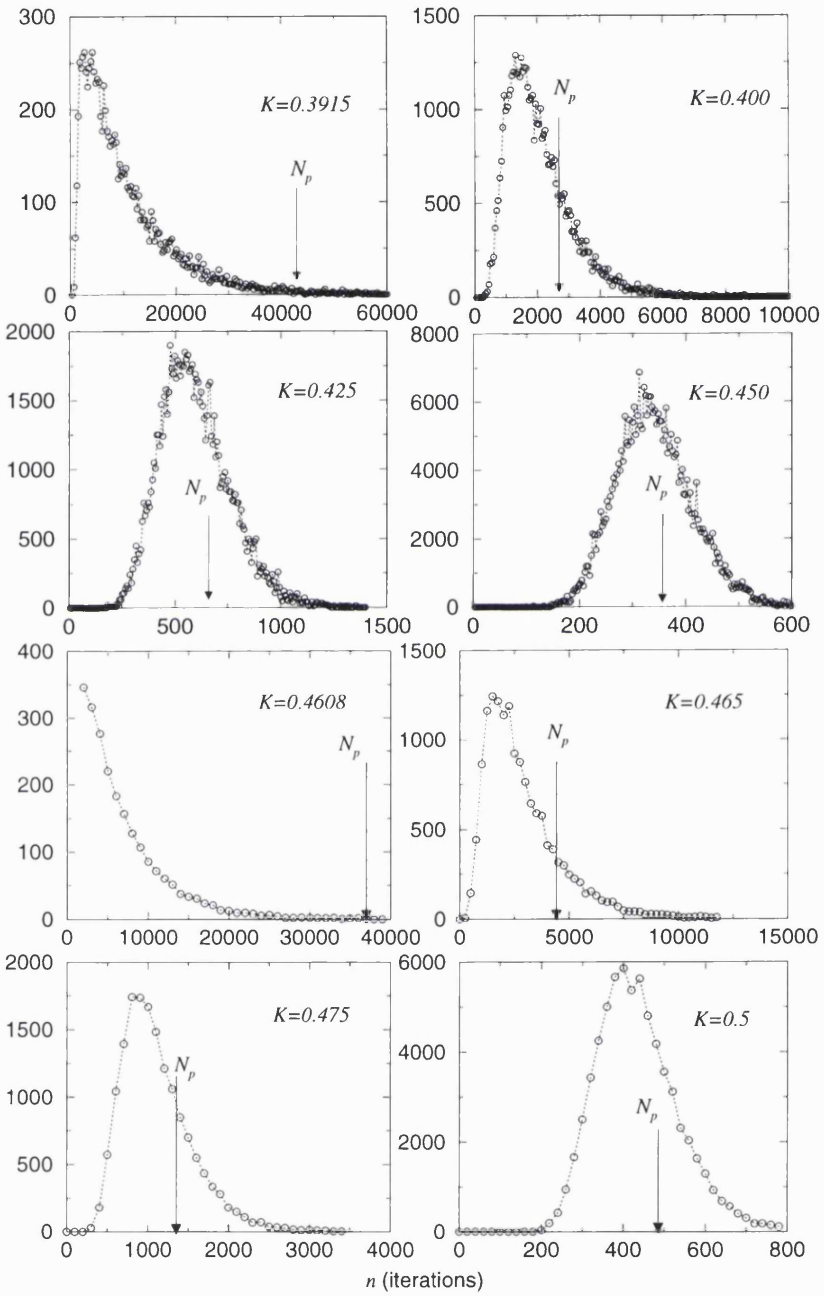

Figure 5.2: Two series of four plots for the the distribution $T(n)$ of the number of initial conditions converging to synchronisation versus n for two coupled logistic maps with $a = 3.9$ (top), and for the skewed tent map with $c = 0.307$ (bottom). Both series are composed of four plots for each map in which the value of K is varied. Note that the y axes are different.

logistic map			skewed tent map		
K	$\lambda_\perp$	N_p	K	$\lambda_\perp$	N_p
0.3915	-8.5×10^{-4}	43058	0.4608	-9.89×10^{-4}	37251
0.400	-0.014923	2469	0.465	-8.809×10^{-3}	4184
0.425	-0.057483	641	0.475	-0.027678	1331
0.450	-0.101935	361	0.500	-0.076468	482

Table 5.1: Transverse Lyapunov exponents $\lambda_\perp$ and number of iterations N_p for the cases shown in Figure 5.2.

there is only one convergence rate, given by the TLE $\lambda_\perp$. We will see in Section 5.3.1 how this quantity is evaluated and its meaning. The numerical detection of the convergence onto $\mathcal{S}$ is in fact given by the first instant that a trajectory of $|z| = |x - y|$ passes below the threshold of 10^{-16}. Considering a slightly different threshold does not significantly affect the shape of the distribution shown in Figure (5.2).

5.3 The first passage time problem (FPT)

When considering the temporal evolution of a trajectory, it is often useful to determine what is the probability that the trajectory will leave a certain domain of the phase space in a certain time interval. This problem is known as the *first passage time* problem (FPT) and it has been widely studied in the past in the context of stochastic processes. For a perspective in the literature, in the discussion to come we sometimes referred to [Feller 57, Ricciardi 77]. In the previous Chapter we studied the characterisation of the macroscopic properties of a deterministic but chaotic process with techniques originally developed for the realm of stochastic processes. Although we are well aware of the differences, they proved to be useful, enabling us to find an approximation for the probability density function $P(n)$ for the trajectory $z = y - x$ in (4.1). In the next Sections we will discuss, using almost the same steps as in the previous chapter, how to derive approximations for

the probability density function $T(n)$ for the first passage time of the trajectory z below the point $A = 10^{-16}$.

5.3.1 FPT in random walk models

In Chapter 4 we developed our first steps into the statistical description of the intermittent time series, using a random walk model (RWM) for the linearized equations (4.3), when the base dynamics is given by a piecewise linear map on the unit interval, *e.g.* the skewed tent map (4.6). As we previously stated, analytical treatment of the RWM is possible when the walk is simple, that is, when the steps in both directions are the same. In Eq. (4.20) this corresponds to $\alpha = \beta$, condition that is fulfilled for $c = \frac{1}{2}$, that is, using a symmetric tent map for f. In this case, also probabilities c and $1 - c$ are obviously the same. We now try to abstract the RWM from the deterministic problem of the convergence towards $\mathcal{S}$ in (4.1), considering the *simple* RWM

$$S_{n+1} = S_0 + \sum_{i=1}^{n} X_i \tag{5.1}$$

where $X_i = +1$ with probability p and $X_i = -1$ with probability $q = 1-p$. If $p \neq q$ the RWM has a certain bias, *i.e.* it posesses a drift $\lambda \neq 0$, and it will therefore take, on average, a certain direction. To identify this discussion on RWM with the one presented in (4.20), consider the variable S_n as $\tilde{z}_n$, and the steps α and β both equal to 1. As already said in the previous chapter, the probability distribution P of the variable S_n (on a finite time n) is binomial, and the probability that the first n steps of the walk follow a given path is proportional to $p^r q^{n-r}$, where r is the number of steps to the right (*i.e.* $X_i = +1$) and $n - r$ the remaining on the left. The coefficient of proportionality is given by the number of all possible paths that starting from S_0 will end in S, say, with that particular number of steps above, yielding

$$P(S_n = S) = \binom{n}{r} p^r q^{n-r}. \tag{5.2}$$

or, with $S_0 - S = 2r - n$,

$$P(S_n = S) = \binom{n}{\frac{1}{2}(n + S_0 - S)} p^{\frac{1}{2}(n+S_0-S)} q^{\frac{1}{2}(n-S_0+S)}. \tag{5.3}$$

The probability distribution above gives the probability that a RWM starting from S_0 reaches the point S after n iterations [Grimmett & Stirzaker 92].

It may seem intuitive that the probability distribution for the first passage time (FPT) $T(S,n)$, that is, the smallest n for which $S_n = S$, is proportional to (5.3). We say it may seem, because if most of the initial conditions will more than likely be, after n iterations, at a position that is the peak of the distribution P, then most of them will converge in the same time, thus giving a corresponding peak. In fact, it is possible to prove the *hitting time theorem* [Grimmett & Stirzaker 92] stating that the probability $T(S,n)$ that a RWM hits the point S for the first time at the nth step, having started from zero, satisfies

$$T(S,n) = \frac{|S|}{n} P(S_n = S). \tag{5.4}$$

Ashwin *et al.* [1998] make use of this theorem to find the distribution of laminar phases for on-off intermittency, in view of the fact that they consider a simple RWM to model the dynamics. Theorem (5.4) is useful, but only in cases where we can model the dynamics as a simple RWM. For example, the symmetric tent map and the conjugate logistic map (at fully developed chaos) display a binomial-like distribution for $T(S,n)$, with small dispersion around the mean, this assuring that the quantity P/n in (5.4) does not differ much from a binomial. The peak of the distribution $P(S_n = S)$ is centred on the mean value, defined by $\langle \delta S \rangle = \langle r \rangle - \langle n - r \rangle$ that is, the average number of steps on the right minus the average number of steps on the left. The mean number $\langle r \rangle$ is, by definition,

$$\langle r \rangle = \sum_{r=0}^{n} \binom{n}{r} p^r q^{n-r} r \tag{5.5}$$

where there is an easy trick to evaluate the sum. If we consider that $rp^r = p\frac{\partial}{\partial p}(p^r)$, the sum in (5.5) gives

$$\begin{aligned} \textstyle\sum_{r=0}^{n} \binom{n}{r} \left[p\frac{\partial}{\partial p}(p^r) \right] q^{n-r} &= p\frac{\partial}{\partial p} \left[\textstyle\sum_{r=0}^{n} \binom{n}{r} p^r q^{n-r} \right] \\ &= p\frac{\partial}{\partial p}(p+q)^n = pn(p+q)^{n-1} = pn. \end{aligned}$$

The result was quite intuitive, and similarly, we have that $\langle n - r \rangle = qn$, thus giving $\langle \delta S \rangle = n(p-q)$. This expression is the same found in the previous Chapter

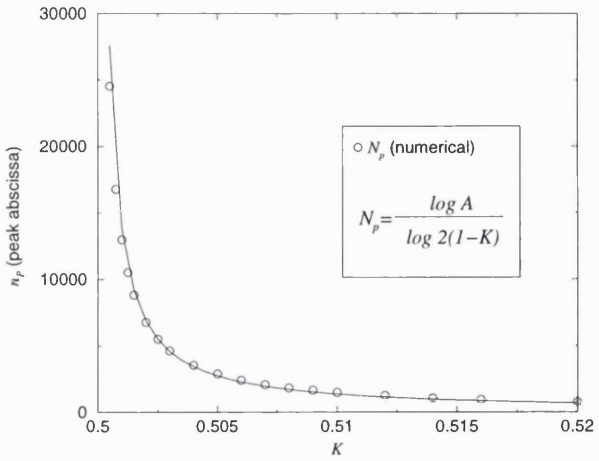

Figure 5.3: Position of the abscissa n_p of the peak of the distribution of synchronisation times for the coupled logistic maps at fully developed chaos ($a = 4$). The open circles represent the numerical points while the solid line represents the analytically derived function.

when we introduced the average drift per iterate, considering that $\alpha = \beta = 1$ and $S = \tilde{z}_A$. So, if N_p represents the position of the peak of the distribution T, *i.e.* the average number of iterations that a trajectory will spend before arriving at $A = 10^{-16}$, we have $N_p = -\log A/\lambda_\perp$, for $\lambda_\perp < 0$. This relation is easily numerically verified to hold, as Figure 5.3 shows, where the numerical position of the peak of the distribution N_p for the logistic map at fully developed chaos is compared to the analytic estimation. As in the previous chapter, we see that the use of a RWM gives a good qualitative description for simple models, *i.e.* when the steps in both direction are the same. The natural extension we can take in our discussion is now to consider a DDA to simulate a less specific dynamical case.

5.3.2 FPT in diffusion processes

We have dealt in the previous Chapter with the question of finding the statistical properties of a stochastic signal $x(t)$, considering that its probability density function obeys the partial differential equation (4.25). The properties already derived in the previous Chapter can help us in tackling a seemingly different problem, the first passage time problem that, in a way, it can be seen as switching from the description of $x(t)$ to the description of $t(x)$. Considering the continuous time and

real valued trajectory $x(t)$, representing the trajectory of the stochastic process in question, we ask for the probability distribution of the time t at which $x(t)$ enters a state S, say, for the first time. If $x(t)$ is a random process, clearly the FPT is a random variable, in the interval $[t_0, \infty)$, where $x(t_0) = x_0$. For this problem, S can be seen as an absorbing barrier for the process.

First, we adjust the notation for the discussion. We will denote $x(t)$ the trajectory of the random process, as a continuous time variable, and $P(x, t|x_0, t_0)$ its probability density function, to be interpreted such that $P(x, t|x_0, t_0)dx$ represents the probability that the trajectory will be in the interval $x, x + dx$ at time t, after having started from x_0 at time t_0. Whenever we will use the shortened version $P(x, t|x_0)$, it is meant that $t_0 = 0$. We similarly denote with $T(x, t|x_0)$ the probability density function for the FPT, *i.e.* $T(x, t|x_0)dt$ gives the probability that in the time interval $t, t + dt$, $x(t)$ attains the threshold S for the first time, given that $x(0) = x_0$. Our task is to find a probability density function for the FPT, and this will certainly involve considerations on $P(x, t|x_0)$, partly given previously. Ricciardi [1977] discussed a very elegant approach on the problem, but we will instead follow the lines of the derivation of Siegert [1951] of a functional equation for $T(x, t|x_0)$.

Let the starting point for the process $x_0 < S$ be below the threshold, and denote with x an arbitrary state above S. Every sample path that at time t lies in the interval $x, x + dx$ must necessarily have crossed S for the first time at some instant $\tau < t$. We can express this condition mathematically as

$$P(x, t|x_0) = \int_0^t T(S, \tau|x_0) P(x, t - \tau|S) d\tau. \tag{5.6}$$

This integral equation is known to have been first derived by E. Schrödinger in 1915, and it is not the only approach to derive a functional equation for $T(x, t|x_0)$, but has the advantage of not requiring any explicit formula for $P(x, t|x_0)$ to derive a corresponding expression for $T(x, t|x_0)$. Moreover, its application has already proved to be fruitful. Chandrasekhar [1943], for example, estimated the rate of escape of stars from galaxy clusters by determining the probability that a star with given initial velocity will reach a chosen velocity for the first time in $t, t + dt$,

obtaining this probability from a modified form of (5.6). As customary in solving integro-differential equations, we will use the Laplace transforms to carry on the derivation. The Laplace transform of a function $f(x)$ in the variable s is given by

$$\mathcal{L}[f(x);s] = \int_0^\infty e^{-sx} f(x) dx,$$

and its inverse transform as

$$\mathcal{L}^{-1}[F(s);x] = \frac{1}{2\pi i} \int_{\gamma-i\infty}^{\gamma+i\infty} F(s) e^{sx} ds,$$

where $F(s)$ is an analytic function of order $\mathcal{O}(s^{-k})$ with $k > 1$ and γ is a real constant that exceeds the real part of all singularities of $F(s)$. A survey of the principal Laplace transforms can be found in [Gradshteyn & Ryzhik 94], but we cite here only two main theorems: The *convolution theorem*, which states that the Laplace transform $\mathcal{L}$ in the variable s of a convolution product $f * g(x)$, defined as

$$f * g(x) = \int_0^x f(x-\xi) g(\xi) d\xi,$$

is given by

$$\mathcal{L}[f * g(x); s] = \mathcal{L}[f; s]\mathcal{L}[g; s],$$

and the transform of a derivative, stating that

$$\mathcal{L}[df/dt; s] = s\mathcal{L}[f(t); s] - f(0).$$

Eq. (5.6) is a convolution product of the functions T and P, so applying this theorem we obtain the relation

$$T_s(S|x_0) = \frac{P_s(x|x_0)}{P_s(x|S)} \tag{5.7}$$

where we have denoted with T_s and P_s respectively for the Laplace transforms of T and P with respect to time. Therefore, if the Laplace transform of the probability density function is known, we can, in principle, derive the probability density function for the FPT from (5.7). This does not necessarily mean that we can then find an expression for the original $T(x, t|x_0)$, because an inverse transform may not exist.

At this point, we have already asssumed that the probability density function of the process, $P(x,t|x_0)$ is not known, but we know that being a diffusion process it satisfies the Kolmogorov or backward diffusion equation (4.18),

$$\frac{\partial P(x,t|x_0)}{\partial t} = \lambda \frac{\partial P(x,t|x_0)}{\partial x_0} + D\frac{\partial^2 P(x,t|x_0)}{\partial x_0^2}. \tag{5.8}$$

The Laplace transform of $\partial P(x,t|x_0)/\partial t$ with respect to t can be easily evaluated as $sP_s(x|x_0) - \delta(x-x_0)$, and considering that $x_0 < S < x$, we have, from (5.8),

$$sP_s(x|x_0) = \lambda \frac{\partial P_s(x|x_0)}{\partial x_0} + D\frac{\partial^2 P_s(x|x_0)}{\partial x_0^2}$$

that according to (5.7) transforms to

$$D\frac{\partial^2 T_s(S|x_0)}{\partial x_0^2} + \lambda \frac{\partial T_s(S|x_0)}{\partial x_0} - sT_s(S|x_0) = 0. \tag{5.9}$$

We have derived a linear differential equation for $T_s(S|x_0)$ from an integral equation for $T(S,t|x_0)$, whose solution can be shown to be of the form

$$T_s(S|x_0) = c_1 \exp\left(r_+ \frac{x_0}{2D}\right) + c_2 \exp\left(r_- \frac{x_0}{2D}\right) \tag{5.10}$$

where c_1 and c_2 are constants to be determined and $r_\pm = -\lambda \pm \sqrt{\lambda^2 + 4sD}$. The constants in (5.10) are determined from the boundary conditions on the function $T_s(S|x_0)$. First of all, from (5.7) we have the boundary condition $T_s(S|S) = 1$, while the other condition is given by the boundness of $T_s(S|x_0)$. T is bounded by definition, since $\int T(S,t|x_0)dt \leq 1$, and for its Laplace transform, we can apply the Cauchy-Schwartz inequality,

$$\left[\int_0^\infty e^{-st} T(S,t|x_0)dt\right]^2 \leq \int_0^\infty e^{-2st}dt \cdot \int_0^\infty [T(S,t|x_0)]^2 dt < +\infty.$$

The first integral on the right-hand side is $1/2s$, and the second is bounded too, because it must be null for zero and for large t, and bounded in between. The limiting case can be a Dirac delta distribution for T, but that is indeed integrable. To fulfill the boundness condition forces us to set $c_2 = 0$ necessarly in (5.10), and after using $T_s(S|S) = 1$ we finally obtain

$$T_s(S|x_0) = \exp\left[\frac{\lambda}{2D}(S-x_0)\right] \exp\left[-\frac{S-x_0}{2D}\sqrt{\lambda^2 + 4sD}\right].$$

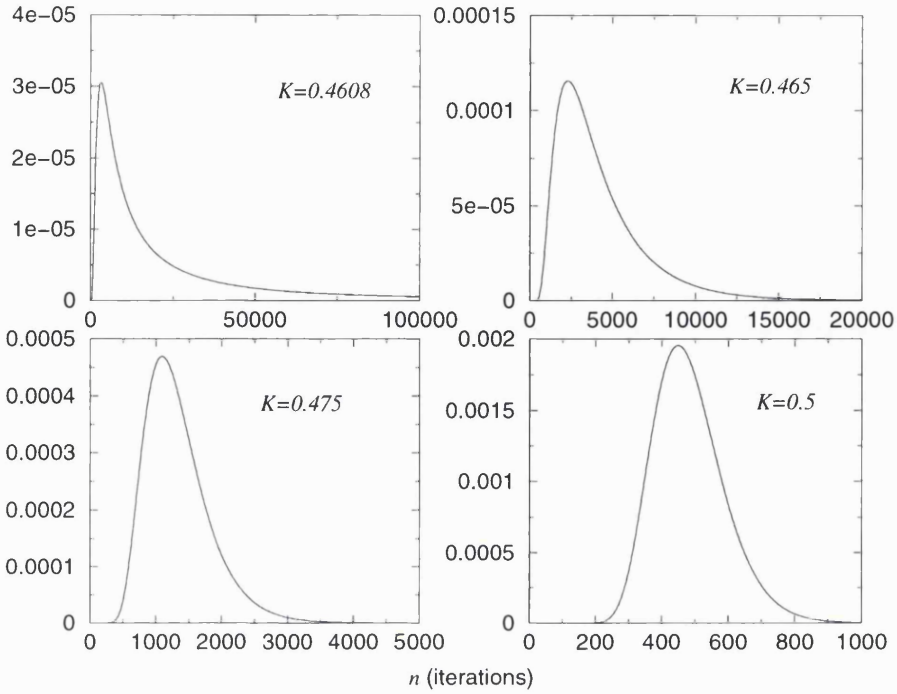

Figure 5.4: Four plots of the probability density function for the first passage time $T(S,t|x_0)$ (5.11) for the coupled skewed tent map. The values of K used in expression (5.11) are the same used for the numerical experiments in Figure 5.2.

The inverse Laplace transform, $\mathcal{L}^{-1}$ in this case can be calculated. Taking into account the change of coordinates $p = \lambda - 4sD$, and that for $F(p) = e^{-a\sqrt{p}}$,

$$\mathcal{L}^{-1}[F(p);t] = \frac{a}{2\sqrt{\pi t^3}} \exp\left(-\frac{a^2}{4t}\right)$$

we finally obtain

$$T(S,t|x_0) = \frac{S-x_0}{\sqrt{4\pi D}} t^{-3/2} \exp\left[-\frac{(S-x_0-\lambda t)^2}{4Dt}\right]. \tag{5.11}$$

In this formula, the dependence on K is through the drift coefficient $\lambda = -\lambda_\perp = -\log(1-K) - \Lambda$ only, as in (4.4).

We found an analytical expression for $T(S,t|x_0)$ without knowing the expression for $P(S,t|x_0)$. The relation (5.11) shows a time dependence $t^{-3/2}$ for small λ (that is, $(S-x_0)^2/2D \ll t$), that agrees with the laminar length distribution found in on-off intermittency in [Heagy *et al.* 94a], discussed in Chapter 2. In Figure 5.4 we show four plots of $T(-\log A, t|0)$ for several values of K for two coupled skewed tent maps, recalling that the drift coefficient is given by $\lambda = -\lambda_\perp$, and the

diffusion coefficient D given by (4.32). The comparison of this Figure with Figure 5.2(bottom), shows a qualitative good agreement, although there is a difference of scales.

5.4 Coupled Duffing oscillators

A single driven Duffing oscillator,

$$\ddot{x} + \mu\dot{x} - x + x^3 = A\cos(\omega t) \tag{5.12}$$

is a second-order non autonomous differential equation that describes the motion of a unit mass particle in a double-well potential, subject to viscous damping and forced by a cosinusoidal term [Moon & Holmes 79, Thompson & Stewart 86], from earlier studies by G. Duffing [1918]. Two identical oscillators are then coupled together, with a unidirectional coupling type to yield:

$$\begin{cases} \ddot{x} + \mu\dot{x} - x + x^3 = A\cos(\omega t) \\ \ddot{y} + \mu\dot{y} - y + y^3 + K(y - x) = A\cos(\omega t). \end{cases} \tag{5.13}$$

The Eqs. (5.13) represent an extended system in which, in addition to the forcing term $A\cos(\omega t)$, the x system can be thought of as a driving for the slave or response y system through the coupling term, where K is a real non-negative parameter. This type of coupling produces (with $\dot{t} = 1$) an extended 5-dimensional system for which the invariant set $x(t) = y(t)$ exists, *i.e.* a synchronised motion.

Different choices of the parameters μ, A, and ω can lead to very different behaviour of a single forced pendulum, so we expect the increasing dimension of the phase space in the systems (5.13), formed by the coupling of two of these systems, to show an even richer set of possible different solutions. We decided here to show one simple case, that we believe being highly interesting.

Consider the parameter values $\mu = 0.1$, $\omega = 0.3$. The act varying the forcing A produces the bifurcation diagram shown in Figure 5.5, while the particular choice $A = 3.0$ produces a stable cross-well chaotic response as the only stable attractor for the system (5.12), where the Poincaré surface of section is shown in Figure 5.6.

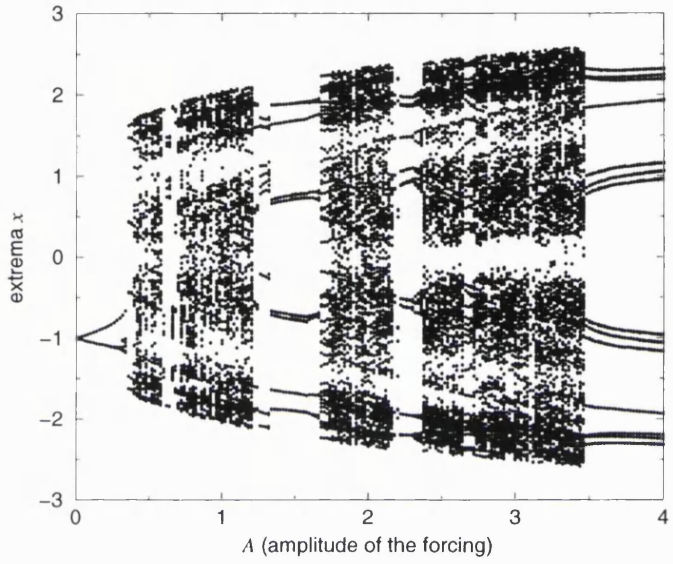

Figure 5.5: Bifurcation diagram obtained by sampling the relativa extrema (maxima and minima) of the time series of $x(t)$ for the forced Duffing oscillator, Eq. (5.12), for the parameter values $\mu = 0.1$, $\omega = 0.3$, and variable amplitude of the forcing A.

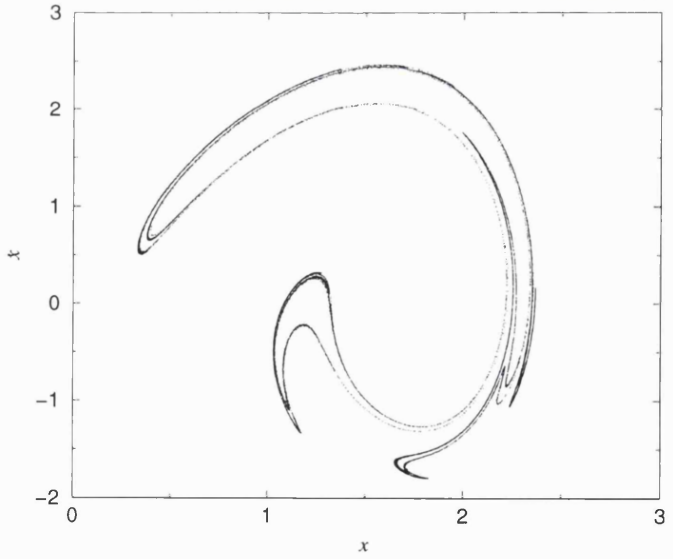

Figure 5.6: Poincaré section for the forced Duffing oscillator, with $A = 3.0$.

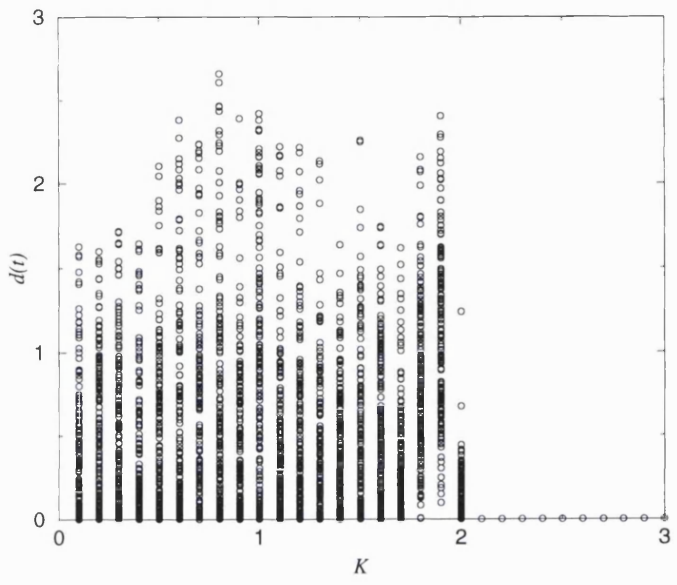

Figure 5.7: Plot of several values of the Euclidean distance $d(t)$ between the trajectories $(x(t), \dot{x}(t))$ and $(y(t), \dot{y}(t))$ for different values of K. The transition to a stable synchronised state is located approximatively at $K_{thr} = 2.0$.

To illustrate the synchronisation property (for the moment regardless of the time to convergence) we consider the parameters for both systems to be identical as previously defined. Thus, without loss of generality, if we select initial conditions for the driving system (x) to be $(x_0, \dot{x}_0) = (1.1, -0.5)$ the variable x will undergo a chaotic motion. The initial conditions for the slave system (y) are set at $(y_0, \dot{y}_0) = (1.0, -0.9)$, and using a usual Runge-Kutta numerical scheme the full system (5.13) may be integrated. The Euclidean distance $d = \sqrt{(x-y)^2 + (\dot{x}-\dot{y})^2}$ between the two trajectories is monitored for various choices of the coupling parameter K, as shown in Figure 5.7. In this plot the system is set to run for approximately 70 cycles of the periodic forcing to allow for the decay of transients. Over the next 10 cycles an average of the mean value between successive maxima and minima of the function $d(t)$ is evaluated. For $K = 0$ the two systems are independent and they show an average distance $\overline{d} \simeq 1.5$ (approximatively half of the size of the attractor); increasing the value of the coupling parameter we see from the average distance that the transition to the synchronised state occurs at $K_{thr} \simeq 2.0$ for this numerical experiment, whereafter the two subsystems display the same output. For values of K greater than K_{thr} the synchronised state is stable. This scenario

is specifically for the initial conditions given but different initial conditions would qualitatively produce the same response.

Defining a precise threshold value (*i.e.* for all initial conditions) of the coupling parameter for the convergence of the dynamics onto an invariant subspace involves two intrinsic problems:

1. For low values of K the invariant set is strongly unstable and for high values is strongly stable, while for values of the coupling constant close to the threshold, weak stability/instability causes the basin of attraction for the convergence onto the subset to have a very complicated structure, even in regions very close to the invariant set. So distinct pairs of initial conditions $(x_0, \dot{x}_0)$, $(y_0, \dot{y}_0)$ may lead to slightly different values for K_{thr}.

2. Simulations for locating the synchronisation threshold, or for computing characteristic exponents, are produced by running the integration over a finite time, supposed to be large enough to avoid problems of transient time. The length of the transient time may depend on the coupling parameter and on the initial conditions, and as yet no distribution is known for this latter.

Returning to the question of the time to synchronisation, in relation to the second problem above, we plot, in Figure 5.8, two typical curves representing the full evolution of $d(t)$ (in linear-log scale), for two values of K above the synchronisation threshold, now without ignoring the first 70 cycles. The time, here expressed in cycles of the periodic forcing $(2\pi/\omega)$, has been left running until $d(t) = 0$ exactly up to the precision of the computer. The two curves are computed for identical initial conditions (given in the caption) but $K = 2.7$ and $K = 2.05$, so that the invariant subset has two different degrees of stability, and we note that the observed decay is qualitatively different. The evolution of $d(t)$ when $K = 2.7$ can be notionally split into three different parts. The first evolution (τ_o), until approximatively 50 cycles of the periodic forcing, shows no appreciable change in the order of magnitude of the distance measure $d(t)$ (about unity), and in fact it is related to the chaotic wandering that the response system is performing about the attractor of the driving system, so that an approximate horizontal line can be seen. After this, in the

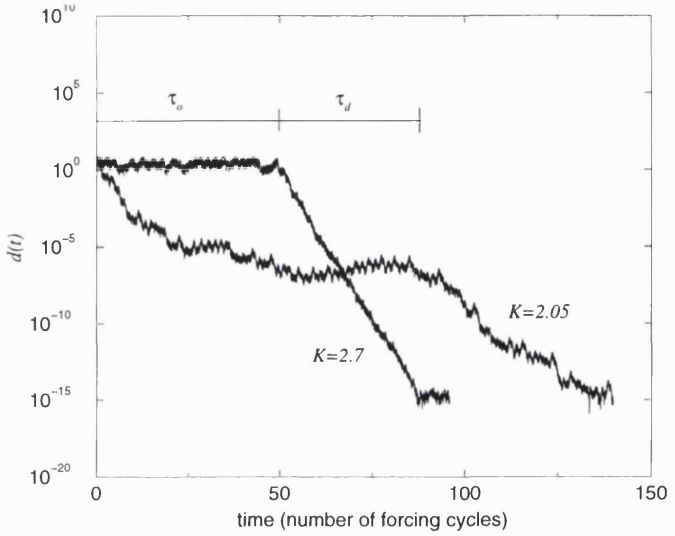

Figure 5.8: Two curves representing the time evolution of the Euclidean distance $d(t)$ between the drive and the response trajectories for the parameter values $\mu = 0.1$, $\omega = 0.3$, $A = 3.0$ with coupling parameter $K = 2.05$ and $K = 2.7$. The initial conditions that generate these two plots are the same, namely $(x_0, \dot{x}_0) = (3.1, -1.1)$ and $(y_0, \dot{y}_0) = (1.1, -0.5)$, but the different value of the coupling constant leads to qualitatively different decay onto the invariant subset. For the curve with $K = 2.7$ we have labelled the time intervals of the orbiting transient as τ_o and decaying transient as τ_d.

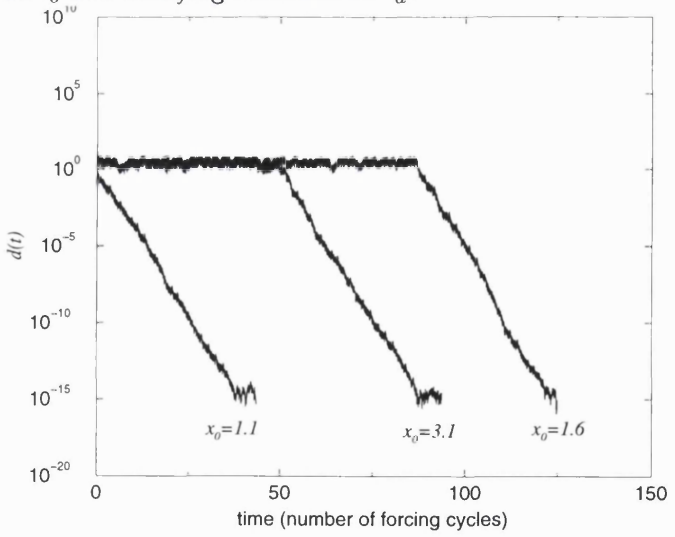

Figure 5.9: The behaviour of $d(t)$ for three cases of convergence onto the synchronised subset of Eqs. (5.13) for the parameter values as in the previous Figures, $A = 3.0$ and $K = 2.7$. In all cases the initial conditions for the slave system are set to $(y_0, \dot{y}_0) = (1.1, -0.5)$. For the driving system we set $\dot{x}_0 = -1.1$ and choose three different values for x_0 as reported below each plot.

time interval τ_d, the trajectory starts to decay towards the synchronised state, and in logaritmic scale its decay is almost linear, demonstrating an exponential dependence of the form $d(t) \propto \exp(\lambda t)$, with a rate of contraction $\lambda < 0$. After approximatively 80 cycles $d(t)$ reaches the level of roundoff error, where a pseudo-random oscillatory phenomenon takes place for values of $d(t)$ around 10^{-15}. We refer to the first non-decaying part of the transients τ_o as the *orbiting transient*, while the second part τ_d the *decaying transient*. When $K = 2.05$ the degree of stability is weaker than in the previous case (this statement can be quantified by the largest transverse Lyapunov exponent), and this condition is reflected in the decay of $d(t)$, for which a division of the trajectory into qualitatively different decaying parts is no longer possible. It seems reasonable that the decaying part of the transient is an exponential function of time, with the maximum transverse Lyapunov exponent as coefficient of the exponential. We show in the following that a linear fit of the decaying transient in logaritmic scale is indeed very close to the maximum transverse exponent. What is actually less clear is if there is any distribution for the orbiting transient. Another intuitive comment is that when the motion in the invariant subset posesses a weaker stability, transients will produce longer relaxation times, so we might expect longer orbiting transients on average, a condition that is already fulfilled by the decaying part of the transient.

The orbiting transient is dependent on the intial conditions chosen. In Figure 5.9 we show curves representing the evolution of $d(t)$, again on linear-log scale, with $K = 2.7$ fixed, for three different initial conditions. More precisely, $(y_0, \dot{y}_0) = (1.1, -0.5)$ and $\dot{x}_0 = -1.1$ are kept fixed, and we use three different starting points x_0, as given in the figure below each end point of the three curves. The slope of the linearly decaying part or the decaying transient for each of the three curves is almost the same, corresponding to the intuitive conjecture that the convergence is governed by the strength of dissipation transverse to the invariant subset. However, the three trajectories shown converge in very different times; almost a delay of approximatively 50 cycles of the forcing for $x_0 = 3.1$ when compared to the trajectory starting at $x_0 = 1.1$. If we look closer at the trajectory of the response system in the phase space, we see that this is not just simply orbiting

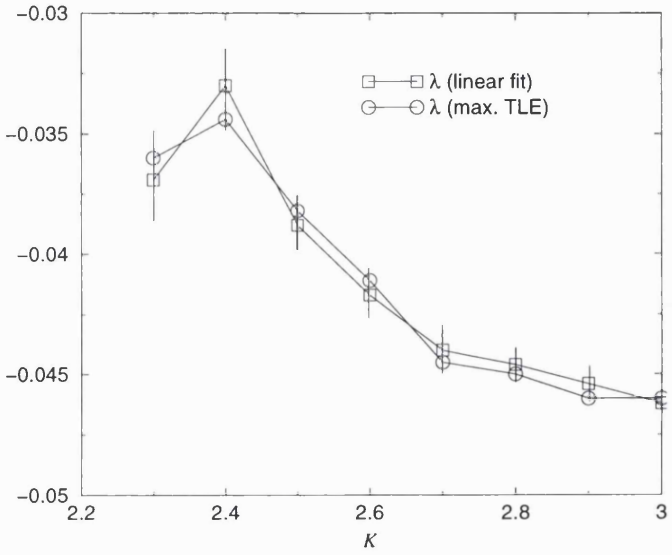

Figure 5.10: Estimates of the linear fit compared to the transverse Lyapunov exponent (TLE) for a variation of K. The circles represent the computed value of the maximum, while the squares represent the fitted values of the slope of the decaying transient for a trajectory in linear-log scale as in Figure 5.9. The linear fit is averaged over 20 initial conditions for each value of K, and the respective error bars are shown.

about the attractor of the driving, but rather it is performing a different orbit, larger in size that the orbit of the driving system. A transient trajectory of the response system $(y, \dot{y})$ before synchronisation is achieved is shown in Figure 5.11. This type of trajectory (either steady state or transient) has not been seen in the single Duffing oscillator. We conjecture that this orbiting transient is following a path close to either of an unstable orbit of the extended system in $\mathbb{R}^4 \times \mathbb{S}^1$, or perhaps the path of a solution (stable or unstable) that no longer exists, but which can be found in some nearby region of parameter space.

5.5 Transient Distribution

We have seen in Figure 5.8 that not all transients behave the same but, for all cases in which we have been able to divide the trajectory into different parts (*e.g.* the curve for $K = 2.7$ in Figure 5.8, and all curves in Figure 5.9), we can linearly fit the decaying part (τ_d) in linear-log scale. The comparison between the slope of this fit and the maximum transverse Lyapunov exponent (denoted TLE) is given

in Figure 5.10 for values of K between 2.3 and 3.0 in steps of 0.1. For $K < 2.3$ a trajectory may still undergo orbiting and decaying transient behaviour, as described in the previous section, but the evaluation of a suitable linear fit becomes much less accurate. Moreover, progressively lowering the coupling parameter, as we approach K_{thr} from above, we expect to find decaying trajectories which resemble the curve for $K = 2.05$ in Figure 5.8. The maximum transverse Lyapunov exponent $\lambda_\perp$ has been computed as rate of contraction of perturbations transverse to the synchronised state, *i.e.* as the Lyapunov exponent of the difference system $(x - y, \dot{x} - \dot{y})$. The values reported for the fit λ, and for the maximum transverse Lyapunov exponent $\lambda_\perp$ have been obtained as an average of 20 different initial conditions for each value of K. All the values obtained for the fit were very close to the average, with a standard deviation of the order of 10^{-4} for almost all values of K. The estimate for $K = 2.3$ showed a less precise fit, with standard deviation 5×10^{-4}.

Finally, in Figure 5.11 we show four plots to summarize this dynamical situation. Our aim is to determine whether, once all parameters are fixed, there is any particular spatial or time distribution for the transient time given a representative set of initial conditions in the phase space. Again using the fixed parameters used in Eqs. (5.13), and fixed K, we set the initial conditions for the response system to be $(y_0, \dot{y}_0) = (1.1, -0.5)$ and we vary $(x_0, \dot{x}_0)$ denoting $x_0 = y_0 + \xi_0$ and $\dot{x}_0 = \dot{y}_0 + \eta_0$. We follow here the natural choice of varying the initial conditions of the driving system. Setting a grid of (ξ_0, η_0) values, for each (ξ_0, η_0) chosen, we run time forward until the Euclidean distance $d(t)$ reaches a cutoff value of 10^{-6}. The distance $d(t)$ in the plots before did not show on-off intermittent behaviour. We checked that the qualitative features of the distribution of transient time to synchronisation are not changed in decreasing the cutoff used (10^{-6}). For K fixed the slope of the decaying transient, in linear-log scale, is almost the same for all initial conditions, so a fixed cutoff will give us a faithful representation of the orbiting transient times τ_o.

The results of the computations carried out for the case $K = 3.0$ are given in Figure 5.11. On the upper left diagram we show a histogram describing how all

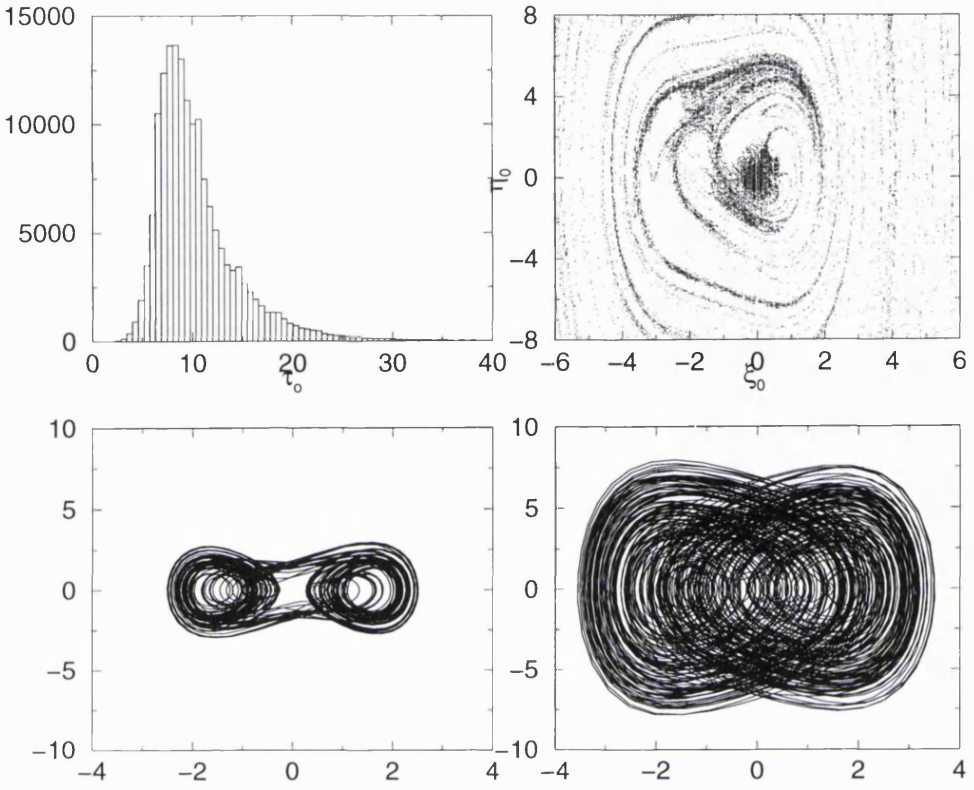

Figure 5.11: Upper panel: Time distribution of the initial points (ξ_0, η_0) for increasing orbiting time τ_o for $K = 3.0$, and spatial organization of the initial conditions in the pre-peak region of the previous histogram, in the (ξ_0, η_0) plane. Lower panel: Attractor of the drive system (left) and a phase plane representation of the trajectory of the response system (right) in its state of orbiting transient before synchronisation takes place.

initial conditions in the grid distribute themselves with respect to their orbiting time τ_o. This "density" plot shows a peak at about $\tau_o \simeq 8$, and we can ideally divide the distribution into three parts; as a distribution before the peak (these are the points whose synchronisation is the fastest), then the peak, that contains almost all the "mass" of the distribution, and then finally the tail, formed by all points achieving synchronisation in the longest time possible (at least, within the grid we set). For $K = 3.0$, initial conditions which achieve synchronisation slowest take about 40 cycles of the periodic forcing. The picture in the top right of Figure 5.11 shows a spatial organization of the initial conditions whose synchronisation is in the pre-peak region, arbitrarly taken at $\tau_o < 6$ cycles of the forcing. The initial conditions are taken in the range $[\xi_0, \eta_0] = [-6, 6] \times [-8, 8]$. The first thing we can notice is that the distribution of points shows some organized shape, indicating the

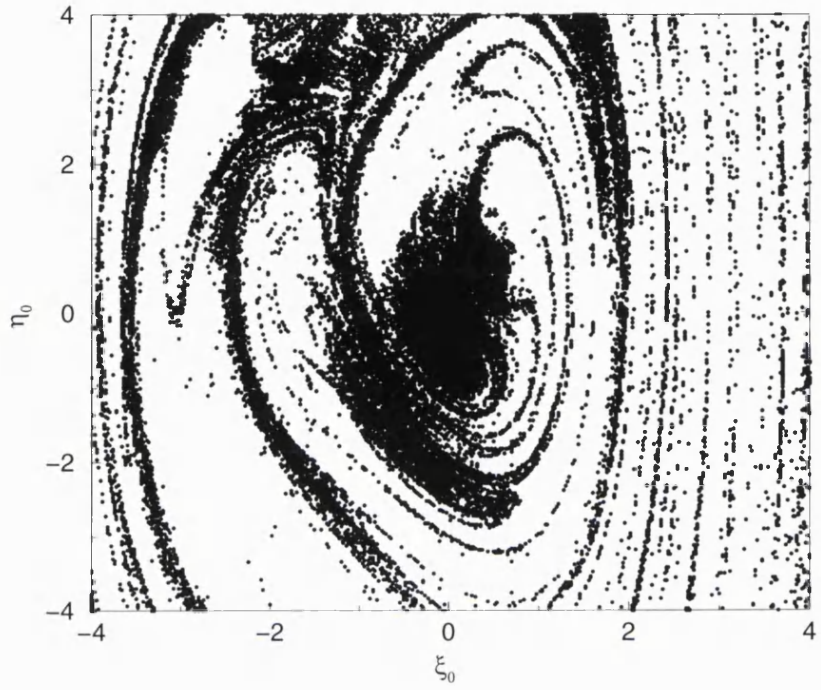

Figure 5.12: Spatial distribution for $\tau_o < 6$ of points converging fastest onto $\mathcal{S}$. The section, already shown in Figure 5.11, is drawn here in the interval $[\xi_0, \eta_0] = [-4, 4] \times [-4, 4]$, to better reveal its structure.

existence of privileged zones of the phase space in which the convergence towards the invariant subset is the fastest, taking into account also the arbitrarity of the section cut. Figure 5.12 shows an enlargment of this distribution of initial points in order to enhance its seemingly fractal structure closer to the $(\xi_0, \eta_0) = (0, 0)$. To check the robustness of the distribution in the presence of noise, we have repeated the same procedure as above but introducing noise in both the drive and response systems. The amplitude of the noise has been increased up to 10^{-6}, without any considerable change in the shape of the pre-peak section, and in some enlargments of it.

The two lower pictures of Fig. 5.11 represent the dynamics of the drive (left) and response (right) systems in the phase space for a trajectory which displays very delayed synchronisation. The two pictures are shown to the same scale, to illustrate the difference of the pre-synchronised transient. The left picture shows a trajectory of the cross-well motion typical of the Duffing oscillator, for initial conditions of the driving $(x_0, \dot{x}_0) = (1.6, -1.1)$. The first 50 cycles of the response

system are shown in the lower right part of Figure 5.11, for initial conditions $(y_0, \dot{y}_0) = (1.1, -0.5)$. This picture is produced using the same initial points as the third time history in Figure 5.9, where a τ_o of approximatively 80 cycles of the forcing are displayed. In this case the value of K is different, but still the numerical integration produced a time history with very long orbiting transient. For $t < \tau_o$ the orbit displays the spatial evolution of the orbiting transient before convergence to synchronisation state, after which the trajectory rapidly settles onto the attractor displayed in the lower left picture. The orbit of the response is not a simple chaotic wandering about the attractor of the driving, but instead it performs a different orbit, before suddenly converging onto the driving.

We show in Figure 5.13 the time and spatial distribution of the initial points (ξ_0, η_0) in the case $K = 2.4$, in order to see which major changes can possibly occurr. As expected, the tail of the distribution is now much longer, intuitively, because approaching the bifurcation we expect longer relaxation times, although the position of the peak is not relevantly changed. The comparison of the orbiting time distribution with the plots of the distribution $T(n)$ in Figure 5.1 (or with the probability densities $T(S, t|x_0)$ in Figure 5.4) shows that the gradual changes in the distribution of the first passage time seem qualitatively to be common to several different dynamical systems having a simple invariant subset. We checked the validity of this statement plotting for other values of K curves of distribution of orbiting transient, and the only difference noticed so far has been a very slow change of position of the peak of the distribution, compared with the mapping and theoretical cases. Regarding the spatial distribution then, from the second picture of Figure 5.13 we notice the presence of a certain non-trivial spatial arrangment in the space (ξ_0, η_0). We remind the reader that the transient motion of the response system for $K = 2.4$ looks qualitatively similar to the one for $K = 3.0$, shown in Figure 5.11.

As far as we can deduce, this orbiting transient is not following a stable orbit of the single Duffing equation. The fact that noise does not strongly influence the overall behaviour seems to indicate that neither it is following an unstable orbit of the full 5-dimensional system. This leaves the possibility that an orbit exists

in nearby parameter space onto which the transient orbit becomes trapped for a lenght of time before synchronisation occurrs.

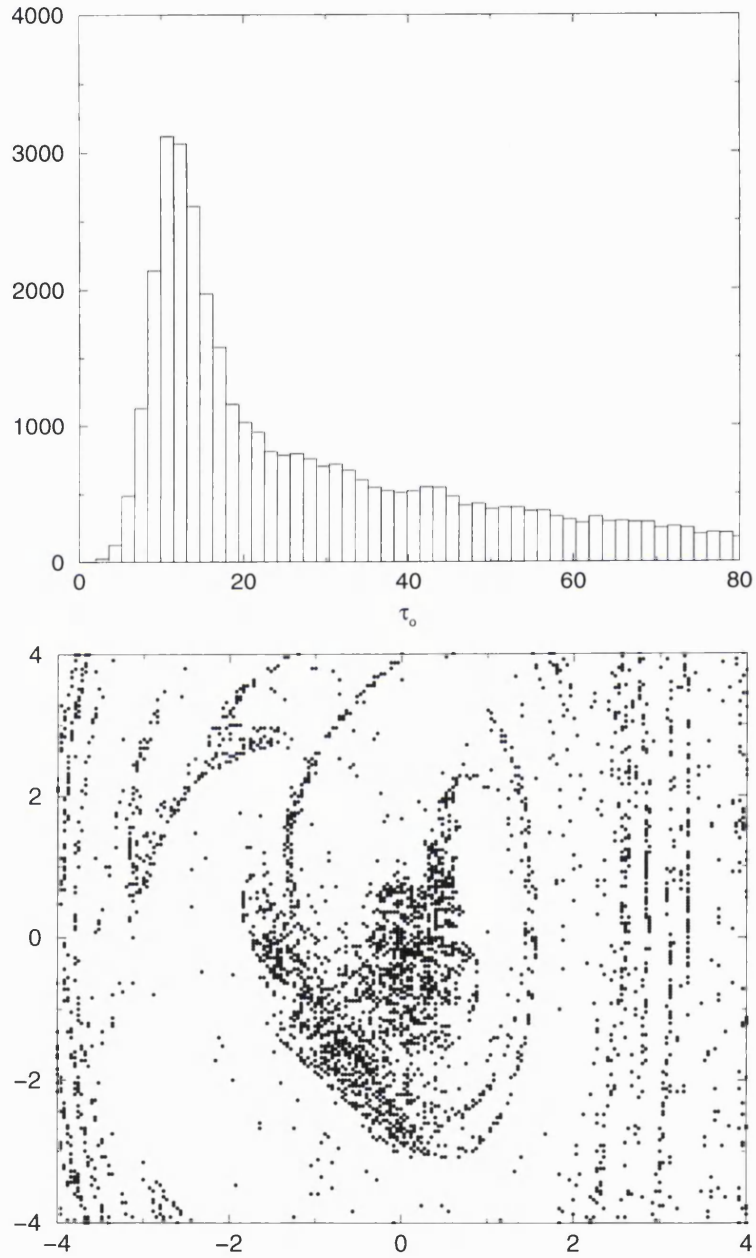

Figure 5.13: Upper picture: time distribution for the orbiting transient τ_o in the case $K = 2.4$. While the position of the peak is not relevantly increased, the tail of the distribution is now much longer. Lower picture: Spatial distribution of initial points (ξ_0, η_0) for the pre-peak zone for $K = 2.4$.

Chapter 6

Where will the research go?

In the previous chapters we have shown a detailed analysis of the process of synchronisation between two coupled oscillators. We noted the importance of this process in our understanding of the mechanism of self-organisation between globally coupled dynamical systems. This is particularly the case when no simple invariant subset exists, but we can still recognize that the motion of the coupled systems evolves in a lower dimensional portion of the whole phase space. We pointed out at the beginning that the synchronisation of chaos as a research theme became very popular only after the work of Pecora and Carroll [1990,91]. Ten years have almost passed, and we want to discuss here if subsequent extensive discussions have lead to any significant practical implications, or if the state of the art can give us some insight towards possible future directions of research. Synchronisation of chaos as a research issue may have sometimes attracted the impression of a phenomenon desperately in search of an application. Some discussion brought to the consideration of its application to the study of the cardiorespiratory system [Schäfer *et al.* 99], for example, although the phenomenon behind the various type of self-organized motion in coupled systems seemed to be suitably tackled via the *phase synchronisation* [Rosenblum *et al.* 96], that is defined as the equality of the phases of the two chaotic systems, or as a commensurate ratio between them, provided that a definition of phase exist for a chaotic system (see, for instance, [Rosenblum *et al.* 97]). Regarding the identical synchronisation as discussed in

this work, there is, for example, the interesting work of Gregory Duane [1997], who tackled the problem of synchronicity in high dimensional systems for a model of the large-scale atmospheric circulation patterns in the northern and southern hemispheres.

Anyway, since the work of Pecora and Carroll [1990,91], the first suggestion for using chaotic but synchronised systems was the application to secure transmission of signals. Chaotic signals have broadband Fourier spectrum, so they have the advantage to be used in principle as carriers for signals of different frequencies. This task was first performed by [Oppenheim *et al.* 92, Cuomo & Oppenheim 93], using the principle that if we have two identical nonlinear low-dimensional dynamical systems, where one variable for the first systems enslaves the second, this chaotic variable can be used as a carrier for the message. Using this idea, several different methods have been derived in recent years to achieve the task of transmitting a message hidden in a chaotic system, as in [Kocarev *et al.* 92, Murali & Lakshmanan 93], or the more complete list in [Pecora *et al.* 97]. Unfortunately, the comunication schemes that use synchronised chaos to transmit the message, although successful, are not secure. Linear regression schemes can provide an information on whether spurious bits have been introduced in a chaotic time series. On top of this, Pérez and Cerdeira [1995], as well as [Yang *et al.* 98] finally proved themselves able to unmask a message that has been encoded by chaotic synchronisation, either in a digital or analog way.

6.1 Periodic orbit theory

We briefly mentioned in Chapter 4 that a random walk model fails to be a good approximation of a system of coupled chaotic tent maps. A skewed tent map and a random evolution in the unit interval have the same statistical properties, based on the fact that they have the same probability distribution. The big difference is that for a chaotic, but deterministic, evolution not all points in the phase space have the same importance. The phase space of a chaotic system is filled with unstable periodic orbits whose presence influences the chaotic wandering of the trajectory.

Rather than "influences", we can state that the distribution of unstable periodic orbits in the phase space acts as a skeleton for the chaotic attractor that, according to [Cvitanović *et al.* 88] can thus be seen as a random wandering on the union of all periodic points. It is thus interesting to study whether we can discuss, or even quantify the stability of a chaotic invariant subset interpreting the chaotic motion in the subset via its "skeleton" that is, the distribution of all its unstable periodic points.

As a first example of our discussion, we show, in Figure 6.1 a case of two coupled skewed tent maps as studied before in the previous two chapters. The stable output of the dynamics is the on-off intermittency studied in Chapter 2. The first two pictures from the top show a series of 10000 iterations for this system, the second one of which, in linear-log axis. The trajectory of $|z_n|$ in this latter is seen wildly fluctuating, with sudden reversals of its direction towards or away from the invariant subset. A rectangular box is indicated with an arrow, and the enlargment of that portion of trajectory is shown in the third picture from the top. The bottom picture shows a time series of the driving system x where at approximately $n = 6825$ the trajectory spends a long time close to an unstable fixed point. During this time $|z_n|$ experiences a contraction towards $|z| = 0$, roughly of about 3 orders of magnitude. This clearly indicates that although the zero fixed point of the skewed tent map is an unstable point, the same point is *transversely stable* in $\mathcal{S}$. If the driving system could be placed exactly in that fixed point, the system will experience a uniform contraction towards $\mathcal{S}$, although typical initial conditions lead to orbits that never converge onto it. As well as the unstable fixed point, there are certainly other unstable periodic solutions of the skewed tent map that are transversely stable in $\mathcal{S}$, as well as other transversely unstable. If we also consider that there are an infinite number of periodic points embedded in a chaotic attractor, this implies that the blowout bifurcation is a major change in a chaotic system induced by an infinite number of unstable periodic orbits, unlike many other cases of crises of bifurcation (like the boundary crises) in which only one periodic orbit is responsible of the change. The purpose of this section is to discuss whether from a knowledge of these periodic orbits we might be able to say

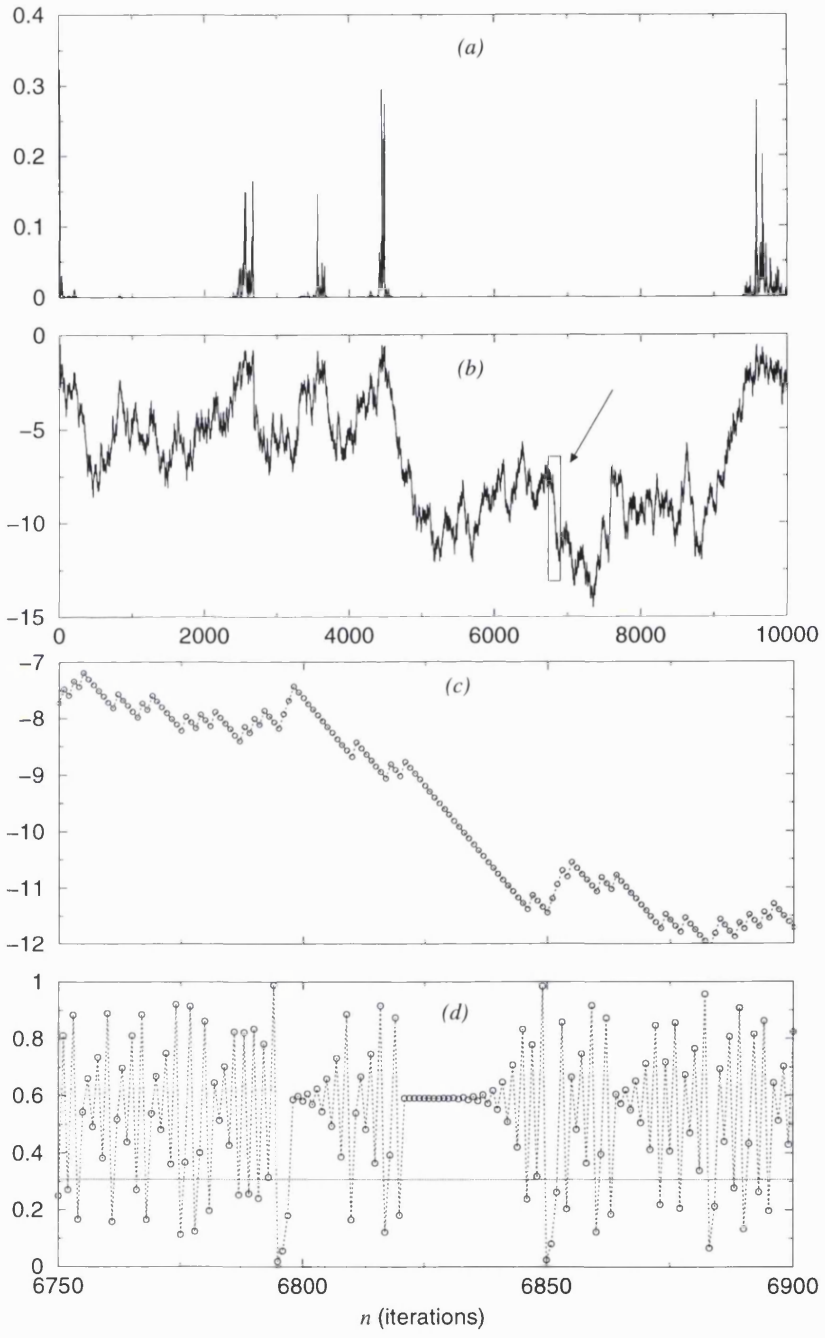

Figure 6.1: (a):Time series of $|z_n|$ of 10000 iterations for two coupled skewed tent maps with $c = 0.307$, showing on-off intermittency. (b): same as in picture (a), but showing $\log_{10}|z_n|$. The rectangular box indicated the enlargment that is shown in picture (c). (c): Enlargment of the logaritmic time series (with circles). (d): Corresponding behaviour of the driving system x_n, where at approximately $n = 6825$ the trajectory sets very close to the unstable fixed point.

something about the convergence in $\mathcal{S}$.

6.2 Organization of the unstable periodic orbits

We will use in this discussion the skewed tent map we have already treated previously. This will allow us some analytical treatment for its simplicity, and a comparison with the result we showed in the previous chapters for the same dynamical system. To avoid confusion, from now on, we define the variables as following:

- $K_{thr}(c)$ is the value of K in Eqs. (4.1) for a fixed c at which the blowout bifurcation is located. This symbol represents the *analytical* value, defined by $\lambda_\perp = 0$, Eq. (4.5). Λ and $\lambda_\perp$ are previously defined.

- Λ_m^p is the characteristic exponent for an unstable period-p orbit of the tent map with m iterates on the right and $p-m$ iterates on the left. $K_m^p = 1 - \exp(-\Lambda_m^p)$ is the K-value at which such an orbit change transverse stability.

It is evident that for any $c \neq \frac{1}{2}$ the unstable periodic orbit will have different locations, but a much greater difference is that for $c \neq \frac{1}{2}$ not all unstable periodic orbits will have the same characteristic exponent. We have

$$\Lambda^p = \frac{1}{p} \log\Big(\prod_{i=1}^{p} |f'(x_i)|\Big), \tag{6.1}$$

for the characteristic exponent of a period-p orbit. The expression (6.1) depends on the ratio m/p, and for fixed p (6.1) has the same value for the same number m, regardless of their ordering, *e.g.* for $p = 6$, the orbits "000111" and "001101" have the same Λ^6, which differs from the Λ^6 of "000101". From this fact and from (4.4) it follows that the two maps will display different threshold of stability K_m^p for every unstable periodic orbit within the chaotic invariant set.

For a period-p orbit with m iterates on the right and $p-m$ iterates on the left, by (6.1) Λ_m^p can be expressed as

$$\Lambda_m^p(c) = -\frac{1}{p} \log\{c^{p-m}(1-c)^m\}. \tag{6.2}$$

So every left iterate contributes with a factor c^{p-m}, while every right iterate with a factor $(1-c)^m$. From the formula (6.2) we can derive an expression for $K_m^p(c)$, *i.e.* the set of all points in K-space vs c at which a periodic orbit of period p, with m iterates on the right and $p-m$ iterates on the left (of the inversion point c), change stability transversely to $\mathcal{S}$,

$$K_m^p(c) = 1 - \exp(-\Lambda_m^p(c)). \tag{6.3}$$

Once c has been fixed, for all $K < K_m^p$ the orbit (p,m) is transversely unstable, while for $K > K_m^p$ the orbit (p,m) is transversely stable. As well as the set of all unstable periodic orbits embedded in a chaotic attractor is interpreted as its *skeleton*, we can think of all functions $K_m^p(c)$ as the *skeleton* of $K_{thr}(c)$. What are the properties of all functions $K_m^p(c)$? We have stated a few (in what follows we always consider $m \leqslant p$, with m, p integers):

1. $K_m^p(\frac{1}{2}) = \frac{1}{2}$, $\forall m, p$. All curves $K_m^p(c)$ cross each other all in $\frac{1}{2}$ only. From this property, for a symmetric tent map all periodic orbits change stability in $\mathcal{S}$ at $K = \frac{1}{2}$.

2. $\lim_{c\to 0^+} K_m^p(c) = \lim_{c\to 1^-} K_m^p(c) = 1$.

3. $K_m^p(1-c) = K_{p-m}^p(c)$. Here is stated that for a particular (p,m) orbit, with its function $K_m^p(c)$, the orbit $(p, p-m)$ has a function $K_{p-m}^p(c)$ symmetric with respect to $c = \frac{1}{2}$ to the function $K_m^p(c)$. So that the set of all $K_m^p(c)$ for a fixed period-p distributes symmetrically for all available m. If $2m = p$, $K_m^p(c)$ is itself symmetric.

4. $K_{\alpha m}^{\alpha p}(c) = K_m^p(c)$, $\forall \alpha = 1, 2, \cdots$. Different orbits, but with same ratio $\frac{m}{p}$, have the same transverse stability. This is simply derived from (6.2), and comes about from the simple consideration that (p,m) and $(\alpha p, \alpha m)$ are the same orbit.

5. $dK_m^p(c^*)/dc = 0$ with $c^* = 1 - \frac{m}{p}$, $\forall m \neq 0 = 1, \cdots, p-1, p \neq 1$. All $K_m^p(c)$ functions have their minima for $c^* = 1 - \frac{m}{p}$.

6. $K_m^p(c^*) = K_{thr}(c^*)$. All the minima of the functions $K_m^p(c)$ stay on the curve $K_{thr}(c)$. This can be simply proven by noting that (6.3) can be rewritten as

$$K_m^p(c) = 1 - c^{1-\frac{m}{p}}(1-c)^{\frac{m}{p}},$$

in the same form of (4.8). The theoretical curve of $K_{thr}(c)$ (extracted with the natural invariant measure) can be seen as the set of points at which all unstable periodic orbits change stability with the minimum value of K.

7. The curves $K_0^1(c)$ and $K_1^1(c)$ define two triangular regions in which all other curves $K_m^p(c)$ are contained. This means that for all values of c except $\frac{1}{2}$ the unstable fixed points $x = 0$ and $x = 1/(2-c)$ are the first (or the last) solutions to change transverse stability in changing K.

8. The curve $K_1^2(c)$ acts as a separatrix between curves $K_m^p(c)$ and K_{p-m}^p. For example, for $c < \frac{1}{2}$, all curves with $2m < p$ have $K_m^p(c) < K_1^2(c)$, while for $2m > p$ (*i.e.* the symmetric ones) it is $K_m^p(c) > K_1^2(c)$. More generally, we have that for $c < \frac{1}{2}$ and fixed p, $K_m^p(c) < K_{m+1}^p(c)$, while the contrary holds for $c > \frac{1}{2}$.

6.2.1 Statistics of the unstable periodic orbits

In Figure 6.2 we represent some of the curves $K_m^p(c)$ together with $K_{thr}(c)$, in $c \in (0,1)$. The thick solid line shows the behaviour of $K_{thr}(c)$. The function has a maximum in $c = \frac{1}{2}$, for which $K_{thr}(\frac{1}{2}) = \frac{1}{2}$. All other curves represent, respectively, the change of stability of the orbits $(p,m) = (1,1)$ (the fixed point $1/(2-c)$), (1,0) (the fixed point 0), and the periodic orbits (2,1), (4,3), and (10,9). From the figure it is possible to see that, for example, for $c \simeq 0.1$ and $K \simeq 0.4$, the orbits (1,0), (2,1), and (4,3) possess positive transverse exponents while $\lambda_\perp < 0$. So there are zones in the parameter space in which the chaotic attractor is transversely unstable, but some of the unstable periodic orbits embedded in it are stable in $\mathcal{S}$, and vice versa.

Different unstable orbits show different convergence onto $\mathcal{S}$, but we expect that the higher the period p is, more faithful is the representation they give of the

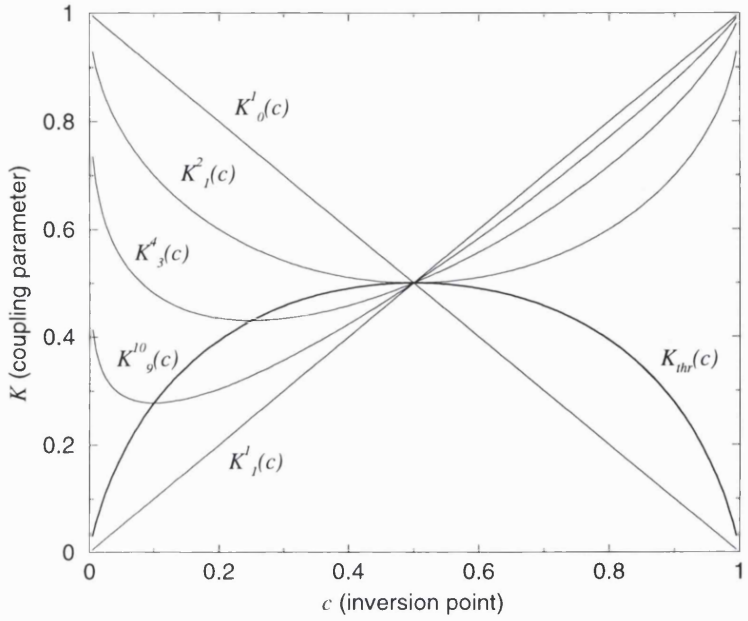

Figure 6.2: Several curves $K^p_m(c)$ and the curve $K_{thr}(c)$ (thick solid line) in the (c, K) parameter space. The spread of the stability lines of the different periodic orbits gradually decreases to zero for $c \to \frac{1}{2}$.

invariant measure. This point seems to be divergent with the local representation of the role of the unstable periodic orbit, since the dynamics is most influenced by the unstable orbits whose stable manifolds have a negative eigenvalue with high enough absolute value, a situation that is usually accomplished by the lowest period periodic orbits (as suggested by [Hunt & Ott 96]). We have numerical evidence that the latter are responsible for the *local* behaviour, as in Figure 6.1, while the former are responsible for the *global* behaviour (in the statistical sense, they mimic the natural invariant density). We have already stated some of the properties of the unstable orbit (p, m), now we want to see what is the statistical behaviour of the ensemble of all them up to a certain order. The orbits (p, m) will contribute to a particular macroscopic observable according to their characteristic exponents Λ^p_m, and we can associate them the statistical weight $e^{-p\Lambda^p_m(c)}$. First of all we compute for some periodic orbits with period up to $p = 50$ all the values of $K^p_m(c)$ for a fixed c, and we associate to them a height proportional to their respective

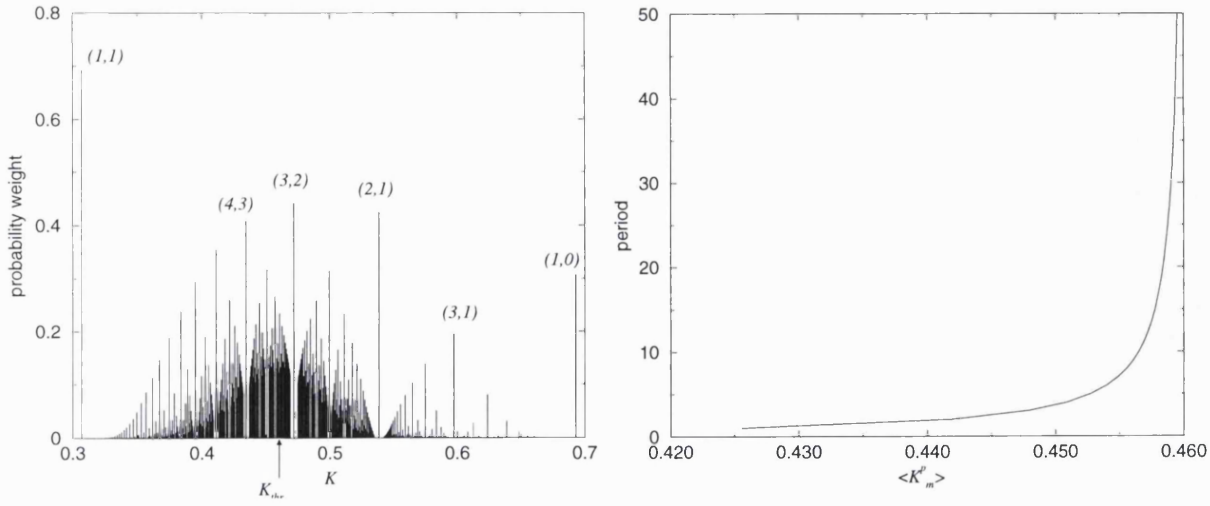

Figure 6.3: Left: Position of all K_m^p in the K-space for $c = 0.307$ up to $p = 50$, showing in the ordinate the probablity weight $\mathcal{P}_m^p$. The location of K_{thr} is indicated with a arrow. This series of peak in the abscissa, is actually a section of the previous graph for $c = 0.307$. Right: Evaluation of the quantity $\langle K_m^p \rangle$ for the skewed tent map with $c = 0.307$. In this case, $K_{thr} \simeq 0.4602$, as already known, and the curve shows convergence towards that value in increasing the period p.

weights, according to the formula

$$\mathcal{P}_m^p(c) = \frac{\binom{p}{m} e^{-p\Lambda_m^p(c)}}{\sum_{m'} \binom{p}{m'} e^{-p\Lambda_{m'}^p(c)}}. \tag{6.4}$$

The first thing we can see from the previous expression is that the denominator is always equal to one, due to the complete symbolic dynamics and to the particular expression of the map, according to which

$$\sum_{m=0}^{p} \binom{p}{m} e^{-p\Lambda_m^p(c)} = \sum_{m} \binom{p}{m} c^m (1-c)^{p-m} = (c+1-c)^p = 1. \tag{6.5}$$

We are already able to locate exactly the position of all K_m^p for all c from (6.3), that are shown in Figure 6.3(left) in the K-space for $c = 0.307$ (for p up to 50 and $m = 0, p$), showing in the ordinate the probablity weight $\mathcal{P}_m^p$. The probability weight $\mathcal{P}_m^p$ can average the contribution of all periodic orbits in determining an average value of $\langle K_m^p \rangle$ that, if correct, should converge towards K_{thr} in increasing the period of the orbits considered. The result is actually shown in Figure 6.3(right), where the quantity

$$\langle K_m^p \rangle = \sum_{p,m} \binom{p}{m} e^{-p\Lambda_m^p(c)} K_m^p \tag{6.6}$$

is evaluated for all periodic orbits of period up to $p = 50$. The graph shows that the evaluation goes towards the correct value ($K_{thr} \simeq 0.4602$ for $c = 0.307$ in the graph) increasing p.

Actually, a curious and unexpected result can easily be obtained: suppose we want to weight the value of $\lambda_\perp$ with the periodic orbits. From the formula (4.4), we know we have to evaluate the quantity

$$\langle \lambda_\perp \rangle = \sum_{p,m} \binom{p}{m} e^{-p\Lambda_m^p(c)} [\log(1-K) + \Lambda_m^p(c)] \tag{6.7}$$

that for the tent map is simplified by considering that from (6.2), we have

$$e^{-p\Lambda_m^p(c)} = c^m (1-c)^{p-m} \tag{6.8}$$

and $\Lambda_m^p(c)$ is already given by the (6.2). Unfolding the sum in (6.7) may be quite cumbersome for p high enough, but if we look at simpler low-period expansion, *e.g.* for $p = 1$, we have the only two contributions $m = 0, 1$, and the (6.7) becomes

$$\log(1-K) + \sum_{p=1,m=0,1} \binom{p}{m} e^{-p\Lambda_m^p(c)} \Lambda_m^p(c) = \log(1-K) - [(1-c)\log(1-c) + c\log c]. \tag{6.9}$$

that equated to zero must represent the average threshold of synchronisation when the average is carried out weighting just on the fixed points. It is easy to see that this yields the formula (4.8)! The average with the fixed points have reproduced the one with the natural measure, but actually, the same average gives the same result with all values of p, when the sum over all $m = 0, p$ is considered.

One more tool we have for the investigation of the dynamics of coupled map system like (4.1) is the presence of the weight function $e^{-p\Lambda_m^p(c)}$. This weight function might help us to estabilish the correctness of the hypothesis of Nagai and Lai [1997], who claim that "*The [blowout] bifurcation occurs when there are approximately equal numbers of the transversely stable and the transversely unstable periodic orbits so that on average the the typical trajectory experiences an exactly equal amount of attraction towards and repulsion away from the invariant subspace* $\mathcal{S}$". This statement does not hold in the case we discussed on the coupled skewed tent maps, as it can be seen from Figure 6.2. We know that the curve

$K_1^2(c)$ has an equal number of curves K_m^p for the transversely unstable periodic orbits above, and for transversely stable periodic orbits below, but it does not coincide with $K_{thr}(c)$. Nevertheless, in [Nagai & Lai 97] the authors consider the possibility of using an appropriate weight function associate to each periodic orbit. The location of the curve K_1^2 for $c = 0.307$ in Figure 6.3(left) is not the same as K_{thr}, but we have to consider the evident asymmetry in the distribution of the weight $\mathcal{P}_m^p$. According to the formula (6.4), the weight $\mathcal{P}_m^p$ is higher when when an orbit (p, m) is of low period, when the binomial coefficient $\binom{p}{m}$ is large, but also when its characteristic exponent Λ_m^p is very small. The smaller Λ_m^p is, the longer the chaotic wandering of a trajectory will remain close to it, because the repulsion away from it is exponentially strong in Λ_m^p. It is not surprising so that, in Figure 6.3(left), K_{thr} is shifted away from K_1^2 towards the K_m^p points related to orbits (p, m) with large $\mathcal{P}_m^p$. After these considerations we can draw a scenario for a "Periodic-orbit theory" for a blowout bifurcation, inspired from [Nagai & Lai 97]. If there are N_+^p orbits of period p transversely unstable and N_-^p stable, we can argue that a blowout bifurcation takes place when there is an equal attraction to and repulsion from $\mathcal{S}$. In other words, when

$$\sum_{p,m} N_+^p(m)\mathcal{P}_m^p = \sum_{p',m'} N_+^{p'}(m')\mathcal{P}_{m'}^{p'}.$$

6.3 Diffusion approximation

The research in the fourth and fifth chapters relied on the theory of diffusion processes in an attempt to describe the motion of a chaotic system with an invariant subset. Using a model like (4.1) with a base dynamics represented by a piecewise-linear map, the skewed tent map, the diffusion approximation provided a good representation of the behaviour of the system (4.1) close to the blowout bifurcation. Better stochastic models are likely to give better representations of the dynamical behaviour of such systems, but it would be very interesting to see whether the dynamics can help in building a more realistic stochastic model for a deterministic system. We may argue that in the case of synchronised behaviour there is a major

advance, suggested in [Fujisaka & Yamada 86b] with the so-called *multiplicative noise model*, for an intermittent process caused by chaotic modulation.

To introduce this model, we remind that we presented, in the previous Chapter, the origin of the DDA as a simulation of the RWM, although diffusion processes arise from statistical considerations on dynamical systems even when the base dynamics is not piecewise linear. Let us consider the dynamical evolution of the variable $|z_n|$ which measures the deviation from the invariant subset $\mathcal{S}$. If the deviation is small, we know that $|z_n|$ grows (or shrinks) like $|z_n| \sim \exp \lambda_\perp n$ on average, which is a solution of the equation

$$|z_{n+1}| = f_n |z_n| = (1 - K)|f'(x_n)| \cdot |z_n|$$

where we consider n as a continuous variable, admissable if n is large. The term f_n denotes the local contraction rate transverse to the direction of the motion in $\mathcal{S}$. Taking the logarithm of both sides, we have

$$\log |z_{n+1}| = \log f_n + \log |z_n| \tag{6.10}$$

In the limit of large n it is obviously $\lim_{n\to\infty} \log f_n = \lambda_\perp$ with probability 1, independent of n. We can now write

$$\log f_n = \lambda_\perp + \eta_n$$

where η_n is a stochastic variable representing the fluctuation of the TLE with respect to its ergodic limit $\lambda_\perp$. Combining the two, we can write

$$\frac{d \log |z_n|}{dn} = \lambda_\perp + \eta_n \tag{6.11}$$

where we replaced the iteration process with the derivative since we are interested in the long time behaviour of the mapping system. The fluctuations η_n should satisfy the requirements

$$\begin{aligned} \langle \eta_n \rangle &= 0 \\ \langle \eta_n \eta_{n'} \rangle &= 2D\delta_{nn'}, \end{aligned} \tag{6.12}$$

where D can be seen as the "intensity" of the fluctuations. The process (6.10) with the local TLE (6.12) represents a stochastic differential equation, as the

ones described in the previous Chapter. So the probability density function of the variable $|z|$ should be a solution of the Fokker-Planck equation (4.17). The properties of the fluctuations are the same already explained at the beginning of Section 4.2.1 for the stochastic (or Langevin) force $\Gamma(t)$. To be more explicit, consider the iterative equation (6.10). When $\lambda_\perp < 0$, $|z_n| \to 0$, and the trajectories of the two systems coupled as in (4.1) converges onto the synchronised state $\mathcal{S}$, as expected. If, on the contrary, $\lambda_\perp > 0$, even if small, $|z_n|$ is supposed to diverge to infinity, that nevertheless does not happen in a deterministic system like (4.1) ($|z_n|$ is upper bounded to 1 because of the boundness of the variables x and y), but also in (2.5) (where it is not). Thus there must be a type of reinjection process for the dynamics for $\lambda_\perp > 0$, and this can be modelled, starting from relation (6.11), as a power law in the distance, given by

$$\frac{d \log |z_n|}{dn} = \lambda_\perp + \eta_n - \beta |z_n|^p \tag{6.13}$$

firstly introduced by [Fujisaka & Yamada 86b] (where $p = 2$ was chosen), and later developed by [Fujisaka *et al.* 97a,b]. The model (6.13) has been termed *multiplicative noise model*, as explained in a more general form in [Schenzle & Brand 79]. The next question is whether we can find an evolution equation for the probability density function $P(n)$ in the case the Langevin dynamics is described by (6.13). The first thing we can see in (6.13) is that the diffusion coefficient is still D, while the drift coefficient is now given by $\lambda(|z|) = -\lambda_\perp + \beta |z_n|^p$.

A Fokker-Planck equation for the Langevin process (6.13) has been developed by [Fujisaka *et al.* 97b], and in the variable $|z|$ has the form

$$\frac{\partial P(|z|, n)}{\partial n} = -\frac{\partial}{\partial |z|}[(\lambda_\perp - \beta |z|^2 + D)|z| P(|z|, n)] + D \frac{\partial^2}{\partial |z|^2}[|z|^2 P(|z|, n)]$$

whose stationary solution can be calculated as [Fujisaka *et al.* 97b]

$$P(|z|) \propto |z|^{-(1+\eta)} \exp\left(-\frac{\beta |z|^2}{2D}\right) \tag{6.14}$$

where, as in Chapter 4, $\eta = \lambda_\perp / D$. In [Fujisaka *et al.* 97b] it has been show that the simulated dynamics of the Langevin process (6.13) yields a on-off intermittent time series, so to prove the correctness of the probability density function (6.14)

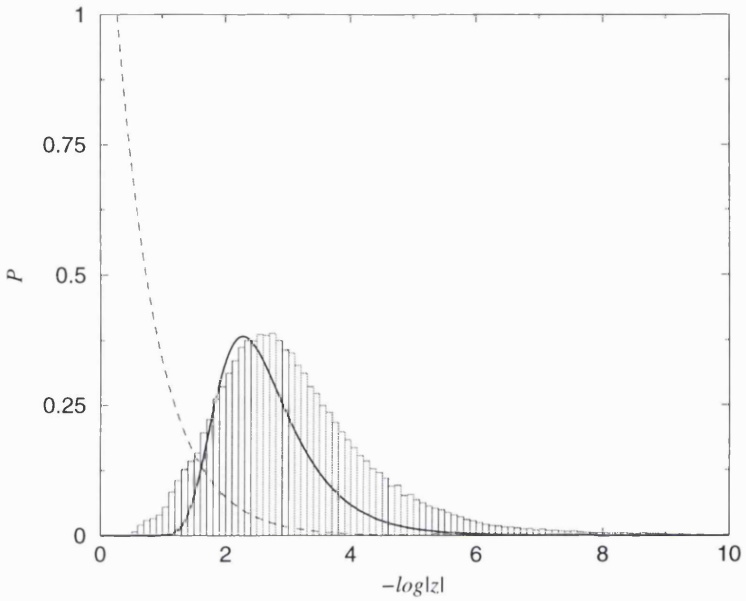

Figure 6.4: Histogram of the distribution of a time series of $-\log|z|$ of 10000 iterations compared with the probability density functions of the simple DDA (4.30) (thin dashed line) and the probability density function for the multiplicative noise model (thick solid line). We have used $\beta = 3$ to fit the peak of the distribution, and a normalisation *ad hoc*.

we plot, in Figure 6.4, a histogram of the distribution of a time series of $-\log|z|$ of 10000 iterations compared with the probability density functions of the simple DDA (4.30) (thin dashed line) and the probability density function for the multiplicative noise model, that in the new variable $\tilde{z} = -\log|z|$ reads

$$P(\tilde{z}) \propto \exp(-\eta\tilde{z}) \exp\left(-\frac{\beta e^{-2\tilde{z}}}{2D}\right), \tag{6.15}$$

and that is shown in the thick solid line. We have not found a normalisation coefficient for (6.14), so the solid curve (6.15) has been adapted to be visually compared with the histogram, but we found that the best choice of β for the correctness of the peak should be $\beta \simeq 3$, rather than the $\beta = 1$ used by Fujisaka and Yamada, provided that the exponent p in (6.13) is 2.

Bibliography

[Abarbanel 95] H.D.I. Abarbanel. *Analysis of observed chaotic data*, Springer (1995).

[Afraimovich *et al.* 86] V.S. Afraimovich, N.N. Verichev and M.I. Rabinovich. Stochastic synchronization of oscillations in dissipative systems, *Radiophys. Quantum Electron.* **29**,795-803(1986).

[Alexander *et al.* 92] J.C. Alexander, J.A. Yorke, Z. You and I. Kan. Riddled Basins, *Int. J. Bif. Chaos* **2**,795-813(1992).

[Arecchi & Boccaletti 97] F.T. Arecchi and S. Boccaletti. Adaptive strategies for recognition, noise filtering, control, synchronization and targeting of chaos, *CHAOS* **7**,621-634(1997).

[Ashwin *et al.* 94] P. Ashwin, J. Buescu and I. Stewart. Bubbling of attractors and synchronisation of chaotic oscillators, *Phys. Lett. A* **193**,126-139(1994).

[Ashwin *et al.* 96] P. Ashwin, J. Buescu and I. Stewart. From attractor to chaotic saddle: a tale of transverse instability, *Nonlinearity* **9**,703-737(1996).

[Ashwin *et al.* 98] P. Ashwin, P.J. Aston and M. Nicol. On the unfolding of the blowout bifurcation, *Physica D* **111**,81-95(1998).

[Ashwin & Rucklidge 98] P. Ashwin and A.M. Rucklidge. Cycling chaos: its creation, persistence and loss of stability in a model of nonlinear magnetoconvection, *Physica D* **122**,134-154(1998).

[Bagnoli *et al.* 99] F. Bagnoli, L. Baroni and P. Palmerini. Synchronization and directed percolation in coupled map lattices, *Phys. Rev. E* **59**,409-416(1999).

[Baker & Gollub 90] G.L. Baker and J.P. Gollub. *Chaotic dynamics: an introduction*, Cambridge Univ. Press (1990).

[Beck & Schlögl 93] C. Beck and F. Schlögl. *Thermodynamics of chaotic systems*, Cambridge Univ. Press (1993).

[Benettin *et al.* 80] G. Benettin, L. Galgani, A. Giorgilli and J.M. Strelcyn. Lyapunov characteristic exponents for smooth dynamical systems and for Hamiltonian systems: a method for computing all of them, *Meccanica* **15**,9-40(1980).

[Benzi *et al.* 85] R. Benzi, G. Paladin, G. Parisi and A. Vulpiani. Characterization of intermittency in chaotic systems, *J. Phys. A* **18**,2157-2165(1985).

[Bischi *et al.* 98] G.-I. Bischi, L. Stefanini and L. Gardini. Synchronization, intermittency and critical curves in a duopoly game, *Math. Comp. Simulation* **44**,559-585(1998).

[Buescu & Stewart 94] J. Buescu and I. Stewart. Lyapunov stability and adding machines, *Ergod. Theor. Dynam. Sys.* **15**,1-20(1994).

[Chandrasekhar 43] S. Chandrasekhar. Dynamical friction, *Astrophys. J.* **97**,263-273(1943).

[Chua 92] L.O. Chua. The genesis of Chua circuit, *Archiv für Electronik und Ubertragungstechnik* **46**,250-257(1992).

[Chua *et al.* 92] L.O. Chua, L. Kocarev, K. Eckert and M. Itoh, Chaos synchronization in Chua's circuit, *Int. J. Bif. Chaos* **2**,705-709(1992), also in [Madan 93], pag.309.

[Covas *et al.* 97] E. Covas, P. Ashwin and R. Tavakol. Non-normal parameter blowout bifurcation: an example in a truncated mean-field dynamo model, *Phys. Rev. E* **56**,6451-6458(1997).

[Cuomo & Oppenheim 93] K. Cuomo and A. Oppenheim. Circuit implementation of synchronized chaos with application to secure communication, *Phys. Rev. Lett.* **71**,65-68(1993).

[Cvitanović *et al.* 88] P. Cvitanović, G.H. Gunaratne and I. Procaccia. Topological and metric properties of of Hénon-type strange attractors, *Phys. Rev. A* **38**,1503-1520(1988).

[Duane 97] G.S. Duane. Synchronized chaos in extended systems and metereological teleconnections, *Phys. Rev. E* **56**,6475-6493(1997).

[Duffing 18] G. Duffing. *Erzwungene Schwingungen bei Veränderlicher Eigenfrequenz*, F. Vieweg u. Sohn, Braunschweig (1918).

[Eckmann & Ruelle 85] J.-P. Eckmann and D. Ruelle. Ergodic theory of chaos and strange attractors, *Rev. Mod. Phys.* **57**,617-656(1985).

[Einstein 05] A. Einstein. Über die von der molekularkinetischen Theorie der Wärme geforderte Bewegung von in ruhenden Flüssigkeiten suspendierten Teilchen, *Ann. Physik* **17**,549-560(1905).

[Feller 57] W. Feller. *An introduction to probability theory and its applications*, J.Wiley & Sons, New York (1957).

[Fujisaka & Yamada 83] H. Fujisaka and T. Yamada. Stability theory of synchronized motion in coupled-oscillator systems I, *Prog. Theor. Phys.* **69**,32-47(1983).

[Fujisaka & Yamada 85] H. Fujisaka and T. Yamada. A new intermittency in coupled dynamical systems, *Prog. Theor. Phys.* **74**,918-921(1985).

[Fujisaka & Yamada 86a] H. Fujisaka and T. Yamada. Stability theory of synchronized motion in coupled-oscillator systems IV, *Prog. Theor. Phys.* **75**,1087-1104(1986).

[Fujisaka & Yamada 86b] H. Fujisaka and T. Yamada. Intermittency caused by chaotic modulation I, *Prog. Theor. Phys.* **76**,582-591(1986).

[Fujisaka *et al.* 97a] H. Fujisaka, S. Matsushita and T. Yamada. Fluctuation-controlled transient below the on-off intermittency transition, *J. Phys. A* **30**,5697-5707(1997).

[Fujisaka *et al.* 97b] H. Fujisaka, S. Matsushita, T. Yamada and H. Tominaga. On-off intermittency and large deviation statisical mechanics, *Phys. Rep.* **290**,27-36(1997).

[Gauthier & Bienfang 96] D.J. Gauthier and C. Bienfang. Intermittent loss of synchronization in coupled chaotic oscillators - toward a new criterion for high-quality synchronization, *Phys. Rev. Lett.* **77**,1751-1754(1996).

[Geist *et al.* 90] K. Geist, U. Parlitz and W. Lauterborn. Comparison of different methods for computing Lyapunov exponents, *Prog. Theor. Phys.* **83**,875-893(1990).

[Gradshteyn & Ryzhik 94] I.S. Gradshteyn and I.M. Ryzhik. *Table of integrals, series, and products*, Academic Press (1994).

[Grebogi *et al.* 83a] C. Grebogi, S.W. McDonald, E. Ott and J.A. Yorke. Final state sensitivity: an obstruction to predictability, *Phys. Lett. A* **99**,415-418(1983).

[Grebogi *et al.* 83b] C. Grebogi, E. Ott and J.A. Yorke. Crises, sudden changes in chaotic attractors and chaotic transients, *Physica D* **7**,181-200(1983).

[Grebogi *et al.* 87a] C. Grebogi, E. Ott and J.A. Yorke. Basin boundaries metamorphoses: changes in accessible boundary orbits, *Physica D* **24**,243-262(1987).

[Grebogi *et al.* 87b] C. Grebogi, E. Ott, F. Romeiras and J.A. Yorke. Critical exponents for crisis-induced intermittency, *Phys. Rev. A* **36**,5365-5380(1987).

[Grimmett & Stirzaker 92] G.R. Grimmett and D.R. Stirzaker. *Probability and random processes*, Clarendon Press, Oxford (1992).

[Gwinn & Westervelt 85] E.G. Gwinn and R.M. Westervelt. Intermittent chaos and low-frequency noise in the driven damped pendulum, *Phys. Rev. Lett.* **54**,1613-1616(1985).

[Haken 75] H. Haken. Analogy between higher instabilities in fluids and lasers, *Phys. Lett. A* **53**,77-78(1975).

[Haken 83] H. Haken. *Advanced synergetics*, Springer-Verlag (1983).

[Hammer *et al.* 94] P.W. Hammer, N. Platt, S.M. Hammel and B.D. Lee. Experimental observation of on-off intermittency, *Phys. Rev. Lett.* **73**,1095-1098(1994).

[Hao 90] Bai-Lin Hao. *CHAOS II*, World Scientific, Singapore (1990).

[Hasler & Maistrenko 97] M. Hasler and Y.L. Maistrenko. An introduction to the synchronization of chaotic systems: coupled skew tent maps, *IEEE Trans. Circuits Syst.* **44**,856-866(1997).

[Hata & Miyazaki 97] H. Hata and S. Miyazaki. Exactly solvable maps of on-off intermittency, *Phys. Rev. E* **55**,5311-5314(1997).

[Hayli & Vidovic 94] A. Hayli and A. Vidovic. Sommerer and Ott system with qualitatively uncertain dynamics revisited, *Phys. Lett. A* **195**,59-62(1994).

[Heagy *et al.* 94a] J.F. Heagy, N. Platt and S.M. Hammel. Characterization of on-off intermittency, *Phys. Rev. E* **49**,1140-1150(1994).

[Heagy *et al.* 94b] J.F. Heagy, T.L. Carroll and L.M. Pecora. Synchronous chaos in coupled oscillator system, *Phys. Rev. E* **50**,1874-1885(1994).

[Heagy *et al.* 94c] J.F. Heagy, T.L. Carroll and L.M. Pecora. Experimental and numerical evidence for riddled basins in coupled chaotic systems, *Phys. Rev. Lett.* **73**,3528-3531(1994).

[Heagy *et al.* 95a] J.F. Heagy, T.L. Carroll and L.M. Pecora. Desynchronization by periodic orbits, *Phys. Rev. E* **52**,1253-1256(1995).

[Herzel & Freund 95] H. Herzel and J. Freund. Chaos, noise and synchronisation reconsidered, *Phys. Rev. E* **52**,3238-3241(1995).

[Hunt & Ott 96] B.R. Hunt and E. Ott. Optimal periodic orbits of chaotic systems, *Phys. Rev. Lett.* **76**,2254-2257(1996).

[Huygens 1673] C. Huygens. *Horoloqium Oscilatorium*, Parisis (1673)

[Jakobson 81] M.V. Jacobson. Absolutely continuous invariant measure for one parameter families of one dimensional maps, *Commun. Math. Phys.* **81**,39-88(1981).

[Johnson *et al.* 98] G.A. Johnson, D.J. Mar, T.L. Carroll and L.M. Pecora. Synchronization and imposed bifurcations in the presence of large parameter mismatch, *Phys. Rev. E* **57**,5247-5251(1998).

[Kaneko 93] K. Kaneko. *Theory and applications of coupled map lattices*, J. Wiley & Sons (1993).

[Kennedy 92] M.P. Kennedy. Robust op amp realization of Chua's circuit, *Frequenz* **46**,66-80(1992).

[Kocarev *et al.* 92] L. Kocarev, K.S. Halle, K. Eckert, U. Parlitz and L.O. Chua. Experimental demonstration of secure communications via chaotic synchronization, *Int. J. Bif. Chaos* **2**,709-713(1992).

[Koch & Meinhardt 94] A.J. Koch and H. Meinhardt. Biological pattern formation. From basic mechanisms to complex structures, *Rev. Mod. Phys.* **66**,1481-1507(1994).

[Konnur 96] R. Konnur. Equivalence of synchronization and control of chaotic systems, *Phys. Rev. Lett.* **77**,2937-2940(1996).

[Kuramoto 75] Y. Kuramoto. *Proceedings of the International Symposium on Mathematical Problems in Theoretical Physics*, edited by H. Araki, *Lecture Notes in Physics*, **39**, Springer-Verlag, Berlin (1975).

[Kuramoto 84] Y. Kuramoto. *Chemical oscillations, waves and turbulence* Springer-Verlag, Berlin (1984).

[Lai 96] Y.-C. Lai. Distinct small-distance scaling behaviour of on-off intermittency in chaotic dynamical systems, *Phys. Rev. E* **54**,321-327(1996).

[Lai & Grebogi 96a] Y.-C. Lai and C. Grebogi. Characterizing riddled fractal sets, *Phys. Rev. E* **53**,1371-1374(1996).

[Lai & Grebogi 96b] Y.-C. Lai and C. Grebogi. Noise-induced riddling in chaotic systems, *Phys. Rev. Lett.* **77**,5047-5050(1996).

[Lai *et al.* 96] Y.-C. Lai, C. Grebogi, J.A. Yorke and S.C. Venkataramani. Riddling bifurcation in chaotic dynamical systems, *Phys. Rev. Lett.* **77**,55-58(1996).

[Lindsey 72] W.C. Lindsey. *Synchronization systems in communication and control*, Prentice Hall, Englewood Cliffs, New Jersey (1972).

[Lorenz 63] E.N. Lorenz. Deterministic nonperiodic flow, *J. Atmos. Sci.* **20**,130-141(1963).

[Madan 93] *Chua's circuit: A Paradigm for Chaos*, edited by Rabinder N. Madan, (World Scientific Series on Nonlinear Sciences, Singapore, 1993).

[Maistrenko *et al.* 98a] Y.L. Maistrenko, V.L. Maistrenko, A. Popovich and E. Mosekilde. Role of the absorbing area in chaotic synchronization, *Phys. Rev. Lett.* **80**,1638-1641(1998).

[Maistrenko *et al.* 98b] Y.L. Maistrenko, V.L. Maistrenko, A. Popovich and E. Mosekilde. Transverse instability and riddled basins in a system of two coupled logostic maps, *Phys. Rev. E* **57**,2713-2724(1998).

[Maritan & Banavar 94a] A. Maritan and J.R. Banavar. Chaos, noise and synchronization, *Phys. Rev. Lett.* **72**,1451-1454(1994).

[Maritan & Banavar 94b] A. Maritan and J.R. Banavar. Reply on Comment on "Chaos, noise and synchronization" by A.S. Pikovsky, *Phys. Rev. Lett.* **73**,2932(1994).

[Matsumoto 84] T. Matsumoto. A chaotic attractor from the Chua's circuit, *IEEE Trans. Circuits Syst.* **31**,1055-1058(1984).

[Milnor 85] J. Milnor. On the concept of an attractor, *Comm. Math. Phys.* **99**,177-195(1985).

[Mira *et al.* 96] C. Mira, L. Gardini, A. Barngola and J.-C. Cathala. *Chaotic dynamics in two-dimensional noninvertible maps*, World Scientific, Singapore (1996).

[Moon & Holmes 79] F.C. Moon and P.J. Holmes. A magnetoelastic strange attractor, *J. Sound & Vib.* **65**,285-296(1979).

[Murali & Lakshmanan 93] K. Murali and M. Lakshmanan. Trasmission of signals by synchronization in a chaotic van der Pol-Duffing oscillator, *Phys. Rev. E* **48**,1624-1627(1993).

[Nagai & Lai 97] Y. Nagai and Y.-C. Lai. Periodic orbit theory of the blowout bifurcation, *Phys. Rev. E* **56**,4031-4041(1997).

[Oppenheim *et al.* 92] A. Oppenheim, G. Wornell, S. Isabelle and K. Cuomo. Signal processing in the context of chaotic signals, Proceedings *IEEE ICASSP*,117-120(1992).

[Ott 93] E. Ott. *Chaos in dynamical systems*, Cambridge Univ. Press (1993).

[Ott *et al.* 90] E. Ott, C. Grebogi and J.A. Yorke. Controlling chaos, *Phys. Rev. Lett.* **64**,1196-1199(1990).

[Ott *et al.* 94] E. Ott, J.C. Alexander, I. Kan, J.C. Sommerer and J.A. Yorke. The transition to chaotic attractors with riddled basins, *Physica D* **76**,384-410(1994).

[Ott & Sommerer 94] E. Ott and J.C. Sommerer. Blowout bifurcations: the occurrence of riddled basins and on-off intermittency, *Phys. Lett. A* **188**,39-47(1994).

[Pecora & Carroll 90] L.M. Pecora and T.L. Carroll. Synchronization in chaotic systems, *Phys. Rev. Lett.* **64**,821-824(1990).

[Pecora & Carroll 91] L.M. Pecora and T.L. Carroll. Driving systems with chaotic signals, *Phys. Rev. A* **44**,2374-2383(1991).

[Pecora *et al.* 97] L.M. Pecora, T.L. Carroll, G.A. Johnson, D.J. Mar and J.F. Heagy. Fundamentals of synchronization in chaotic systems, concepts and applications, *CHAOS* **7**,520-543(1997).

[Pegna *et al.* 99] G. Pegna, R. Marrocu, F. Meloni and G. Santoboni. Experimental definition of the basin of attraction for Chua's circuit, to be published in *Int. J. Bif. Chaos* (1999).

[Pérez & Cerdeira 95] G. Pérez and H.A. Cerdeira. Extracting messages masked by chaos, *Phys. Rev. Lett.* **74**,1970-1973(1995).

[Pikovski 84] A.S. Pikovsky. On the interaction of strange attractors, *Z. Phys. B* **55**,149-154(1984).

[Pikovski 94] A.S. Pikovski. Comment on "Chaos, noise and synchronization", *Phys. Rev. Lett.* **73**,2931(1994).

[Platt *et al.* 93] N. Platt, E.A. Spiegel and C. Tresser. On-off intermittency - a mechanism for bursting, *Phys. Rev. Lett.* **70**,279-282(1993).

[van der Pol & van der Mark 27] B. van der Pol and J. van der Mark. Frequency demultiplication, *Nature* **120**,363-364(1927).

[Pomeau & Manneville 80] Y. Pomeau and P. Manneville. Intermittent transition to turbulence in dissipative dynamical systems, *Commun. Math. Phys.* **74**,189-197(1980).

[Press *et al.* 92] W.H. Press, S.A. Teukolsky, W.T. Vetterling and B.P. Flannery. *Numerical Recipes*, Cambridge Univ. Press (1992).

[Ricciardi 77] L.M. Ricciardi. *Diffusion processes and related topics in biology*, Lecture Notes on Biomathematics, **14**, Springer-Verlag, Berlin (1977).

[Risken 84] H. Risken. *The Fokker-Planck equation*, Springer-Verlag (1984).

[Rosenblum *et al.* 96] M.G. Rosenblum, A.S. Pikovsky and J. Kurths. Phase synchronization of chaotic oscillators, *Phys. Rev. Lett.* **76**,1804-1807(1996).

[Rosenblum *et al.* 97] M.G. Rosenblum, A.S. Pikovsky and J. Kurths. From phase to lag synchronization in coupled chaotic oscillators, *Phys. Rev. Lett.* **78**,4193-4196(1997).

[Rössler 76] O.E. Rössler. An equation for continuous chaos, *Phys. Lett. A* **57**,397-398(1976).

[Roy & Thornburg 94] R. Roy and K.S. Thornburg. Experimental synchronization of chaotic lasers, *Phys. Rev. Lett.* **72**,2009-2012(1994).

[Rulkov *et al.* 95] N.F. Rulkov, M.M. Sushchik, L.S. Tsimring and H.D.I. Abarbanel. Generalized synchronization of chaos in directionally coupled chaotic systems, *Phys. Rev. E* **51**,980-994(1995).

[Sakaguchi & Kuramoto 86] H. Sakaguchi and Y. Kuramoto. A soluble active rotator model showing phase transitions via mutual entrainment, *Prog. Theor. Phys.* **76**,576-581(1986).

[Santoboni 96] G. Santoboni. *Sincronizzazione di sistemi caotici accoppiati*, B.Sc. Thesis, Univ. of Cagliari, Italy (1996).

[Santoboni *et al.* 98] G. Santoboni, S.R. Bishop and F. Meloni. Qualitatively unpredictable behaviour in the synchronised solutions of coupled nonlinear systems, *Conference Proceedings* **61** SIF, Bologna (1998).

[Santoboni *et al.* 99a] G. Santoboni, A. Varone and S.R. Bishop. Transient time in unidirectional synchronization, to be published in *Int. J. Bif. Chaos* **9**(1999).

[Santoboni *et al.* 99b] G. Santoboni, A. Varone and S.R. Bishop. Spatial distribution of chaotic transients in unidirectional synchronisation, *Phys. Lett. A* **257**,175-181(1999).

[Santoboni *et al.* 99c] G. Santoboni, R. Murray and S.R. Bishop. On the "premature" synchronisation of coupled maps, submitted to *Phys. Rev. E* (1999).

[Schäfer *et al.* 99] C. Schäfer, M.G. Rosenblum, H.-H. Abel and J. Kurths. Synchronization in the human cardiorespiratory system, *Phys. Rev. E* **60**,857-870(1999).

[Schenzle & Brand 79] A. Schenzle and H.Brand. Multiplicative stochastic process in statistical physics, *Phys. Rev. A* **20**,1628-1647(1979).

[Schuster *et al.* 86] H.G. Schuster, S. Martin and W. Martienssen. New method for determining the largest Lyapunov exponent of simple nonlinear systems, *Phys. Rev. A* **33**,3547-3550(1986).

[Shimada & Nagashima 79] I. Shimada and T. Nagashima. A numerical approach to ergodic problems of dissipative dynamical systems, *Prog. Theor. Phys.* **61**,1605-1616(1979).

[Shuai *et al.* 97] J.W. Shuai, K.W. Wong and L.M. Cheng. Synchronization of spatiotemporal chaos with positive conditional Lyapunov exponent, *Phys. Rev. E* **56**,2272-2275(1997).

[Siegert 51] A.J.F. Siegert. On the first passage time probability problem, *Physical Review* **81**,617-623(1951).

[Strogatz & Stewart 93] S.H. Strogatz and I. Stewart. Coupled oscillators and biological synchronization, *Sci. Am.* **269**,102-109(1993).

[Thompson & Stewart 86] J.M.T. Thompson & H.B. Stewart. *Nonlinear dynamics and chaos*, Wiley and Sons (1986).

[Thompson 89] J.M.T. Thompson. Chaotic phenomena triggering the escape from a potential well, *Proc. R. Soc. Lond. A* **421**,195-225(1989).

[Thompson & Chua 95] *Chaotic behaviour in electronic circuits*, Theme issue of the *Phil. Trans. Roy. Soc.*, edited by J.M.T. Thompson and L.O. Chua, **353** (October 1995).

[Turing 52] A.M. Turing. The chemical basis of morphogenesis, *Trans. R. Soc. London B* **237**,37-72(1952).

[Ueda & Akamatsu 80] Y. Ueda and N. Akamatsu. Chaotically transitional phenomena in the forced negative-resistance oscillators, *IEEE Trans. Circuits Syst.* **28**,217-224(1980).

[Venkataramani *et al.* 96] S.C. Venkataramani, B.R. Hunt, E. Ott, D.J. Gauthier and J.C. Bienfang. Transition to bubbling of chaotic systems, *Phys. Rev. Lett.* **77**,5361-5364(1996).

[van Wiggeren & Roy 98] G.D. van Wiggeren and R. Roy. Communication with chaotic lasers, *Science* **279**,1198-1200(1998).

[Winfree 80] A.T. Winfree. *The geometry of biological time*, Springer, New York (1980).

[Wolf *et al.* 85] A. Wolf, J.B. Swift, H.L. Swinney and J.A. Vastano. Determining Lyapunov exponents from a time series, *Physica D* **16**,285-317(1985).

[Yamada & Fujisaka 83] T. Yamada and H. Fujisaka. Stability theory of synchronized motion in coupled-oscillator systems II, *Prog. Theor. Phys.* **70**,1240-1248(1983).

[Yamada & Fujisaka 84] T. Yamada and H. Fujisaka. Stability theory of synchronized motion in coupled-oscillator systems III, *Prog. Theor. Phys.* **72**,885-894(1984).

[Yang & Chua 97] T. Yang and L.O. Chua. Impulsive control and synchronization of nonlinear dynamical systems and application to secure communication, *Int. J. Bif. Chaos* **7**,645-663(1997).

[Yang *et al.* 98] T. Yang, L.-B. Yang, and C.-M. Yang. Breaking chaotic secure communication using a spectrogram, *Phys. Lett. A* **247**,105-111(1998).

[Yeomans 92] J.M. Yeomans. *Statistical mechanics of phase transitions*, Clarendon Press, Oxford (1992).

[Zhou & Lai 98] C. Zhou and C.-H. Lai. Synchronization with positive Lyapunov exponents, *Phys. Rev. E* **58**,5188-5191(1998).

[Zonghua and Shigang 97] L. Zonghua and C. Shigang. Synchronization of a conservative map, *Phys. Rev. E* **56**,1585-1589(1997).